

UCSF

UC San Francisco Electronic Theses and Dissertations

Title

Optical Assessment of Caries Lesion Structure and Activity

Permalink

<https://escholarship.org/uc/item/34868360>

Author

Lee, Robert C.

Publication Date

2016

Peer reviewed|Thesis/dissertation

Optical Assessment of Caries Lesion Structure and Activity

by

Robert Chulsung Lee, DDS

DISSERTATION

Submitted in partial satisfaction of the requirements for the degree of

DOCTOR OF PHILOSOPHY

in

Oral and Craniofacial Sciences

in the

GRADUATE DIVISION

of the

UNIVERSITY OF CALIFORNIA, SAN FRANCISCO

Copyright 2016

by

Robert Chulsung Lee

DEDICATION

To my family and my fiancé

ACKNOWLEDGEMENTS

This work was supported by NIH/NIDCR grants F30-DE023278, R01-DE17869, R01-DE14698 and T32-DE07306.

Foremost, I would like to express my sincere gratitude to my dissertation advisor, Dr. Daniel Fried, for the continuous support, patience, motivation, enthusiasm, knowledge and guidance during the last eight years.

Besides my dissertation advisor, I would like to thank members of my dissertation and qualifying exam committee: Drs. Cynthia Darling, Michal Staninec, Tracy McKnight and Art Miller. I am very grateful for their brilliant comments.

My sincere thanks go to the current and past members of Dr. Fried's lab who contributed to my academic and scientific achievements: Dr. Cynthia Darling, Dr. Michal Staninec, Dr. Andrew Jang, Dr. Saman Manesh, Dr. Dennis Hsu, Kenneth Chan, Hobin Kang, Jacob Simon, Daniel Saltiel, Henry Tom and numerous summer dental students and residents. I would like to also acknowledge contributions from Dr. Oanh Le and Dr. Antonio Ragadio, Charles Le, Grace Nonomura and the late Larry Watanabe. Much of my experimental work could not have been completed without their help.

I am grateful to my graduate program advisor, Dr. Stefan Habelitz, my clinical coach and advisor, Dr. Peggy Leong, my clinical advisor, Dr. Ram Vaderhobli, and the program directors of the Oral and Craniofacial Sciences (OCS) group, Drs. Pam DenBesten and Ralph Marcucio for their valuable guidance throughout my clinical and research training. I am also thankful to Roger Mraz and Kathryn Gabriel for their guidance and administrative support through the program.

Finally, I would like to acknowledge the following scientific journals and their publishers for their permission to use following publications within this dissertation.

Chapter II

Used with permission from Society of Photo-optical Instrumentation Engineers:
Lee, R. C., Darling, C. L. and Fried, D. (2014). Automated detection of remineralization in simulated enamel lesions with PS-OCT. *SPIE Lasers in Dentistry XX*, San Jose, CA, **8929**: E1-8.

Chapter III

Used with permission from Optical Society of America:
Lee, R. C., Kang, H., Darling, C. L. and Fried, D. (2014). Automated assessment of the remineralization of artificial enamel lesions with polarization-sensitive optical coherence tomography. *Biomed. Opt. Express*, **5**(9): 2950-2962.

Chapter IV

Used with permission from Elsevier:
Lee, R. C., Darling, C. L. and Fried, D. (2015). Assessment of remineralization via measurement of dehydration rates with thermal and near-IR reflectance imaging. *J. Dent.*, **43**(8): 1032-1042.

Chapter V

Used with permission from IEEE:
Lee, R. C., Staninec, M., Le, O., and Fried, D. (2016). Infrared Methods for Assessment of the Activity of Natural Enamel Caries Lesions. *IEEE J. Sel. Top. Quantum Electron.*, **22**(3): 6803609.

Chapter VI

Used with permission from Wiley-VCH:
Lee, R. C., Darling, C. L., Staninec, M., Ragadio A., Fried, D. (2016) Activity assessment of root caries lesions with thermal and near-IR imaging methods. *J. Biophotonics*, (In Press).

Optical Assessment of Caries Lesion Structure and Activity

Robert Chulsung Lee, DDS

ABSTRACT

New, more sophisticated diagnostic tools are needed for the detection and characterization of caries lesions in the early stages of development. It is not sufficient to simply detect caries lesions, methods are needed to assess the activity of the lesion and determine if chemical or surgical intervention is needed. Previous studies have demonstrated that polarization sensitive optical coherence tomography (PS-OCT) can be used to nondestructively image the subsurface lesion structure and measure the thickness of the highly mineralized surface zone. Other studies have demonstrated that the rate of dehydration can be correlated with the lesion activity and that the rate can be measured using optical methods. The main objective of this work was to test the hypothesis that optical methods can be used to assess lesion activity on tooth coronal and root surfaces.

Simulated caries models were used to develop and validate an algorithm for detecting and measuring the highly mineralized surface layer using PS-OCT. This work confirmed that the algorithm was capable of estimating the thickness of the highly mineralized surface layer with high accuracy. Near-infrared (NIR) reflectance and thermal imaging methods were used to assess activity of caries lesions by measuring the state of lesion hydration. NIR reflectance imaging performed the best for artificial enamel and natural coronal caries lesion samples, particularly at wavelengths coincident with the water absorption band at 1460-nm. However, thermal imaging performed the best for artificial dentin and natural root caries lesion samples. These

novel optical methods outperformed the conventional methods (ICDAS II) in accurately assessing lesion activity of natural coronal and root caries lesions.

Infrared-based imaging methods have shown potential for *in-vivo* applications to objectively assess caries lesion activity in a single examination. It is likely that if future clinical trials are a success, this novel imaging technology will be employed for the detection and monitoring of early carious lesions without the use of ionizing radiation, thereby enabling conservative non-surgical intervention and the preservation of healthy tissue structure.

TABLE OF CONTENTS

TITLE PAGE	i
DEDICATION	iii
ACKNOWLEDGEMENTS	iv
ABSTRACT	vi
TABLE OF CONTENTS	viii
LIST OF TABLES	xii
LIST OF FIGURES	xiii
CHAPTER I. INTRODUCTION	1
1.1. Dissertation Motivation and Clinical Significance	2
1.2. Caries Process and Lesion Arrestment	2
1.3. Conventional Methods for Caries Lesion Activity Assessment	4
1.3.1. Coronal Primary Caries Lesion Activity Assessment	5
1.3.2. Root Caries Lesion Activity Assessment	6
1.4. Optical Methods for Caries Lesion Activity Assessment	8
1.4.1. Quantitative Light-induced Fluorescence	8
1.4.2. Pulse Thermography	9
1.5. Infrared Methods for Caries Lesion Activity Assessment	10
1.5.1. Polarization-Sensitive Optical Coherence Tomography	12
1.5.2. Near-infrared Reflectance Imaging with Dehydration	16
1.5.3. Thermal Imaging with Dehydration	17
1.6. Overall hypothesis and objectives	18
1.7. Figures and Figure Legends	20
1.8. References	25
CHAPTER II. AN ALGORITHM FOR DETECTION AND MEASUREMENT OF HIGHLY MINERALIZED SURFACE LAYER WITH POLARIZATION-SENSITIVE OPTICAL COHERENCE TOMOGRAPHY	32
2.1. Summary	33
2.2. Introduction	33
2.3. Materials and Methods	36
2.3.1. Sample Preparation and Simulated Lesion Models	36
2.3.2. PS-OCT System	37
2.3.3. Polarized Light Microscopy	38
2.3.4. Phase Adjustment	39
2.3.5. Image Processing	39

2.3.6. Edge Detection, Artifact Removal and Integrated Reflectivity	39
2.3.7. Transparent Surface Layer Detection and Measurement.....	40
2.3.8. Statistical Analysis	41
2.4. Results and Discussion	41
2.5. Conclusion	43
2.6. Figures and Figure Legends.....	44
2.7. References	49

CHAPTER III. AUTOMATED ASSESSMENT OF REMINERALIZATION OF ARTIFICIAL ENAMEL LESIONS WITH POLARIZATION-SENSITIVE OPTICAL COHERENCE TOMOGRAPHY 51

3.1. Summary	52
3.2. Introduction	53
3.3. Materials and Methods	57
3.3.1. Sample Preparation	57
3.3.2. PS-OCT System	58
3.3.3. Image Processing.....	60
3.3.4. Transparent Surface Layer Detection and Measurement.....	61
3.3.5. Lesion Depth Measurement.....	62
3.3.6. Integrated Reflectivity Measurement	63
3.3.7. Polarized Light Microscopy and Transverse Microradiography	63
3.3.8. Statistical Analysis	64
3.4. Results	65
3.5. Discussion	68
3.6. Conclusion	70
3.7. Figures and Figure Legends.....	71
3.8. References	78

CHAPTER IV. ASSESSMENT OF REMINERALIZATION VIA MEASUREMENT OF DEHYDRATION RATES WITH THERMAL AND NEAR-INFRARED REFLECTANCE IMAGING..... 81

4.1. Summary	82
4.2. Introduction	83
4.3. Materials and Methods	86
4.3.1. Sample Preparation	86
4.3.2. PS-OCT System	87
4.3.3. Calculation of Transparent Surface Layer Thickness, Lesion Depth and Integrated Reflectivity	88
4.3.4. Dehydration Measurements.....	90
4.3.5. Thermal Imaging and Analysis	90
4.3.6. NIR Reflectance Imaging and Analysis	91
4.3.7. Polarized Light Microscopy and Transverse Microradiography	93
4.3.8. Statistical Analysis	94
4.4. Results	95

4.5. Discussion	98
4.6. Conclusion	100
4.7. Figures and Figure Legends	101
4.8. References	114

CHAPTER V. INFRARED METHODS FOR ASSESSMENT OF THE ACTIVITY OF NATURAL ENAMEL CARIES LESIONS 118

5.1. Summary	119
5.2. Introduction	119
5.3. Materials and Methods	124
5.3.1. Sample Selection and Examination	124
5.3.2. PS-OCT System	125
5.3.3. Calculation of Transparent Surface Layer Thickness, Lesion Depth and Integrated Reflectivity	126
5.3.4. Dehydration Measurements.....	127
5.3.5. Thermal Imaging and Analysis	128
5.3.6. NIR Reflectance Imaging and Analysis	129
5.3.7. Polarized Light Microscopy, Transverse Microradiography and Histological Validation of Lesion Activity	130
5.3.8. Statistical Analysis	131
5.4. Results	131
5.4.1. ICDAS II Lesion Activity Assessment	131
5.4.2. Infrared Imaging Methods for Lesion Activity Assessment	132
5.5. Discussion	135
5.6. Conclusion	139
5.7. Figures and Figure Legends	140
5.8. References	151

CHAPTER VI. ACTIVITY ASSESSMENT OF ROOT CARIES LESIONS WITH THERMAL AND NEAR-INFRARED IMAGING METHODS 155

6.1. Summary	156
6.2. Introduction	156
6.3. Materials and Methods	160
6.3.1. Simulated Dentin Lesion Sample Preparation	160
6.3.2. Natural Root Caries Lesion Sample Selection and Examination.....	162
6.3.3. PS-OCT System	162
6.3.4. Calculation of Transparent Surface Layer Thickness, Lesion Depth and Integrated Reflectivity	163
6.3.5. Dehydration Measurements.....	166
6.3.6. Thermal Imaging and Analysis	167
6.3.7. NIR Reflectance Imaging and Analysis	168
6.3.8. Polarized Light Microscopy and Transverse.....	169
6.3.9. Histological Validation of Lesion Activity of Natural Root Caries Lesions.	170
6.3.10. Statistical Analysis	170

6.4. Results	171
6.4.1. Simulated Dentin Lesions	171
6.4.2. Natural Root Caries Lesions	173
6.5. Discussion	174
6.6. Conclusion	179
6.7. Figures and Figure Legends	180
6.8. References	189

CHAPTER VII. SUMMARY AND FUTURE PERSPECTIVE 192

7.1. Summary	193
7.1.1. Coronal Caries Lesion Activity Assessment	193
7.1.2. Root Caries Lesion Activity Assessment	195
7.2. Future Perspective	196
7.3. References	198

LIST OF TABLES

CHAPTER I. INTRODUCTION

Table 1.1.....	20
Table 1.2.....	21

CHAPTER III. AUTOMATED ASSESSMENT OF REMINERALIZATION OF ARTIFICIAL ENAMEL LESIONS WITH POLARIZATION-SENSITIVE OPTICAL COHERENCE TOMOGRAPHY

Table 3.1.....	71
----------------	----

CHAPTER IV. ASSESSMENT OF REMINERALIZATION VIA MEASUREMENT OF DEHYDRATION RATES WITH THERMAL AND NEAR-INFRARED REFLECTANCE IMAGING

Table 4.1.....	101
Table 4.2.....	102
Table 4.1.....	103

CHAPTER V. INFRARED METHODS FOR ASSESSMENT OF THE ACTIVITY OF NATURAL ENAMEL CARIES LESIONS

Table 5.1.....	140
Table 5.2.....	141

CHAPTER VI. ACTIVITY ASSESSMENT OF ROOT CARIES LESIONS WITH THERMAL AND NEAR-INFRARED IMAGING METHODS

Table 6.1.....	180
Table 6.2.....	181

LIST OF FIGURES

CHAPTER I. INTRODUCTION

Figure 1.1	22
Figure 1.2	23
Figure 1.3	24

CHAPTER II. AN ALGORITHM FOR DETECTION AND MEASUREMENT OF HIGHLY MINERALIZED SURFACE LAYER WITH POLARIZATION-SENSITIVE OPTICAL COHERENCE TOMOGRAPHY

Figure 2.1	44
Figure 2.2	45
Figure 2.3	47
Figure 2.4	48

CHAPTER III. AUTOMATED ASSESSMENT OF REMINERALIZATION OF ARTIFICIAL ENAMEL LESIONS WITH POLARIZATION-SENSITIVE OPTICAL COHERENCE TOMOGRAPHY

Figure 3.1	72
Figure 3.2	73
Figure 3.3	74
Figure 3.4	75
Figure 3.5	76
Figure 3.6	77

CHAPTER IV. ASSESSMENT OF REMINERALIZATION VIA MEASUREMENT OF DEHYDRATION RATES WITH THERMAL AND NEAR-INFRARED REFLECTANCE IMAGING

Figure 4.1	104
Figure 4.2	105
Figure 4.3	106
Figure 4.4	107
Figure 4.5	108
Figure 4.6	109
Figure 4.7	110
Figure 4.8	111
Figure 4.9	112
Figure 4.10	113

CHAPTER V. INFRARED METHODS FOR ASSESSMENT OF THE ACTIVITY OF NATURAL ENAMEL CARIES LESIONS

Figure 5.1 142
Figure 5.2 144
Figure 5.3 146
Figure 5.4 148
Figure 5.5 150

CHAPTER VI. ACTIVITY ASSESSMENT OF ROOT CARIES LESIONS WITH THERMAL AND NEAR-INFRARED IMAGING METHODS

Figure 6.1 182
Figure 6.2 183
Figure 6.3 184
Figure 6.4 185
Figure 6.5 186
Figure 6.6 188

CHAPTER I

INTRODUCTION

1.1 Dissertation Motivation and Clinical Significance

During the past century, the nature of dental decay or dental caries in the US has changed markedly due to the introduction of fluoride to the drinking water, the use of fluoride dentifrices and rinses, application of topical fluoride in the dental office and improved dental hygiene. In spite of these advances, dental decay continues to be the leading cause of tooth loss in the US (Chauncey et al. 1989, Kaste et al. 1996, Winn et al. 1996). The nature of the caries problem has changed dramatically with the majority of newly discovered caries lesions being highly localized to the occlusal pits and fissures of the posterior dentition and the proximal contact sites between teeth where they are more difficult to detect. In addition, the prevalence of dental fluorosis appears to be increasing in the US and areas of hypomineralization on tooth surfaces further complicates diagnosis (Denbesten and Li 2011). New diagnostic tools are needed for the detection and characterization of caries lesions in the early stages of development (Featherstone 1996, Hume 1996, ten Cate and van Amerongen 1996, NIH 2001). The caries process is potentially preventable and curable. If carious lesions are detected early enough, it is likely that they can be arrested or reversed by non-surgical means through fluoride therapy, anti-bacterial therapy, dietary changes, or by low intensity laser irradiation (Featherstone 1999, NIH 2001). Therefore, one cannot overstate the importance of detecting the decay at its early stage of development at which point non-invasive preventive measures can be taken to halt further decay.

1.2 Caries Process and Lesion Arrestment

It is well established that demineralization and remineralization occur in the mouth and

the topical use of fluoride inhibits demineralization and enhances remineralization (ten Cate and Duijsters 1982, ten Cate and Featherstone 1991). Sound enamel and dentin crystals are mainly composed of a hydroxyapatite-like mineral that contains many defects and impurities such as carbonated hydroxyapatite that are much more soluble than pure hydroxyapatite or fluorapatite (Featherstone 2008). Demineralization of dental tissue occurs as a result of plaque accumulation and elimination of oral mechanical disturbance promoting progressive lesion formation (Thylstrup et al. 1994). Cariogenic bacteria metabolize fermentable carbohydrates and produce organic acid dissolving calcium and phosphate from the intact crystals (Featherstone 2008). If fluoride ions are present in sufficient concentration during demineralization, these ions can be absorbed into the crystal and further demineralization can be inhibited (Featherstone et al. 1990). Remineralization can reverse the caries process by repairing existing crystal remnants with the help of calcium and phosphate ions, primarily from saliva, and fluoride ions from topical sources (Featherstone 2000). In order to facilitate caries lesion arrestment via remineralization, oral mechanical force must be present to remove cariogenic biomass from the tooth surface (Thylstrup et al. 1994). Saliva also aids in remineralization by inducing gradual pH recovery, promoting re-precipitation of minerals; proline-rich phosphoproteins are present in saliva to hold calcium and phosphate ions at supersaturated concentrations while preventing spontaneous precipitation (Lamkin and Oppenheim 1993). Fluoride also helps the remineralization process by forming a fluorapatite-rich surface layer, which is much more acid resistant than pure phase hydroxyapatite (ten Cate and Featherstone 1991).

The protective factors such as good oral hygiene, adequate salivary flow and

exposure to topical fluoride must outweigh the pathological factors such as high fermentable carbohydrate diet, poor oral hygiene and sub-normal salivary flow and function in order for the remineralization therapy to succeed and reverse the caries process (Featherstone 2008). If the pathological factors outweigh the protective factors, further demineralization will eventually lead to cavitation of the tooth surface. Therefore, during the early caries process, prior to cavitation, therapeutic intervention can arrest or reverse the demineralization through remineralization. With an adequate enough fluorapatite-rich surface layer, diffusion of calcium and phosphate ions at the lesion body may be dramatically reduced (ten Cate and Arends 1977, Kidd 1983, ten Cate and Featherstone 1991). This leads to the arrest of lesion progression and no further intervention is necessary.

1.3 Conventional Methods for Caries Lesion Activity Assessment

Current methods for lesion assessment are composed of a combination of visual and tactile exams, which are prone to subjective bias and interference from staining, are limited to exposed surfaces and there is the potential for permanent damage to the intact lesion surface layer from sharp instruments (NIH 2001, Ekstrand et al. 2009). Clinical disagreement in caries lesion activity diagnosis can be attributed to several factors including variations in examiners' visual acuity, differences in tactile sensitivity, inferences by clinicians, direct and indirect lighting, the use of magnifying eyewear, patient position, instrument used for assessment and interactions between the clinician and the patient (Banting 1993). In addition, the remineralized caries lesion still retains the white coloration due to subsurface demineralization, which may lead to an

inconclusive diagnosis of caries lesion activity (Ekstrand et al. 2009). The histological analyses for lesion assessment such as transverse microradiography (TMR) and polarized light microscopy (PLM) require destruction of the tooth, making both methods unsuitable for use *in-vivo*. Ekstrand et al. reported that it is extremely difficult to differentiate active lesions from inactive lesions in a single clinical examination without training or calibration (Ekstrand et al. 2005). Clinical criteria for caries lesion activity has been introduced by Nyvad et al. and incorporated by the international Caries Detection and Assessment System (ICDAS) II caries classification system, but both of these methods also utilize visual-tactile examination (Nyvad et al. 1999, Banting et al. 2005).

1.3.1 Coronal Primary Caries Lesion Activity Assessment

Early caries lesions can be described as non-cavitated subsurface lesions with an intact surface layer (Fejerskov and Kidd 2003). The lesion body manifests increased porosity due to mineral loss while the surface layer is maintained due to mineral deposition from saliva. The difference between refractive index (RI) of enamel crystals (RI 1.6) and watery saliva medium inside the porosities (water RI 1.33) causes light scattering that results in a white opaque appearance, and this effect is much more pronounced when the lesion is dried (air RI 1.00) (Gugnani et al. 2012). At advanced stages of caries, the surface of the lesion becomes further demineralized giving it a chalky white surface appearance due to irregular surface erosion and cavitation (Thylstrup et al. 1994, Nyvad et al. 1999). Arrested caries lesions exhibit a glossy appearance with a surface hardness that is comparable to sound enamel because they have a highly mineralized

surface layer on the outer surface of the lesion (Thylstrup et al. 1994, Nyvad et al. 1999, Ekstrand et al. 2005).

The ICDAS II criteria for enamel caries lesion activity assessment are largely based on the Nyvad criteria, which were validated based on a three-year longitudinal study involving modification to oral hygiene routine and use of fluoride dentrifice (Nyvad et al. 2003). These criteria utilize the physical properties of surface reflection, texture of early lesion, with chalky rough surfaces being active, and smooth, shiny surfaces being inactive (Banting et al. 2005). Enamel caries lesions also manifest in different colors, which can also be used to differentiate between arrested and active lesions; arrested lesions may exhibit internal brown pigmentation and surface stain, and active lesions retain white appearance (Banting et al. 2005). However, there are major differences between the Nyvad criteria and ICDAS II criteria: 1) the ICDAS II criteria score the lesion activity independently from the lesion severity; 2) Teeth are cleaned with prophy paste and dried for 5 seconds prior to the ICDAS II examination; 3) A ball-ended probe is recommended in the ICDAS II examination to avoid unnecessary damage to the dental hard tissues. **Table 1.1** shows the ICDAS II criteria for coronal caries lesion activity assessment.

1.3.2 Root Caries Lesion Activity Assessment

There is a general trend of increasing incidence of caries in the elderly, mostly related to gingival recession and root caries (Kassebaum et al. 2015). It is extremely difficult to detect early root caries due to its rapid progression and lack of reliable diagnostic techniques (Fejerskov and Kidd 2003). Root caries generally occur anywhere on the

root surface coronal to the gingival margin (Banting 1993). The ICDAS coordinating committee and Ekstrand et al. proposed clinical scoring systems for assessing root caries lesion activity (Banting et al. 2005, Ekstrand et al. 2008). However, the clinical methods for root caries lesion activity assessment are based solely on clinical signs in the absence of histological validation (Lynch and Beighton 1994). Accurate diagnosis of early root caries and non-carious cervical lesions (NCCL) is necessary to apply appropriate treatments for occlusion of dentinal tubules and restoration of the lost tooth structure.

The ICDAS II criteria for root caries lesion activity assessment utilize the clinical signs of lesion location, contour, color, cavitation and surface texture. Beighton et al. reported that most root caries lesions occur within 2 mm of the gingival crest due to frequent plaque accumulation (Beighton et al. 1993). Although color has been shown not to be reliable by itself in determining root caries lesion activity, active lesions likely exhibit yellowish or light brown in color while arrested lesions retain dark stain (Hellyer et al. 1990). ICDAS notes that non-cavitated root caries lesions are almost universally considered to be active while cavitated root caries lesions may be either active or arrested (Banting et al. 2005). Active root caries lesions exhibit a soft or leathery texture compared to arrested lesions that have a hard texture (Lynch and Beighton 1994). **Table 1.2** shows the ICDAS II criteria for root caries lesion activity assessment.

1.4 Optical Methods for Caries Lesion Activity Assessment

There have been steady developments of clinically useful instruments to assist clinicians in assessing caries lesion activity in real-time: Quantitative Light-induced Fluorescence (QLF) and pulse thermography.

1.4.1 QLF

QLF is a non-destructive caries detection method based on a yellow/green fluorescent light (Spitzer and Bosch 1976, Alfano and Yao 1981, Bjelkhagen et al. 1982). Although the chromophores causing the tooth fluorescence have not been clearly identified, aromatic amino acids in dentinal collagen seems to be the contributory factor upon illumination with UV or blue light (Spitzer and Bosch 1976). QLF may involve several different mechanisms: 1) the light scattering in the lesion is much stronger than in sound enamel, effectively reducing the light path in the lesion and the light absorption per volume, thus the fluorescence is reduced; 2) the light scattering in the lesion reduces the visibility of the underlying fluorescing light; 3) chromophores in the lesion are quenched and do not fluoresce as well as sound dental tissue; 4) the effective number of chromophores in the lesions are reduced due to the caries process (Angmar-Mansson and ten Bosch 2001).

There has been extensive research to employ QLF as a lesion activity assessment tool (Amaechi and Higham 2002, Ando et al. 2006, Gomez et al. 2014). Amaechi et al. concluded that QLF could be used to detect and longitudinally monitor the progression or remineralization of incipient caries although the presence of saliva, plaque or stain can confound the results (Amaechi and Higham 2002). In another study,

Ando et al. used QLF as a real-time assessment tool for caries lesion activity status by measuring the fluorescence radiance change during dehydration (Ando et al. 2006). However, these studies focused on smooth surface enamel lesions and assessment of occlusal or root caries lesions using QLF has not been investigated. In addition, QLF has not been successfully applied to imaging interproximal caries lesions and lacks information on the structure and depth of the lesion. Since the fluorescence signal depends on the total enamel thickness and imaging angle, highly convoluted surfaces such as occlusal surface of a tooth hinder the diagnostic capabilities of QLF (Ando et al. 2003, Ando et al. 2004). Further investigations are required to fully evaluate the feasibility and the potential of QLF in assessing caries lesion activity.

1.4.2 Pulse Thermography

Pulse thermography has been proposed as a quantitative and nondestructive method to evaluate the different mineralization state of enamel (Ando et al. 2012). When an external excitation energy (a pulse heat flux) is applied to a sample, internal excitation from the sample can be generated based on the subsurface structure of the sample. If the sample contains internal defects, such as pores within the demineralized enamel, a localized high temperature can be captured due to the insulation effect of the defects (Ando et al. 2012). Therefore, remineralized enamel, which contains significantly less porosity compared to demineralized enamel, is expected to exhibit less internal thermal excitation compared to demineralized enamel. Ando et al. showed that pulse thermography has the potential to detect a difference in mineralization status of enamel by measuring the thermal response upon a heat flash (Ando et al. 2012). This

technology is in a very early stage of development, and further experiments and validations are required to evaluate the efficacy and feasibility of this method.

1.5 Infrared Methods for Caries Lesion Activity Assessment

Infrared imaging has the potential for replacing radiography for the routine screening for caries lesions on the proximal and occlusal surfaces where almost all lesions are found (Staninec et al. 2010, Zakian et al. 2010, Staninec et al. 2011). The risk of low-level exposure to ionizing radiation is not well understood; even greatly reduced levels of radiation exposure may still pose a significant risk especially for children and pregnant women. Another major limitation of radiographs is that they cannot be used to detect early occlusal caries lesions because of the overlapping features of the tooth crown. It is unlikely that improvements in radiographic sensitivity will enable detection of early enamel lesions because of this problem.

Accurate determination of the degree of lesion activity and severity is of paramount importance for the effective employment of new optical diagnostic technologies. Since optical diagnostic tools exploit changes in the light scattering of the lesion they have great potential for the diagnosis of the current "state of the lesion", i.e., whether or not the caries lesion is active and expanding or whether the lesion has been arrested and is undergoing remineralization. Therefore, new technologies should be able to determine whether caries lesions have been partially remineralized and have become arrested. Polarization sensitive optical coherence tomography (PS-OCT) is uniquely capable of this task since it provides a measure of the reflectivity from each layer of the lesion and is able to show the formation of a zone of increased mineral

density and reduced light scattering due to remineralization (Jones et al. 2006, Jones and Fried 2006, Manesh et al. 2009). This is a very important distinction between PS-OCT and other optical methods, such as the Diagnodent and QLF, that only provide a single measure of lesion severity representing change in fluorescence from the lesion and are not capable of resolving the lesion structure in depth. Although recent efforts in QLF development have focused on using other means to show the presence of a surface zone which involve hydration and dehydration of the lesion during image acquisition (Ando et al. 2006), it is more advantageous to be able to acquire unequivocal in depth images of the lesion structure (van der Veen et al. 1999). Such data is also invaluable for caries management by risk assessment in the patient and for determining the appropriate form of intervention.

Many lesions have been arrested or are developmental defects and do not require intervention. New methods are needed to assess lesion activity and avoid unnecessary cavity preparations. Near-infrared (NIR) and thermal imaging methods should allow more frequent monitoring of lesions, since ionizing radiation is not required, and previous studies suggest that NIR imaging may be able to differentiate active and more severe lesions from developmental defects (Hirasuna et al. 2008).

These novel-imaging technologies can be employed for the detection and monitoring of early carious lesions without the use of ionizing radiation, thereby enabling conservative non-surgical intervention and the preservation of healthy tissue structure.

1.5.1 PS-OCT

OCT is a non-invasive technique for creating cross-sectional images of internal biological structures. Several studies both *in-vitro* and *in-vivo* have demonstrated that PS-OCT is uniquely capable of this task since it provides a measurement of the reflectivity from each layer of the lesion and is able to show the formation of a zone of increased mineral density and reduced light scattering due to remineralization (Amaechi et al. 2001, Fried et al. 2002, Jones et al. 2006, Louie et al. 2010). Polarization sensitivity is particularly valuable for resolving the structure of early caries lesions. PS-OCT images are typically processed in the form of phase and intensity images, and such images best show variations in the birefringence of the tissues (Baumgartner et al. 1998, Baumgartner et al. 2000). Caries lesions strongly scatter incident polarized light and the image in the orthogonal polarization axis to that of the incident polarization can provide improved lesion contrast.

There are two mechanisms in which the intensity can arise in the cross-polarization axis. The native birefringence of the tooth enamel can rotate the phase angle of the incident light beam between the two cross-polarization axes as the light propagates through the enamel without changing the degree of polarization. The other mechanism is the scattering of incident light in which the degree of polarization is reduced. It is this mechanism that is exploited to measure the severity of demineralization. Strong scattering of the incident linearly polarized light scrambles the polarization and leads to equal distribution of the intensity in both orthogonal polarization axes. Demineralization of the enamel due to dental decay causes an increase in the scattering coefficient by 1-2 orders of magnitude (Darling et al. 2006).

This in turn causes a large rise in reflectivity in the cross-polarization axis. This approach also has the advantage of reducing the intensity of the strong surface reflection from the tooth allowing measurement of the lesion surface zone. A conventional OCT system is susceptible to strong Fresnel surface reflectance that can mask or resemble increased reflectivity from the lesion itself. Varying the angle of incidence and topical application of high index agents may be employed to mitigate the effect of the strong surface reflection in conventional OCT systems (Jones and Fried 2005, Nam et al. 2011).

The reflectivity in the cross-polarization OCT (CP-OCT) images can be directly integrated to quantify the lesion severity, regardless of the tooth topography. By using this approach, the difficult task of deconvolving the strong surface reflection from the lesion surface can be circumvented. We have demonstrated in several studies that the lesion severity can be represented by the integrated reflectivity with depth in the CP-OCT image and the integrated reflectivity, ΔR , is analogous to the integrated mineral loss, ΔZ , obtained from TMR (Arends et al. 1997, Ngaotheppitak et al. 2005, Jones et al. 2006, Chong et al. 2007). The presence of a surface zone of reduced light scattering in the OCT image may indicate that the lesion is arrested. PS-OCT images are particularly valuable for resolving these highly mineralized surface layers since the image in the incident polarization shows the position of the tooth surface while the image in the cross-polarization shows the body of the subsurface lesion.

PS-OCT can be used to nondestructively image the subsurface structure and measure the thickness of the highly mineralized surface zone of caries lesions (Can et al. 2008). This surface zone is of particular importance for differentiating active lesions

from developmental defects, such as hypomineralization typically caused by fluorosis, and those lesions that have become arrested due to remineralization. Since PS-OCT can resolve changes in lesion structure, i.e., show a surface zone of reduced light scattering, it can be used as a quantitative diagnostic of the activity of the lesion or as an indicator of an arrested lesion or a developmental defect that needs no further intervention (Kidd 1983, Fejerskov and Kidd 2003). Developmental defects typical of mild fluorosis show a relatively thick transparent (weakly scattering/reflective) outer layer that has a higher mineral content than the hypomineralized body of the defect. This outer region of low reflectivity can be resolved in the PS-OCT images (Hirasuna et al. 2008).

Previous studies have shown that the remineralization of smooth enamel surfaces can be achieved by employing two caries models; the first model involves pH cycling to produce lesions with a well-defined surface zone of intact enamel while the second model uses a different demineralization model to produce a surface softened lesion (Jones et al. 2006, Jones and Fried 2006). Both models showed markedly different outcomes after exposure to the remineralization solution (Jones and Fried 2006). PS-OCT images of a surface softened lesion before and after remineralization in **Fig. 1.1** show that there was significant growth in the thickness of a transparent remineralized enamel layer with a concomitant decrease in the integrated reflectivity (Kang et al. 2011). In that study, the mean surface layer thickness increased significantly from $10 \pm 4 \mu\text{m}$ for the lesion before remineralization to $33 \pm 5 \mu\text{m}$ after 20 days of immersion in the remineralization solution at neutral pH, $p < 0.05$ ($n = 10$). The mean integrated reflectivity of the lesion, ΔR ($\text{dB} \times \mu\text{m}$), also decreased significantly by

31%. Another study monitored the remineralization progression after immersing the bovine enamel blocks in an acidic remineralization solution at pH 4.8 following demineralization via surface softening subsurface lesion model for three 4-day periods (Kang et al. 2011). The integrated reflectivity from the body of the lesion decreased by 35% for the ten samples after a period of only 12 days.

Even though the penetration of NIR light is markedly reduced in dentin due to higher light scattering and absorption, PS-OCT can effectively be used to discriminate demineralized dentin from sound dentin and cementum (Lee et al. 2009). Furthermore, PS-OCT has also been used to measure remineralization on dentin surfaces and OCT images such as those in **Fig. 1.2** show optical changes that are even more dramatic than we have observed for enamel (Manesh et al. 2009). Not only do the PS-OCT images show a reduction in the reflectivity of the lesion area indicating remineralization but the images also show the growth of a transparent layer on the surface. In addition, dentin contains a high percentage of collagen, demineralized areas exhibited considerable shrinkage if not immersed in water. The amount of shrinkage in artificially demineralized dentin was proportional to the integrated mineral loss, ΔZ with a high correlation ($R = 0.82$) between the shrinkage and ΔZ (Manesh et al. 2009). Moreover, there is no shrinkage of the dentin after remineralization. Thus, it is speculated that active dentin lesions will exhibit significantly greater shrinkage than arrested lesions. Hence, PS-OCT is capable of measuring remineralization non-destructively on both enamel and dentin surfaces.

1.5.2 Near-infrared Reflectance Imaging with Dehydration

Fluorescence imaging methods have been used as a potential diagnostic tool for hypomineralization because the subsurface porosities scatter light in a similar manner to demineralized carious lesions (Li et al. 2003, Ando et al. 2006). Previous studies show that NIR imaging can be also applied in reflectance mode, providing similar information to fluorescence loss measurements (Wu and Fried 2009).

A previous study showed that the mean attenuation coefficient of enamel increased significantly from 2.12 ± 0.82 to 5.08 ± 0.98 ($n = 6$) at 1310-nm with loss of mobile water due to heating (Maung et al. 2010). Recent studies at near-IR wavelengths coincident with high water absorption, i.e. 1460 nm and > 1500 -nm for artificial and natural lesions demonstrated extremely high lesion contrast (Chung et al. 2011, Fried et al. 2013, Simon et al. 2014). This suggests that changes in water content have a more profound effect on enamel transparency at NIR wavelengths than in the visible. Zakian et al. carried out near-IR reflectance measurements from 1000 – 2500 nm using a hyperspectral imaging system and showed that the reflectance from sound tooth areas decreases at longer wavelengths where water absorption is higher (Zakian et al. 2009). The attenuation coefficient for dental enamel and the absorption coefficient of water in the visible and NIR are shown in **Fig. 1.3** (Hale and Querry 1973, Fried et al. 1995, Jones and Fried 2002).

Early caries lesions can be described as non-cavitated subsurface lesions with an intact surface layer (Fejerskov and Kidd 2003). The lesion body manifests increased porosity due to mineral loss while the surface layer is maintained due to mineral deposition from the saliva. Mobile water filling the pores of the lesion body can

evaporate through micropores in the surface layer (Zahradnik and Moreno 1977). As the lesion becomes arrested or undergoes remineralization, the permeability of the surface layer significantly decreases (Lepri et al. 2013). Thus, the rate of evaporation of water from the lesion depends on the lesion structure. The influence of hydration and rate of dehydration at NIR wavelengths for caries lesions can be investigated for the activity assessment of caries lesions.

Sound dentin manifests higher scattering and absorption coefficients, almost an order of magnitude higher than enamel, due to the presence of dentinal tubules of 1 – 3 μm in diameter and an organic matrix largely composed of collagen (Chan et al. 2014). The organic scaffold and dentinal tubules are occupied by mostly water when hydrated (Kinney et al. 1993). The capacity of water retention of dentin increases with the increase in severity of demineralization and the size of dentinal tubules (Ozok et al. 2002). Therefore, loss of mobile water from the lesion and sound dentin is likely to be highly dependent on the structure and mineral content of the exposed dentin surface.

1.5.3 Thermal Imaging with Dehydration

Evaporation of water from a lesion is an endothermic process, which causes a temperature decrease followed by a recovery to thermal equilibrium as the lesion becomes dry. Kaneko et al. and Zakian et al. carried out thermal imaging studies using an infrared camera and an air-jet for evaporation on smooth and occlusal natural tooth surfaces (Kaneko et al. 1999, Zakian et al. 2010). ΔQ , the area below the line connecting the initial temperature and final temperature in the time-temperature curve, was used in both studies to measure water evaporated from the sample. From this data

processing step, a two-dimensional ΔQ map can be generated, each pixel representing a ΔQ score. This method of detecting caries lesion has only been employed in detection of enamel caries lesions and has not yet tested on root caries lesions.

In arrested caries lesions, the highly mineralized surface layer inhibits free diffusion of mobile from the lesion body to the outer surface during dehydration; it can be speculated that the water molecules trapped within the lesion body of an arrested caries lesion cannot escape to the outer surface during dehydration. Therefore, the temperature loss due to loss of mobile water from the lesion is likely to be highly dependent on the thickness and mineral content of that highly mineralized surface layer.

1.6 Overall hypothesis and objectives

The overall objective of this proposed research is to develop new nondestructive optical methods for the accurate and early clinical assessment of tooth demineralization and remineralization. It is not sufficient to simply detect caries lesions, methods are needed to assess the activity of the lesion and to determine if chemical intervention is needed. The central hypothesis underlying this proposal is that there are structural differences between active lesions due to caries, arrested lesions and developmental defects, and these differences can be resolved nondestructively using optical imaging methods at infrared wavelengths. Arrested lesions and developmental defects of enamel can be easily mistaken for active early caries lesions due to similar texture and color. Arrested lesions and mild developmental defects typically have a hard outer layer or surface zone of higher mineral content than the body of the lesion which will reduce the lesion permeability.

Active lesions have a higher porosity than arrested lesions and they have a different structure. Arrested lesions have a highly mineralized outer layer that renders the lesion less permeable to fluids (Fejerskov and Kidd 2003). It is hypothesized that those structural differences lead to changes in optical behavior that can be detected using PS-OCT and infrared methods. Studies have established that PS-OCT is capable of non-destructive measurement of the formation of a highly mineralized surface layer on both enamel and dentin after remineralization. It is hypothesized that 1460 nm is best suited for assessing the hydration status of the lesion because there is a broad water absorption peak at 1420 – 1500 nm. To accurately diagnose lesion activity, artificial demineralization and remineralization models will be used to create lesions with different states of remineralization. The thickness of the remineralization layer will be measured using PS-OCT and the rate of water loss will be monitored using NIR reflectance and thermal imaging. Natural coronal and root caries lesions will be evaluated via NIR optical methods and will be correlated with visual methods of lesion activity assessment (ICDAS II) and with histology. The ability to assess lesion activity nondestructively in a single measurement will be a major advantage for lesion diagnosis and for assessing caries risk.

1.7 FIGURES AND FIGURE LEGENDS

Table 1.1 Classification of coronal caries lesion in ICDAS II

	Active	Arrested
Color	White - Yellow	Yellow - Brown
Appearance	Chalky	Shiny
Cavitation	Can be cavitated or non-cavitated	Can be cavitated or non-cavitated
Location	Higher chance in PSA*	Higher chance in non-PSA*
Texture	Rough	Smooth

*PSA (plaque stagnation area): along the gingival margins, below or above approximal contact points and in the groove-fossa systems (Ekstrand et al. 2009)

Table 1.2 Classification of root caries lesion in ICDAS II

	Active	Arrested
Color	Yellow – Light brown	Brown - Black
Appearance	Matte	Shiny
Cavitation	Can be cavitated or non-cavitated	Most likely cavitated
Location	Higher chance in PSA*	Higher chance in non-PSA*
Texture	Soft / Leathery	Hard

*PSA (plaque stagnation area): along the gingival margins, below or above approximal contact points and in the groove-fossa systems (Ekstrand et al. 2009)

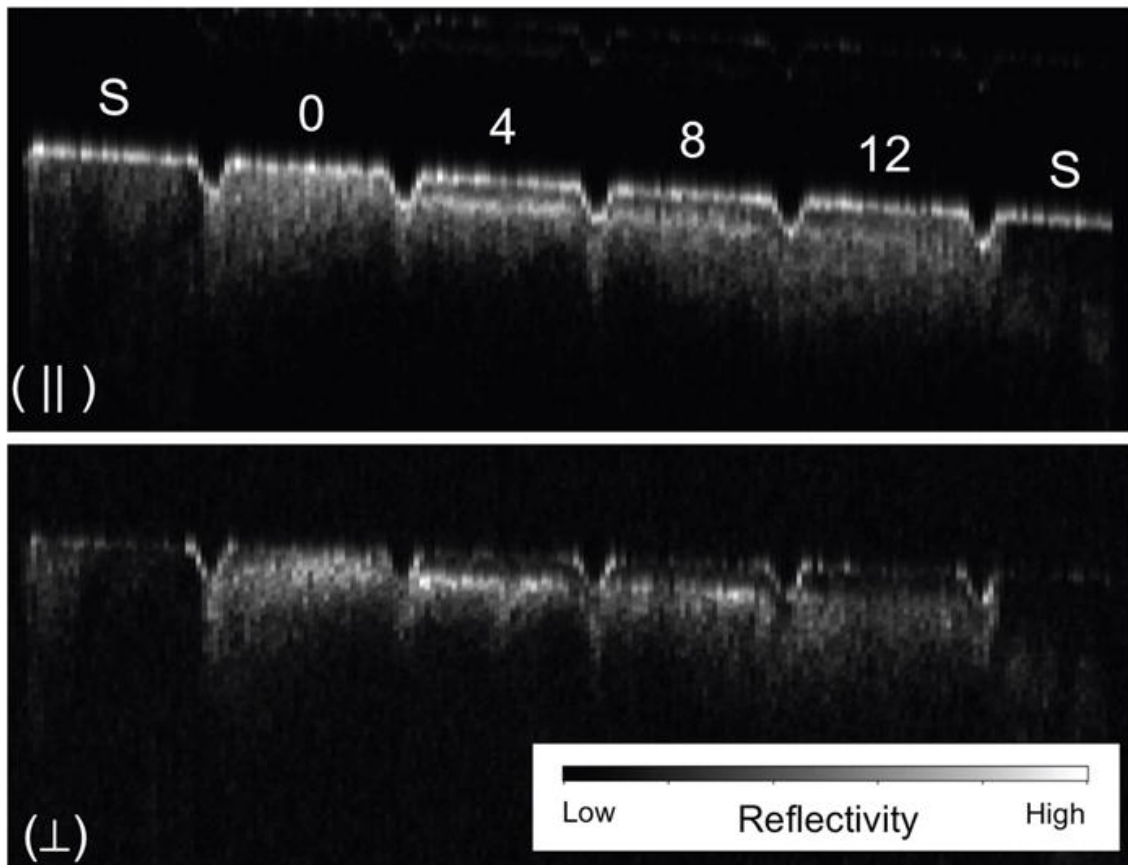


Figure 1.1 PS-OCT b-scan images of a sample after exposure to the remineralizing solution (Kang et al. 2011). Area labeled (S) is sound, and demineralized areas were exposed to increasing periods of time in the remineralization solution, 0, 4, 8, and 12-days. The (||) image represents the light reflected in the original polarization while the (⊥) image is the orthogonal polarization or cross polarization image.

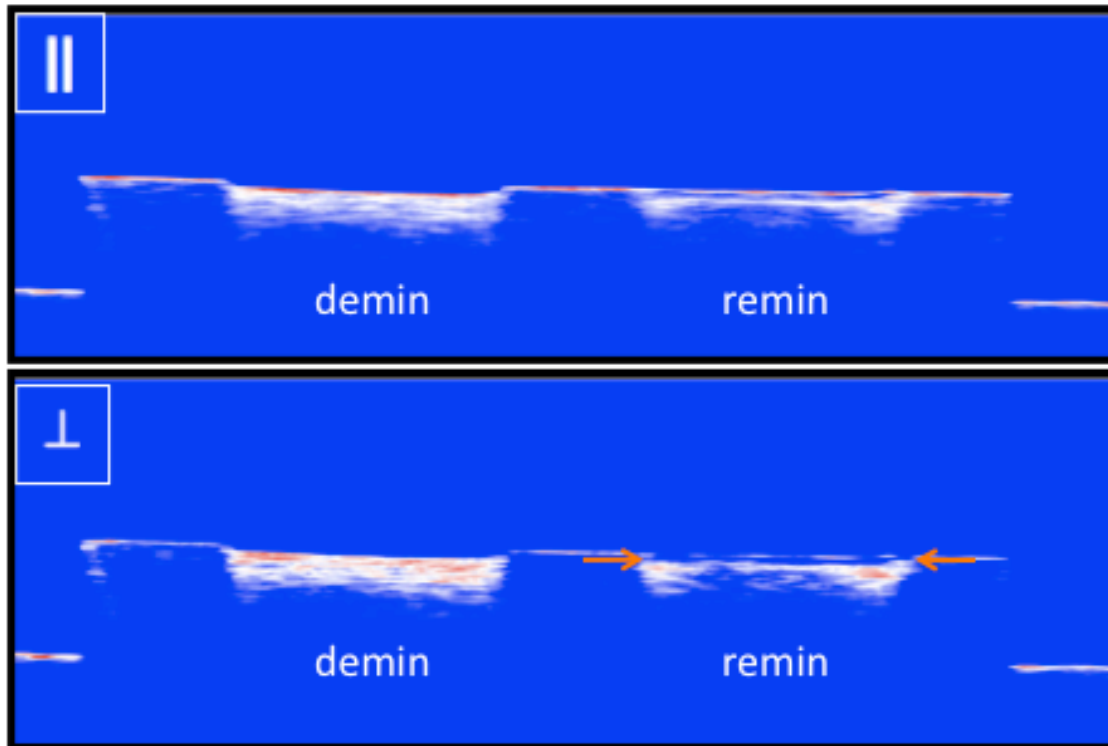


Figure 1.2 PS-OCT (\parallel) and (\perp) images taken of a dentin sample after immersion in demineralization solution (left) and a demineralization solution followed by immersion in a remineralization solution (right) (Manesh et al. 2009). Note the growth of a transparent surface zone on the lesion at the position of the arrows after exposure to the remineralizing solution. Areas in between the lesions and on both ends of the sample were covered with acid resistant varnish to serve as sound reference areas for comparison. The apparent depression in the demineralized areas is not cavitation; it is due to shrinkage of the dentin.

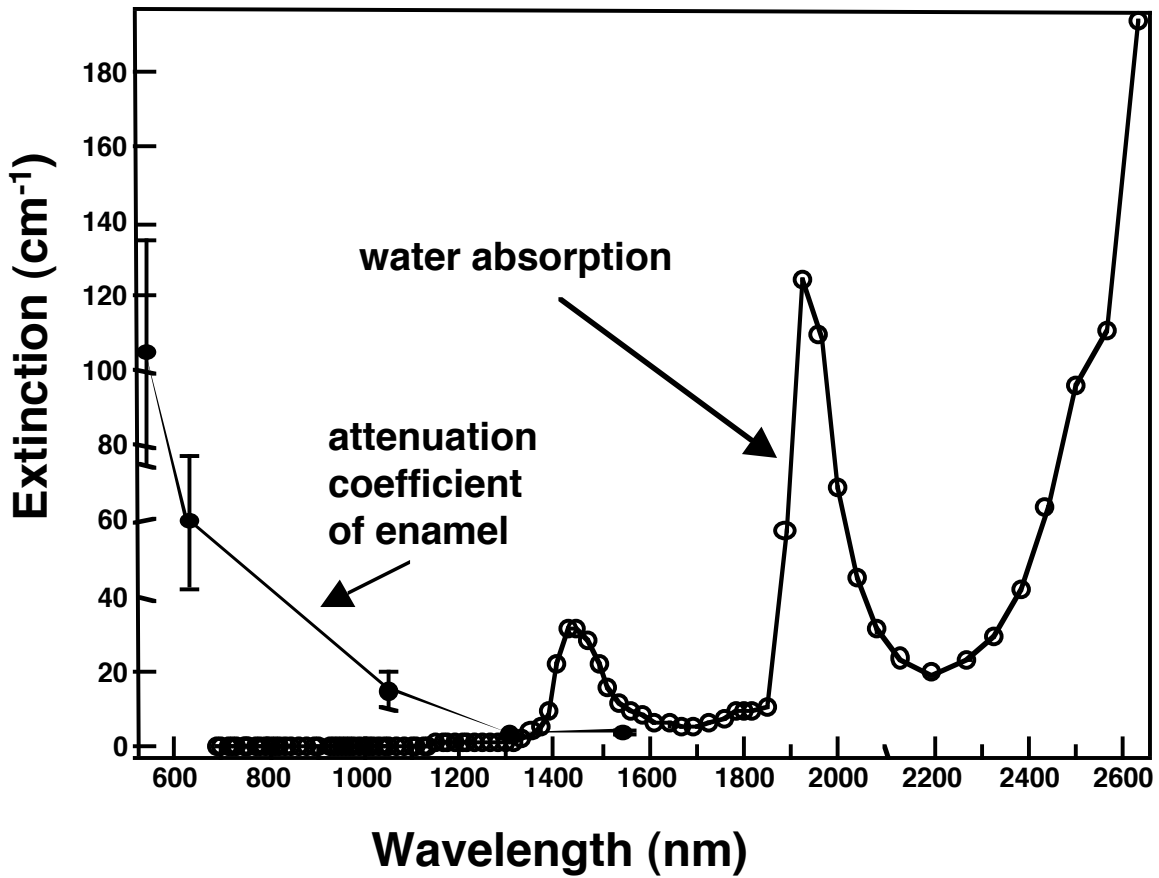


Figure 1.3 The attenuation coefficient for dental enamel and the absorption coefficient of water in the visible and NIR (Hale and Querry 1973, Fried et al. 1995, Jones and Fried 2002).

1.8 REFERENCES

- Alfano, R. R. and Yao, S. S. (1981). Human teeth with and without dental caries studied by visible luminescent spectroscopy. *J. Dent. Res.*, **60**(2): 120-122.
- Amaechi, B. T. and Higham, S. M. (2002). Quantitative light-induced fluorescence: a potential tool for general dental assessment. *J. Biomed. Opt.*, **7**(1): 7-13.
- Amaechi, B. T., Higham, S. M., Podoleanu, A. g., Rodgers, J. A. and Jackson, D. A. (2001). Use of Optical Coherence Tomography for Assessment of Dental caries. *J. Oral. Rehab.*, **28**(12): 1092-1093.
- Ando, M., Eckert, G. J., Stookey, G. K. and Zero, D. T. (2004). Effect of imaging geometry on evaluating natural white-spot lesions using quantitative light-induced fluorescence. *Caries Res.*, **38**(1): 39-44.
- Ando, M., Schemehorn, B. R., Eckert, G. J., Zero, D. T. and Stookey, G. K. (2003). Influence of enamel thickness on quantification of mineral loss in enamel using laser-induced fluorescence. *Caries Res.*, **37**(1): 24-28.
- Ando, M., Sharp, N. and Adams, D. (2012). Pulse thermography for quantitative nondestructive evaluation of sound, de-mineralized and re-mineralized enamel. *Proc. SPIE Health Monitoring of Structural and Biological Systems I*, San Diego, CA, **8348**: S1-7.
- Ando, M., Stookey, G. K. and Zero, D. T. (2006). Ability of quantitative light-induced fluorescence (QLF) to assess the activity of white spot lesions during dehydration. *Am. J. Dent.*, **19**(1): 15-18.
- Angmar-Mansson, B. and ten Bosch, J. J. (2001). Quantitative light-induced fluorescence (QLF): a method for assessment of incipient caries lesions. *Dentomaxillofac. Radiol.*, **30**(6): 298-307.
- Arends, J., Ruben, J. L. and Inaba, D. (1997). Major topics in quantitative microradiography of enamel and dentin: R parameter, mineral distribution visualization, and hyper-remineralization. *Adv. Dent. Res.*, **11**(4): 403-414.
- Banting, D. W. (1993). Diagnosis and prediction of root caries. *Adv. Dent. Res.*, **7**(2): 80-86.
- Banting, D., Eggertsson, H., Ekstrand, K. R., Ferreira-Zandona, A., Ismail, A. I., Longbottom, C., Pitts, N., Reich, E., Ricketts, D., Selwitz, R., Sohn, W., Topping, G. and Zero, D. (2005). Rationale and evidence for the International Caries Detection and Assessment System (ICDAS II). *Proc. the 7th Annual Indiana Conference: Clinical Models Workshop: Remin-Demin, Precavitation, Caries*, Indianapolis, IN, 161-221.

Baumgartner, A., Dicht S., Hitzenberger, C. K., Sattmann, H., Robi, B., Moritz, A., Sperr, W. and Fercher, A. F. (2000). Polarization-sensitive optical coherence tomography of dental structures. *Caries Res.*, **34**: 59-69.

Baumgartner, A., Hitzenberger, C. K., Dicht, S., Sattmann, H., Moritz, A., Sperr, W. and Fercher, A. F. (1998). Optical coherence tomography for dental structures. *Proc. SPIE Lasers in Dentistry IV*, San Jose, CA, **3248**: 130-136.

Beighton, D., Lynch, E. and Heath, M. R. (1993). A microbiological study of primary root-caries lesions with different treatment needs. *J. Dent. Res.*, **72**(3): 623-629.

Bjelkhagen, H., Sundstrom, F., Angmar-Mansson, B. and Ryden, H. (1982). Early detection of enamel caries by the luminescence excited by visible laser light. *Swed. Dent. J.*, **6**(1): 1-7.

Can, A. M., Darling, C. L. and Fried, D. (2008). High-resolution PS-OCT of enamel remineralization. *Proc. SPIE Lasers in Dentistry XIV*, San Jose, CA, **6843**: T1-7.

Chan, K. H., Chan, A. C., Fried, W. A., Simon, J. C., Darling, C. L. and Fried, D. (2013). Use of 2D images of depth and integrated reflectivity to represent the severity of demineralization in cross-polarization optical coherence tomography. *J. Biophotonics*, **8**: 36-45.

Chauncey, H. H., Glass, R. L. and Alman, J. E. (1989). Dental caries, principal cause of tooth extraction in a sample of US male adults. *Caries Res.*, **23**(3): 200-205.

Chong, S. L., Darling, C. L. and Fried, D. (2007). Nondestructive measurement of the inhibition of demineralization on smooth surfaces using polarization-sensitive optical coherence tomography. *Lasers Surg. Med.*, **39**(5): 422-427.

Chung, S., Fried, D., Staninec, M. and Darling, C. L. (2011). Multispectral near-IR reflectance and transillumination imaging of teeth. *Biomed. Opt. Express*, **2**(10): 2804-2814.

Darling, C. L., Huynh, G. D. and Fried, D. (2006). Light scattering properties of natural and artificially demineralized dental enamel at 1310 nm. *J. Biomed. Opt.*, **11**(3): 34023.

Denbesten, P. and Li, W. (2011). Chronic fluoride toxicity: dental fluorosis. *Monogr. Oral Sci.*, **22**: 81-96.

Ekstrand, K., Martignon, S. and Holm-Pedersen, P. (2008). Development and evaluation of two root caries controlling programmes for home-based frail people older than 75 years. *Gerodontology*, **25**(2): 67-75.

- Ekstrand, K. R., Ricketts, D. N., Longbottom, C. and Pitts, N. B. (2005). Visual and tactile assessment of arrested initial enamel carious lesions: an in vivo pilot study. *Caries Res.*, **39**(3): 173-177.
- Ekstrand, K. R., Zero, D. T., Martignon, S. and Pitts, N. B. (2009). Lesion activity assessment. *Monogr. Oral Sci.*, **21**: 63-90.
- Featherstone, J. D. (2000). The science and practice of caries prevention. *J. Am. Dent. Assoc.*, **131**(7): 887-899.
- Featherstone, J. D. (2008). Dental caries: a dynamic disease process. *Aust. Dent. J.*, **53**(3): 286-291.
- Featherstone, J. D. B., Glena, R., Shariati, M. and Shields, C. P. (1990). Dependence of *in vitro* demineralization and remineralization of dental enamel on fluoride concentration. *J. Dent. Res.*, **69**: 620-625.
- Featherstone, J. D. B. (1996). Clinical implications: new strategies for caries prevention. *Proc. the 1st Annual Indiana Conference: Early Detection of dental caries*, Indianapolis, IN, 287-296.
- Featherstone, J. D. B. (1999). Prevention and reversal of dental caries: role of low level fluoride. *Community Dent. Oral. Epidemiol.*, **27**(1): 31-40.
- Fejerskov, O. and Kidd, E., Eds. (2003). Dental caries: the disease and its clinical management. Oxford, Blackwell.
- Fried, D., Featherstone, J. D. B., Glena, R. E. and Seka, W. (1995). The nature of light scattering in dental enamel and dentin at visible and near-IR wavelengths. *Appl. Optics*, **34**(7): 1278-1285.
- Fried, D., Xie, J., Shafi, S., Featherstone, J. D. B., Breunig, T. M. and Le, C. Q. (2002). Early detection of dental caries and lesion progression with polarization sensitive optical coherence tomography. *J. Biomed. Opt.*, **7**(4): 618-627.
- Fried, W. A., Darling, C. L., Chan, K. and Fried, D. (2013). High contrast reflectance imaging of simulated lesions on tooth occlusal surfaces at near-IR wavelengths. *Lasers Surg. Med.*, **45**(8): 533-541.
- Gomez, J., Pretty, I. A., Santarpia, R. P. 3rd, Cantore, B., Rege, A., Petrou, I. and Ellwood, R. P. (2014). Quantitative light-induced fluorescence to measure enamel remineralization in vitro. *Caries Res.*, **48**(3): 223-227.
- Gugnani, N., Pandit, I. K., Gupta, M. and Josan, R. (2012). Caries infiltration of noncavitated white spot lesions: A novel approach for immediate esthetic improvement. *Contemp. Clin. Dent.*, **3**(S2): 199-202.

- Hale, G. M. and Querry, M. R. (1973). Optical constants of water in the 200-nm to 200- μm wavelength region. *Appl. Optics*, **12**(3): 555-563.
- Hellyer, P. H., Beighton, D., Heath, M. R. and Lynch, E. J. (1990). Root caries in older people attending a general dental practice in East Sussex. *Br. Dent. J.*, **169**(7): 201-206.
- Hirasuna, K., Fried, D. and Darling, C. L. (2008). Near-IR imaging of developmental defects in dental enamel. *J. Biomed. Opt.*, **13**(4): 044011.
- Hume, W. R. (1996). Need for change in dental caries diagnosis. *Proc. the 1st Annual Indiana Conference: Early Detection of dental caries*, Indianapolis, IN, 1-10.
- Jones, R. S., Darling, C. L., Featherstone, J. D. B. and Fried, D. (2006). Imaging artificial caries on the occlusal surfaces with polarization-sensitive optical coherence tomography. *Caries Res.*, **40**(2): 81-89.
- Jones, R. S., Darling, C. L., Featherstone, J. D. B. and Fried, D. (2006). Remineralization of in vitro dental caries assessed with polarization sensitive optical coherence tomography. *J. Biomed Opt.*, **11**(1): 014016.
- Jones, R. S. and Fried, D. (2002). Attenuation of 1310-nm and 1550-nm Laser Light through Sound Dental Enamel. *SPIE Lasers in Dentistry VIII*, San Jose, CA, **4610**: 187-190.
- Jones, R. S. and Fried, D. (2005). The effect of high-index liquids on PS-OCT imaging of dental caries. *Proc. SPIE Lasers in Dentistry XI*, San Jose, CA, **5687**: 34-41.
- Jones, R. S. and Fried, D. (2006). Remineralization of enamel caries can decrease optical reflectivity. *J. Dent. Res.*, **85**(9): 804-808.
- Kaneko, K., Matsuyama, K. and Nakashima, S. (1999). Quantification of early carious enamel lesions by using an infrared camera. *Proc. the 4th Annual Indiana Conference: Early Detection of dental caries II*, Indianapolis, IN, 83-99.
- Kang, H., Darling, C. L. and Fried, D. (2011). Repair of Artificial Lesions using an Acidic Remineralization Model Monitored with Cross - Polarization Optical Coherence Tomography. *SPIE Lasers in Dentistry XVII*, San Francisco, CA, **7884**: Q1-7.
- Kassebaum, N. J., Bernabe, E., Dahiya, M., Bhandari, B., Murray, C. J. and Marcenes, W. (2015). Global burden of untreated caries: a systematic review and metaregression. *J. Dent. Res.*, **94**(5): 650-658.
- Kaste, L. M., Selwitz, R. H., Oldakowski, R. J., Brunelle, J. A., Winn, D. M. and Brown, L. J. (1996). Coronal caries in the primary and permanent dentition of children and adolescents 1-17 years of age: United States, 1988-1991. *J. Dent. Res.*, **75**: 631-641.

Kidd, E. A. (1983). The histopathology of enamel caries in young and old permanent teeth. *Br. Dent. J.*, **155**(6): 196-198.

Kinney, J. H., Balooch, M., Marshall, G. W. and Marshall, S. J. (1993). Atomic-force microscopic study of dimensional changes in human dentine during drying. *Arch. Oral Biol.*, **38**(11): 1003-1007.

Lamkin, M. S. and Oppenheim, F. G. (1993). Structural features of salivary function. *Crit. Rev. Oral. Biol. Med.*, **4**(3-4): 251-259.

Lee, C., Darling, C. L. and Fried, D. (2009). Polarization-sensitive optical coherence tomographic imaging of artificial demineralization on exposed surfaces of tooth roots. *Dent. Mater.*, **25**(6): 721-728.

Lepri, T. P., Colucci, V., Turssi, C. P. and Corona, S. A. (2013). Permeability of eroded enamel following application of different fluoride gels and CO₂ laser. *Lasers Med. Sci.*, **28**(1): 235-240.

Li, S. M., Zou, J., Wang, Z., Wright, J. T. and Zhang, Y. (2003). Quantitative assessment of enamel hypomineralization by KaVo DIAGNOdent at different sites on first permanent molars of children in China. *Pediatr. Dent.*, **25**(5): 485-490.

Louie, T., Lee, C., Hsu, D., Hirasuna, K., Manesh, S., Staninec, M., Darling, C. L. and Fried, D. (2010). Clinical assessment of early tooth demineralization using polarization sensitive optical coherence tomography. *Lasers Surg. Med.*, **42**(10): 738-745.

Lynch, E. and Beighton, D. (1994). A comparison of primary root caries lesions classified according to colour. *Caries Res.*, **28**(4): 233-239.

Manesh, S. K., Darling, C. L. and Fried, D. (2009). Nondestructive assessment of dentin demineralization using polarization-sensitive optical coherence tomography after exposure to fluoride and laser irradiation. *J. Biomed. Mater. Res. B Appl. Biomater.*, **90**(2): 802-812.

Manesh, S. K., Darling, C. L. and Fried, D. (2009). Polarization-sensitive optical coherence tomography for the nondestructive assessment of the remineralization of dentin. *J. Biomed. Opt.*, **14**(4): 044002.

Maung, L. H., Lee, C. and Fried, D. (2010). Near-IR Imaging of thermal changes in enamel during laser ablation. *SPIE Lasers in Dentistry XVI*, San Jose, CA, **7549**: 21-26.

Nam, K. H., Jeong, B., Jung, I. O., Ha, H., Kim, K. H. and Lee, S. J. (2011). Measurement of anisotropic reflection of flowing blood using optical coherence tomography. *J. Biomed. Opt.*, **16**(12): 120502.

Ngoatheppitak, P., Darling, C. L. and Fried, D. (2005). Measurement of the severity of natural smooth surface (interproximal) caries lesions with polarization sensitive optical coherence tomography. *Lasers Surg. Med.*, **37**(1): 78-88.

NIH (2001). Diagnosis and management of dental caries throughout life, *NIH Consensus Statement*, **18**: 1-24.

Nyvad, B., Machiulskiene, V. and Baelum, V. (1999). Reliability of a new caries diagnostic system differentiating between active and inactive caries lesions. *Caries Res.*, **33**(4): 252-260.

Nyvad, B., Machiulskiene, V. and Baelum, V. (2003). Construct and predictive validity of clinical caries diagnostic criteria assessing lesion activity. *J. Dent. Res.*, **82**(2): 117-122.

Ozok, A. R., Wu, M. K., ten Cate, J. M. and Wesselink, P. R. (2002). Effect of perfusion with water on demineralization of human dentin in vitro. *J. Dent. Res.*, **81**(11): 733-737.

Simon, J. C., Chan, K. H., Darling, C. L. and Fried, D. (2014). Multispectral near-IR reflectance imaging of simulated early occlusal lesions: Variation of lesion contrast with lesion depth and severity. *Lasers Surg. Med.*, **46**(3): 203-215.

Spitzer, D. and Bosch, J. J. (1976). The total luminescence of bovine and human dental enamel. *Calcif. Tissue Res.*, **20**(2): 201-208.

Staninec, M., Douglas, S. M., Darling, C. L., Chan, K., Kang, H., Lee, R. C. and Fried, D. (2011). Nondestructive Clinical Assessment of Occlusal Caries Lesions using Near-IR Imaging Methods. *Lasers Surg. Med.*, **43**(10): 951-959.

Staninec, M., Lee, C., Darling, C. L. and Fried, D. (2010). In vivo near-IR imaging of approximal dental decay at 1,310 nm. *Lasers Surg. Med.*, **42**(4): 292-298.

ten Cate, J. M. and Arends, J. (1977). Remineralization of artificial enamel lesions in vitro. *Caries Res.*, **11**(5): 277-286.

ten Cate, J. M. and Duijsters, P. P. (1982). Alternating demineralization and remineralization of artificial enamel lesions. *Caries Res.*, **16**(3): 201-210.

ten Cate, J. M. and Featherstone, J. D. B. (1991). Mechanistic aspects of the interactions between fluoride and dental enamel. *Crit. Rev. Oral Biol. Med.*, **2**: 283-296.

ten Cate, J. M. and van Amerongen, J. P. (1996). Caries Diagnosis: Conventional Methods. *Proc. the 1st Annual Indiana Conference: Early Detection of dental caries*, Indianapolis, IN, 27-37.

Thylstrup, A., Bruun, C. and Holmen, L. (1994). In vivo caries models-mechanisms for caries initiation and arrestment. *Adv. Dent. Res.*, **8**(2): 144-157.

van der Veen, M. H., de Josselin de Jong, E. and Al-Kateeb, S. (1999). Caries Activity Detection by Dehydration with Qualitative Light Fluorescence. *Proc. the 4th Annual Indiana Conference: Early Detection of dental caries II*, Indianapolis, IN, 251-260.

Winn, D. M., Brunelle, J. A., Selwitz, R. H., Kaste, L. M., Oldakowski, R. J., Kingman, A. and Brown, L. J. (1996). Coronal and root caries in the dentition of adults in the United States, 1988-1991. *J. Dent. Res.*, **75**: 642-651.

Wu, J. and Fried, D. (2009). High contrast near-infrared polarized reflectance images of demineralization on tooth buccal and occlusal surfaces at $\lambda = 1310\text{-nm}$. *Lasers Surg. Med.*, **41**(3): 208-213.

Zahradnik, R. T. and Moreno, E. C. (1977). Progressive stages of subsurface demineralization of human tooth enamel. *Arch. Oral. Biol.*, **22**(10-11): 585-591.

Zakian, C., Pretty, I. and Ellwood, R. (2009). Near-infrared hyperspectral imaging of teeth for dental caries detection. *J. Biomed. Opt.*, **14**(6): 064047.

Zakian, C. M., Taylor, A. M., Ellwood, R. P. and Pretty, I. A. (2010). Occlusal caries detection by using thermal imaging. *J. Dent.*, **38**(10): 788-795.

CHAPTER II

AN ALGORITHM FOR DETECTION AND MEASUREMENT OF HIGHLY MINERALIZED SURFACE LAYER WITH POLARIZATION-SENSITIVE OPTICAL COHERENCE TOMOGRAPHY

2.1 SUMMARY

Previous *in-vitro* and *in-vivo* studies have demonstrated that polarization-sensitive optical coherence tomography (PS-OCT) can be used to nondestructively image the subsurface structure and measure the thickness of the highly mineralized transparent surface zone of caries lesions. There are structural differences between active lesions and arrested lesions, and the surface layer thickness may correlate with activity of the lesion. The purpose of this work was to develop an algorithm that can be used to automatically detect and measure the thickness of the transparent surface layer in PS-OCT images. Automated methods of analysis were used to measure the thickness of the transparent layer and the depth of the bovine enamel lesions produced using simulated caries models that emulate demineralization in the mouth. The transparent layer thickness measured with PS-OCT correlated well with polarization light microscopy (PLM) measurements of all regions ($R^2 = 0.9213$). This chapter demonstrates that the PS-OCT algorithm can be used to automatically detect and measure thickness of the transparent layer formed due to remineralization in simulated caries lesions.

2.2 INTRODUCTION

New diagnostic tools are needed for the detection and characterization of caries lesions in the early stages of development (Featherstone 1996, Hume 1996, ten Cate and van Amerongen 1996, NIH 2001). The caries process is potentially preventable and curable. If carious lesions are detected early enough, it is likely that they can be arrested/reversed by non-surgical means through fluoride therapy, anti-bacterial therapy, dietary changes, or by low intensity laser irradiation (Featherstone and Young 1999,

NIH 2001). Therefore, one cannot overstate the importance of detecting the decay in the early stage of development at which point non-invasive preventive measures can be taken to halt further decay.

Accurate determination of the degree of lesion activity and severity is of paramount importance for the effective employment of new optical diagnostic technologies. Since optical diagnostic tools exploit changes in the light scattering of the lesion they have great potential for the diagnosis of the current "state of the lesion", i.e., whether or not the caries lesion is active and expanding or whether the lesion has been arrested and is undergoing remineralization. Therefore, new technologies should be able to determine whether caries lesions have been partially remineralized and have become arrested. Previous studies have demonstrated that polarization sensitive optical coherence tomography (PS-OCT) is uniquely capable of this task since it provides a measure of the reflectivity from each layer of the lesion and is able to show the formation of a zone of increased mineral density and reduced light scattering due to remineralization (Jones et al. 2006, Jones and Fried 2006, Manesh et al. 2009). *In-vitro* measurements of the remineralization of artificial lesions produced on enamel surfaces demonstrated that the thickness of the thin layer of higher mineral content that is typically formed near the lesion surface during the remineralization process can be measured with PS-OCT (Can et al. 2008, Kang et al. 2012). This layer is of considerable importance, since the formation of this layer of fluoroapatite limits diffusion into the lesion leading to the arrest of lesion progression, and the lesion becomes inactive and there is no further need for intervention (Kidd 1983, Fejerskov and Kidd 2003).

Polarization sensitivity is particularly valuable for imaging caries lesions due to the enhanced contrast of caries lesions caused by scattering of the incident light by the lesion and the confounding influence of the strong surface reflectance of the tooth surface is reduced in the cross-polarization (Fried et al. 2002). PS-OCT images are typically processed in the form of phase and intensity images, and such images best show variations in the birefringence of the tissues (Baumgartner et al. 1998, Baumgartner et al. 2000). Caries lesions rapidly scatter incident polarized light and the image orthogonal to that of the incident polarization can provide improved contrast of caries lesions. There are two mechanisms in which intensity can arise in the cross-polarization axis (\perp). The native birefringence of the tooth enamel can rotate the phase angle of the incident light beam between the two cross-polarization axes (similar to a wave-plate) as the light propagates through the enamel without changing the degree of polarization. The other mechanism is scattering of incident light in which the degree of polarization is reduced. It is this latter mechanism that is exploited to measure the severity of demineralization. Strong scattering of the incident linearly polarized light scrambles the polarization and leads to equal distribution of the intensity in both cross-polarization axes. Demineralization of the enamel due to dental decay causes an increase in the scattering coefficient by a 1-2 orders of magnitude, thus demineralized enamel induces a very large increase in the reflectivity along with scattering of the polarized light (Darling et al. 2006). This in turn causes a large rise in reflectivity in the cross-polarization channel or axis.

This approach also has the added advantage of reducing the intensity of the strong reflection from the tooth surface for measurement of the lesion surface zone that

can potentially provide information about the lesion activity and remineralization. A conventional OCT system cannot differentiate the strong reflectance from the tooth surface from increased reflectivity from the lesion itself. The reflectivity in the cross-polarization can be directly integrated to quantify the lesion severity, regardless of the tooth topography. By using this approach, the difficult task of deconvolving the strong surface reflection from the lesion surface can be circumvented. By exploiting scattering of polarized light in the cross-polarization axis and strong surface reflection in the co-polarization axis (\parallel) of the PS-OCT system we can quantify thickness of the transparent surface layer on highly convoluted surfaces.

We previously developed approaches to automatically quantify the severity and the depth of demineralized enamel lesions for rapid image processing of large 2D or 3D data sets (Le et al. 2010). This chapter presents and evaluates an approach to automatically detect and measure the thickness of the transparent surface layer in simulated enamel lesions.

2.3 MATERIALS AND METHODS

2.3.1 Sample Preparation and Simulated Lesion Models

Enamel blocks, approximately 8–12-mm in length with a width of 3-mm and a thickness of 2-mm were prepared from extracted bovine incisors acquired from a slaughterhouse. Each enamel and bovine sample was partitioned into six regions or windows (2 sound and 4 lesion regions) by etching small incisions 1.8-mm apart across each of the enamel blocks using a laser. Incisions were etched using a transverse excited atmospheric pressure (TEA) CO₂ laser, an Impact 2500, GSI Lumonics (Rugby, UK),

operating at 9.3- μm with a pulse duration of 15-s and a pulse repetition rate of 200-Hz. A thin layer of acid-resistant varnish in the form of red nail polish, Revlon (New York, NY) was applied to protect the sound control area on each end of the block before exposure to the demineralization solution. The enamel blocks were exposed to a demineralization solution at pH 4.9 composed of a 40-mL aliquot of 2.0-mmol/L calcium, 2.0-mmol/L phosphate, and 0.075-mol/L acetate for 24h. Acid-resistant varnish was applied to the windows for 0-day, 4-day, 8-day and 12-day periods of remineralization. The blocks were placed into the remineralization solution composed of 1.5-mmol/L calcium, 0.9-mmol/L phosphate, 150-mmol/L KCl, 2-ppm F^- , and 20-mmol/L HEPES buffer maintained at pH 7.0 and 37° C. After the fourth period, the samples were removed from the remineralization solution, and the acid resistant varnish was removed using acetone in ultrasonic machine for 15 minutes. Each sample was then stored in 0.1% thymol solution to prevent fungal and bacterial growth. The groups overlapped each other by one period, so that they could be compared to ensure consistency.

2.3.2 PS-OCT System

An all fiber-based Optical Coherence Domain Reflectometry (OCDR) system with polarization maintaining (PM) optical fiber, high speed piezoelectric fiber-stretchers and two balanced InGaAs receivers that was designed and fabricated by Optiphase, Inc., Van Nuys, CA was used to acquire the images. This two-channel system was integrated with a broadband superluminescent diode (SLD) Denselight (Jessup, MD) and a high-speed XY-scanning system (ESP 300 controller & 850G-HS stages, National Instruments, Austin, TX) for *in vitro* optical tomography. This system is based on a

polarization-sensitive Michelson white light interferometer. The high power (15-mW) polarized SLD source operated at a center wavelength of 1317 nm with a spectral bandwidth FWHM of 84 nm provided an axial resolution of 9- μ m in air and 6- μ m in enamel (refractive index = 1.6). This light was aligned with the slow axis of the PM fiber of the source arm of the interferometer. The sample arm was coupled to an AR coated fiber-collimator to produce a 6-mm in diameter, collimated beam. That beam was focused onto the sample surface using a 20-mm focal length AR coated plano-convex lens. This configuration provided axial and lateral resolution of approximately 20 μ m with a signal to noise ratio of greater than 40–50 dB. The all-fiber OCDR system is described in reference (Bush et al. 2000). The PS-OCT system is completely controlled using Labview™ software (National Instruments, Austin, TX).

2.3.3 Polarized Light Microscopy

After sample imaging was completed, approximately 200 μ m thick serial sections were cut using an Isomet 5000 saw (Buehler, IL), for polarized light microscopy (PLM). PLM was carried out using a Meiji Techno RZT microscope (Meiji Techno Co., LTD, Saitama, Japan) with an integrated digital camera, Canon EOS Digital Rebel XT (Canon Inc., Tokyo, Japan). The sample sections were imbibed in water and examined in the brightfield mode with crossed polarizers and a red I plate with 500-nm retardation.

2.3.4 Phase Adjustment

There is a difference in phase between the co- and cross-polarization. In order to account for this problem, a gold mirror was scanned at 100- μm intervals over the entire scan range to determine the required phase adjustments.

2.3.5 Image Processing

Images obtained from the PS-OCT scans were processed using a dedicated program constructed with LabviewTM software (National Instruments, Austin, TX). **Figure 2.1** illustrates diagram of steps involved in image processing. The improved automated image processing method is based on the previous study (Le et al. 2010). The cross-polarization scan images were adjusted to match the co-polarization scan images in z-axis position based on the phase adjustment Gaussian curve. The images were filtered with 5x5 median filter to reduce the speckle noise and convolved with 5x5 Gaussian matrix filter. Each scan had background removed by subtracting the mean reflectivity of the 200 data points measured in air from the unprocessed 50 a-scans. In addition, noise threshold was calculated and applied to images as 4-standard deviation of the same 200 data points acquired previously.

2.3.6 Edge Detection, Artifact Removal and Integrated Reflectivity

An edge locator was used to make two passes along each line. Each pass starts from the position of the maximum peak intensity and locates the first pixel, for which the intensity value is less than e^{-2} multiplied by the maximum peak intensity. All other pixels outside of the edges were set to 0 to the artifacts. Lesion depth was estimated by

measuring the distance between two edges. The distance between those positions was correlated and corrected with data previously analyzed (Chan et al. 2013). The reflectivity was integrated over the lesion depth from the top edge to yield the integrated reflectivity (dB x microns), ΔR . Previous studies have shown that ΔR positively correlates with the integrated mineral loss (volume % mineral loss x microns), ΔZ (Ngaotheppitak et al. 2005, Jones et al. 2006).

2.3.7 Transparent Surface Layer Detection and Measurement

In the approach presented in this chapter,

1. First peak at the \parallel axis represents the incident light surface reflection.
2. Second peak at the \parallel axis represents the scattering at the edge of the lesion.
3. If there is only one strong peak at \parallel axis, we assume that the two signals may be overlapping one another, or there is no transparent layer.
4. Strongest peak at the \perp axis represents scattering at the lesion body.

Three different cases are illustrated in **Fig. 2.2**; Case A where no transparent zone is present, Case B where two peaks are present in the \parallel polarization scan clearly indicating the presence of a surface zone, and Case C where the two peaks overlap and the presence of a transparent surface zone is less obvious. In **Fig. 2.2**, α , the difference between the detected front edges of the scans for the two polarization axes is compared with β , the difference in position of the two peaks that represent the lesion body for both polarization axes. If α was greater than β , the transparent surface layer thickness was estimated to be α . Otherwise, there was no transparent surface layer detected.

2.3.8 Statistical Analysis

Sample groups were compared using repeated measures analysis of variance (ANOVA) with a Tukey–Kramer post hoc multiple comparison test. Pearson’s correlation was used to examine the relationship between data acquired from PS-OCT and PLM measurements, including sound, demineralization and remineralization areas. All statistical analyses were performed with 95% confidence with InStat™ (GraphPad software, San Diego, CA).

2.4 RESULTS AND DISCUSSION

The transparent surface layer detection algorithm was able to successfully distinguish lesions with transparent surface layer. All windows that manifested the transparent surface layer with PLM were detected using the algorithm for PS-OCT ($n = 13$). In addition the algorithm also correctly identified windows without the transparent layer with 3 false positives. However, detection of the transparent surface layer with PLM is limited for the shallow transparent surface layer less than $10\mu\text{m}$ due to “edge effect” and the non-uniform advancing front of the lesion on the $200\text{-}\mu\text{m}$ thick samples (Lee et al. 2009). The algorithm detected the transparent surface layer with high sensitivity ($= 1$) and high specificity ($= 0.9286$). **Figure 2.3** shows PS-OCT and PLM images from one of the samples. Linearly polarized light was incident on the sample and the reflected light with polarization \parallel and \perp to the incident light was measured, generating the \parallel and \perp images, respectively. There is minimal reflectivity in the sound regions outside the four lesion windows, while the lesions have much higher contrast in the cross-polarization images. It is obvious how the surface reflection interferes with resolution of the lesion in

the images taken in the original polarization. The strong surface reflection of the co-polarization images can be used for resolving the outer surface of the transparent surface layer of the lesion. The transparent surface layer can be simply estimated by taking the differences in depth between of the top-edges of the two polarization images. However, this method overestimates the thickness of the transparent surface layer and it is unable to differentiate lesions with a transparent surface layer (arrested lesions) from demineralized and sound regions.

With this approach, the optical depth difference between the top-edges of \parallel axis and \perp axis as well as the difference between the lesion of the body and the edge of the lesion or the surface reflection can be calculated. These depth differences can be compared to differentiate the transparent surface layer from sound or demineralized areas. **Figure 2.2** shows 3 different types of a-scan line profiles that can be observed after phase alignment and image processing. A plot of the estimated thickness of the transparent surface layer versus the thickness measured using PLM shown in **Fig. 2.4** indicates strong correlation, Pearson $R^2 = 0.9213$. In addition, the depth of the lesion body under the transparent surface layer could also be estimated incorporating using the edge-detection algorithm. Although the algorithm was successful in differentiating the sound region from lesions, there was no significant difference in lesion depth measurements or lesion severity, ΔR , among groups with different periods of remineralization due to the high variability in the degree of remineralization.

2.5 CONCLUSION

An algorithm was developed to detect and measure the thickness of the transparent surface zone formed due to remineralization using PS-OCT. It was successfully tested using an artificial remineralization model. PS-OCT can be used to non-destructively image the subsurface structure and measure the thickness of the highly mineralized transparent surface zone of caries lesions even with the presence of the very thin transparent surface layer. This method is further tested for a larger number of samples with varying thickness of the transparent surface layer in next chapter.

2.6 FIGURES AND FIGURE LEGENDS

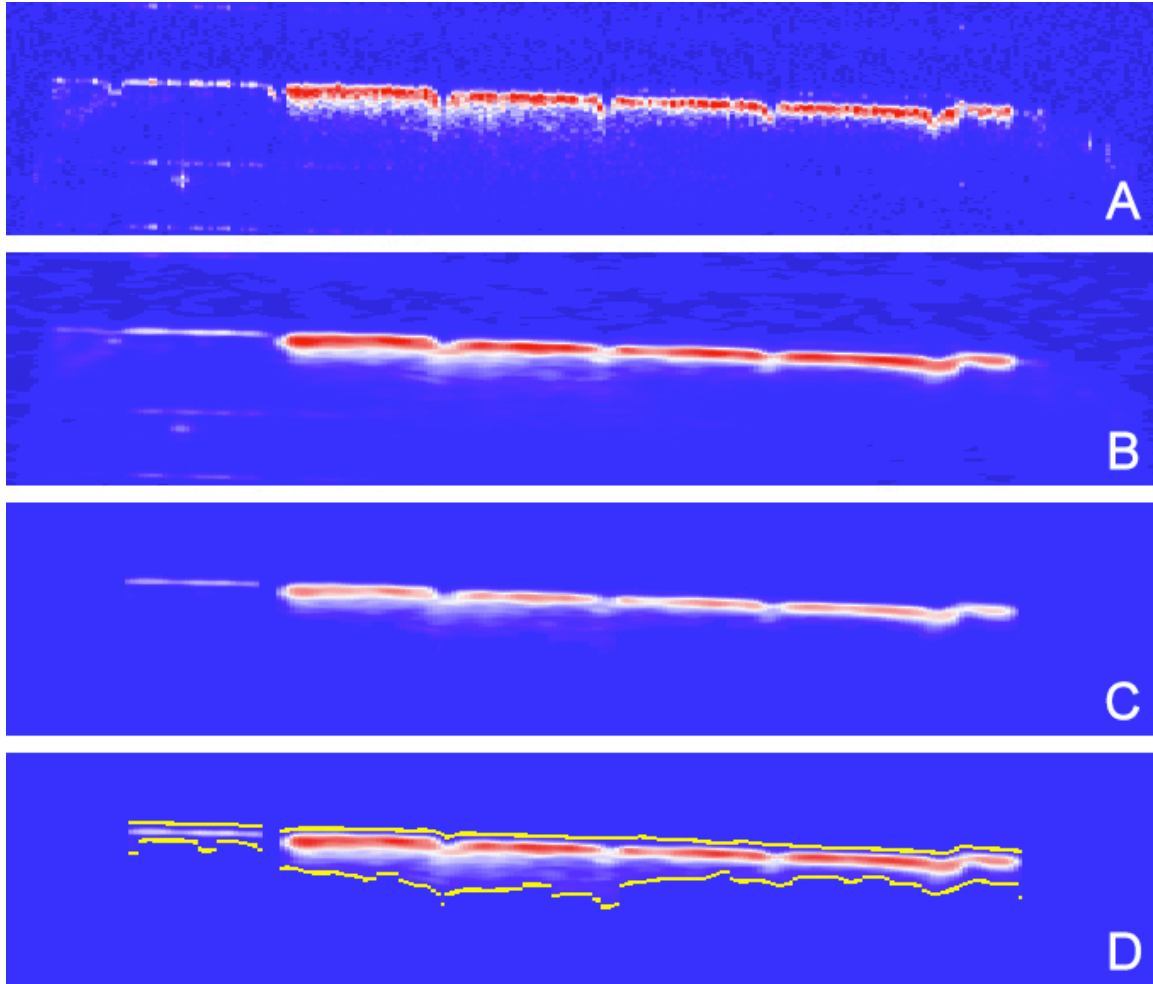
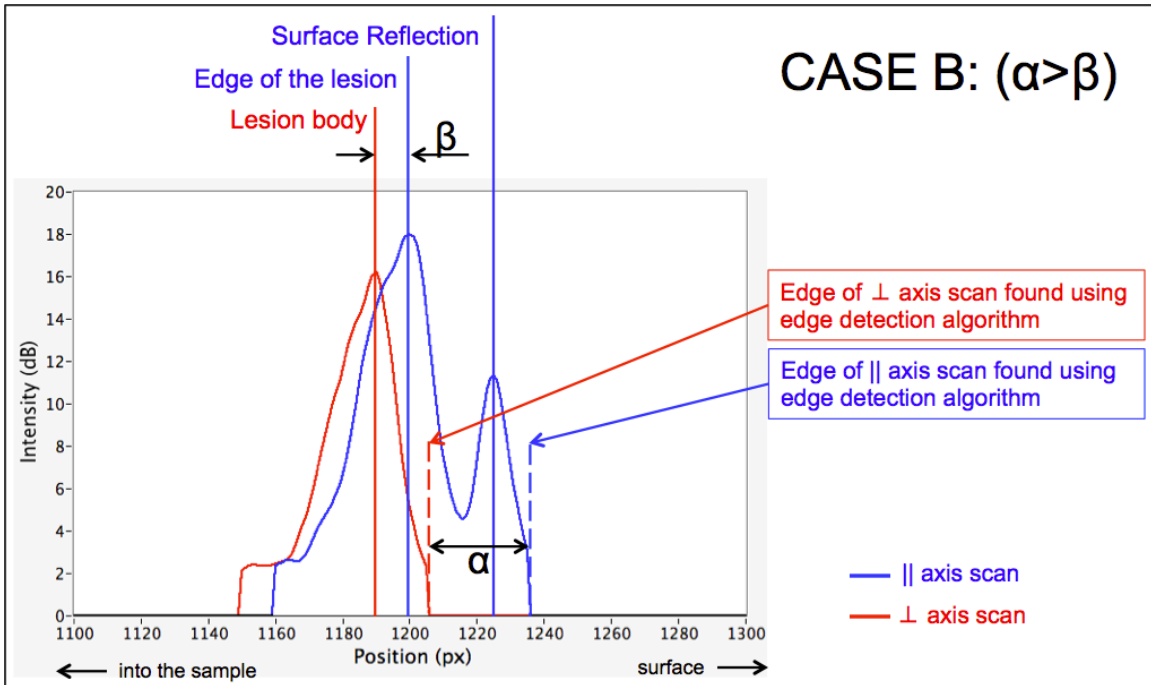
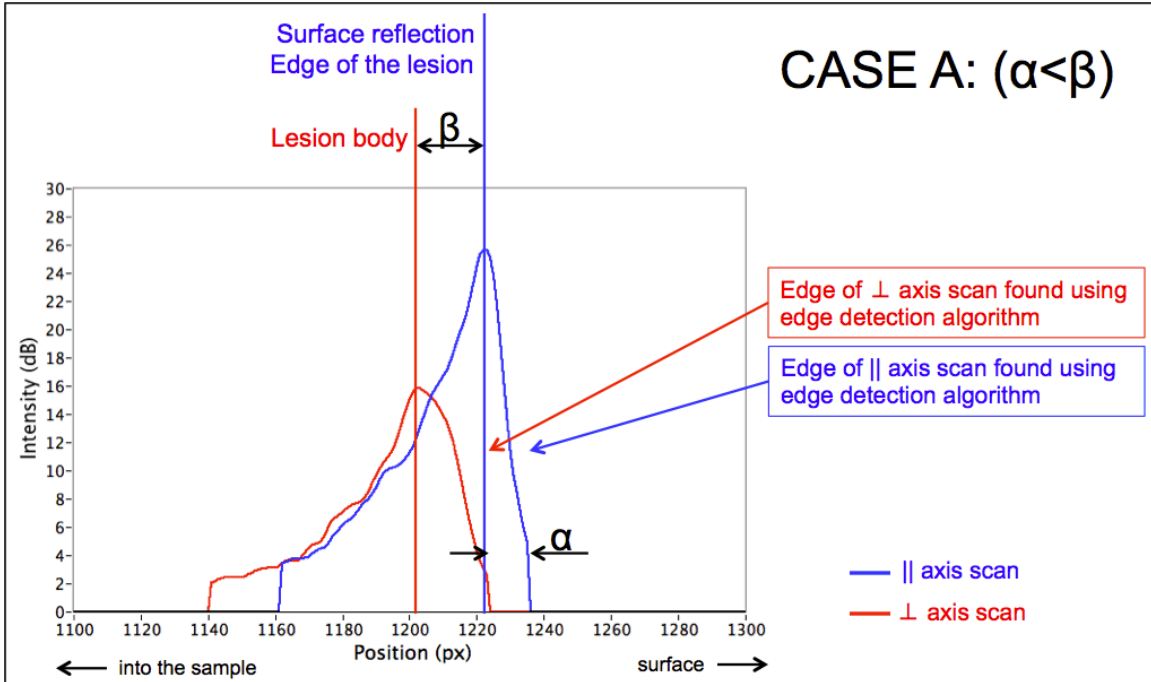


Figure 2.1 Diagrammatic representation of the image processing steps used in this experiment. Intensity scale is red-white-blue. (A) Original OCT b-scan; (B) Image adjusted with 5×5 median filter and 5×5 Gaussian convolution filter; (C) Image after background subtraction and thresholding; (D) Edges overlaid on (C).



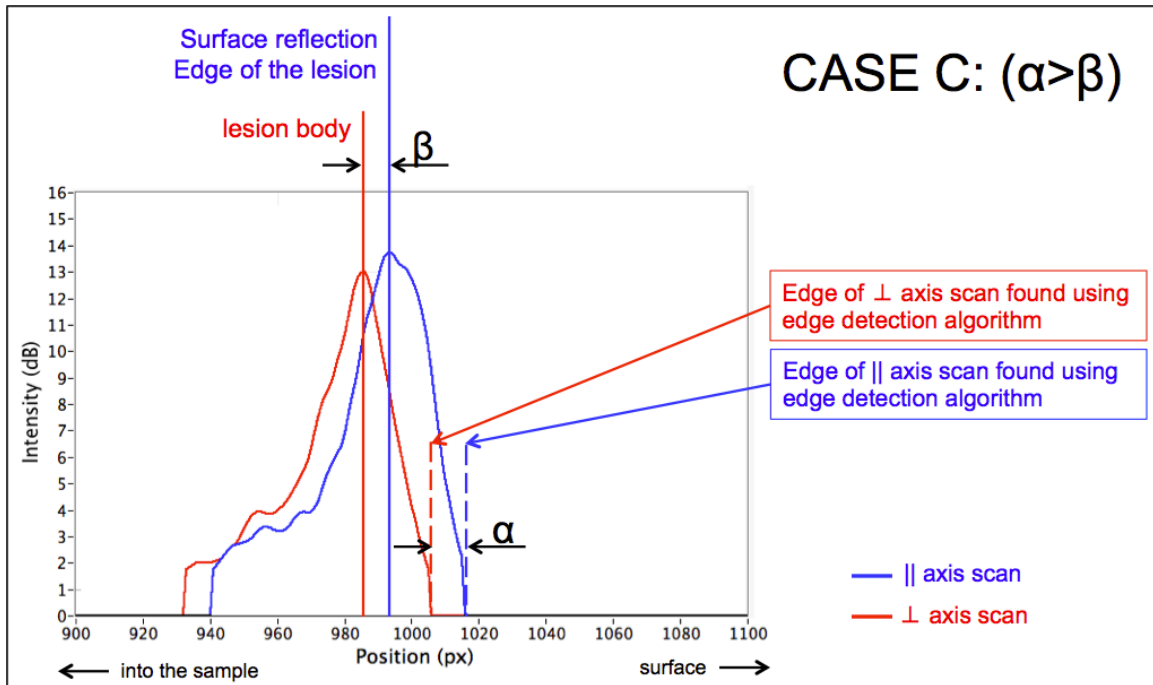


Figure 2.2 If α was greater than β , the transparent surface layer thickness was detected. CASE A ($\alpha < \beta$, single peak): no transparent surface layer was detected. CASE B ($\alpha > \beta$, double peak): the transparent surface layer was detected. CASE C ($\alpha > \beta$, single peak): the transparent surface layer was detected.

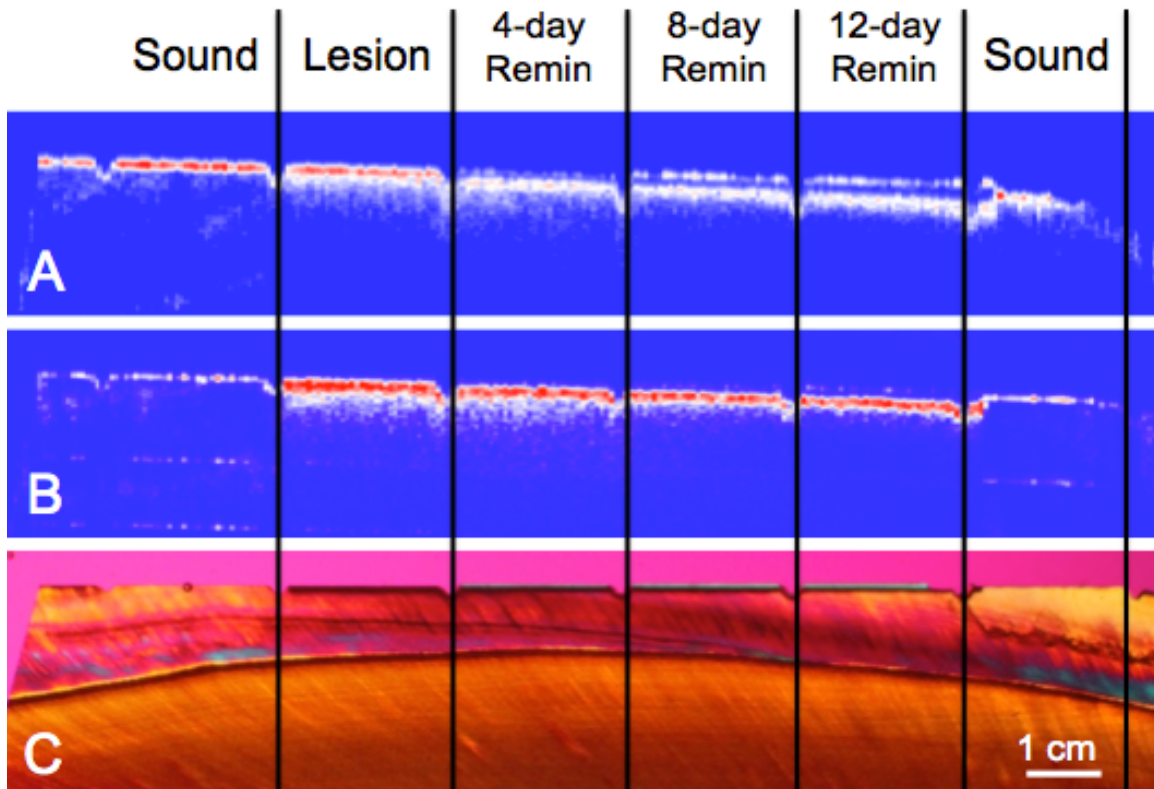


Figure 2.3 (A) (\parallel -axis) PS-OCT b-scan of a sample before sectioning. Intensity scale is in red-white-blue scheme. (B) The corresponding (\perp -axis) PS-OCT B-scan. (C) The corresponding PLM of 200- μ m-thick section in a similar orientation to the PS-OCT images.

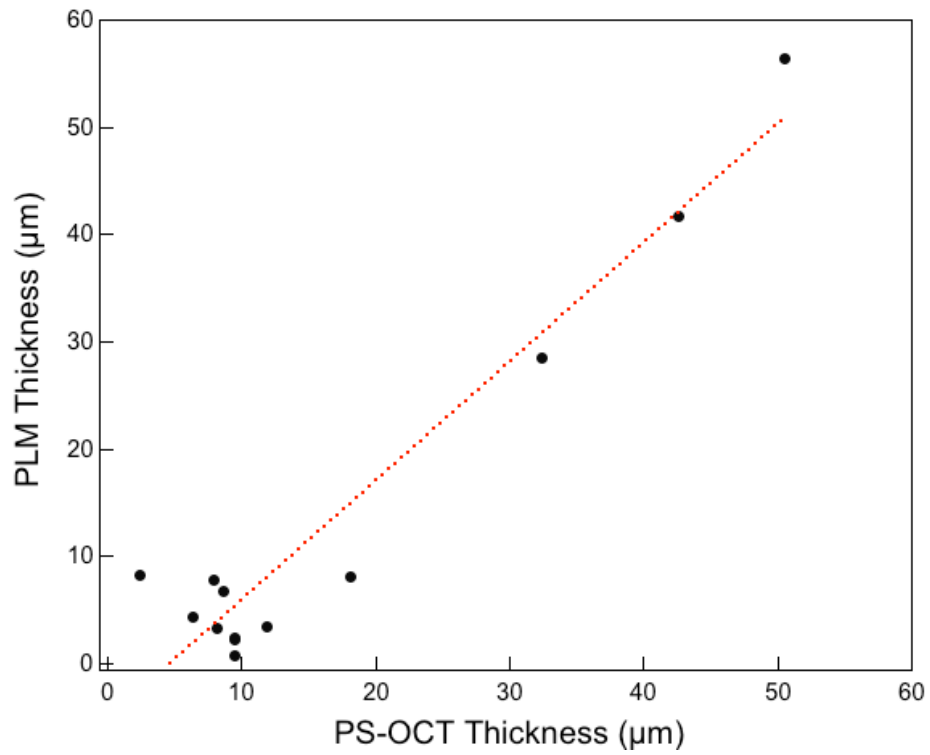


Figure 2.4 Plot of estimated transparent surface layer thickness from PS-OCT versus PLM images for the windows that manifested the transparent surface layer with PLM (n = 13) with corresponding regression line ($p < 0.0001$, $R^2 = 0.9213$).

2.6 REFERENCES

- Baumgartner, A., Dicht S., Hitzenberger, C. K., Sattmann, H., Robi, B., Moritz, A., Sperr, W. and Fercher, A. F. (2000). Polarization-sensitive optical coherence tomography of dental structures. *Caries Res.*, **34**: 59-69.
- Baumgartner, A., Hitzenberger, C. K., Dicht, S., Sattmann, H., Moritz, A., Sperr, W. and Fercher, A. F. (1998). Optical coherence tomography for dental structures. *Proc. SPIE Lasers in Dentistry IV*, San Jose, CA, **3248**: 130-136.
- Bush, J., Davis, P. and Marcus, M. A. (2000). All-fiber optic coherence domain interferometric techniques. *Proc. SPIE Fiber Optic Sensor Technology II*, San Jose, CA, **4204**: 71-80.
- Can, A. M., Darling, C. L. and Fried, D. (2008). High-resolution PS-OCT of enamel remineralization. *Proc. SPIE Lasers in Dentistry XIV*, San Jose, CA, **6843**: T1-7.
- Chan, K. H., Chan, A. C., Fried, W. A., Simon, J. C., Darling, C. L. and Fried, D. (2013). Use of 2D images of depth and integrated reflectivity to represent the severity of demineralization in cross-polarization optical coherence tomography. *J. Biophotonics*, **8**: 36-45.
- Darling, C. L., Huynh, G. D. and Fried, D. (2006). Light scattering properties of natural and artificially demineralized dental enamel at 1310 nm. *J. Biomed. Opt.*, **11**(3): 34023.
- Featherstone, J. D. B. (1996). Clinical implications: new strategies for caries prevention. *Proc. the 1st Annual Indiana Conference: Early Detection of dental caries*, Indianapolis, IN, 287-296.
- Featherstone, J. D. B. and Young, D. (1999). The need for new caries detection methods. *Proc. SPIE Lasers in Dentistry V*, San Jose, CA, **3593**: 134-140.
- Fejerskov, O. and Kidd, E., Eds. (2003). *Dental caries: the disease and its clinical management*. Oxford, Blackwell.
- Fried, D., Xie, J., Shafi, S., Featherstone, J. D. B., Breunig, T. M. and Le, C. Q. (2002). Early detection of dental caries and lesion progression with polarization sensitive optical coherence tomography. *J. Biomed. Opt.*, **7**(4): 618-627.
- Hume, W. R. (1996). Need for change in dental caries diagnosis. *Proc. the 1st Annual Indiana Conference: Early Detection of dental caries*, Indianapolis, IN, 1-10.
- Jones, R. S., Darling, C. L., Featherstone, J. D. B. and Fried, D. (2006). Imaging artificial caries on the occlusal surfaces with polarization-sensitive optical coherence tomography. *Caries Res.*, **40**(2): 81-89.

Jones, R. S., Darling, C. L., Featherstone, J. D. B. and Fried, D. (2006). Remineralization of in vitro dental caries assessed with polarization sensitive optical coherence tomography. *J. Biomed Opt.*, **11**(1): 014016.

Jones, R. S. and Fried, D. (2006). Remineralization of enamel caries can decrease optical reflectivity. *J. Dent. Res.*, **85**(9): 804-808.

Kang, H., Darling, C. L. and Fried, D. (2012). Nondestructive monitoring of the repair of enamel artificial lesions by an acidic remineralization model using polarization-sensitive optical coherence tomography. *Dent. Mater.*, **28**(5): 488-494.

Kidd, E. A. (1983). The histopathology of enamel caries in young and old permanent teeth. *Br. Dent. J.*, **155**(6): 196-198.

Le, M. H., Darling, C. L. and Fried, D. (2010). Automated analysis of lesion depth and integrated reflectivity in PS-OCT scans of tooth demineralization. *Lasers Surg. Med.*, **42**(1): 62-68.

Lee, C., Darling, C. L. and Fried, D. (2009). Polarization-sensitive optical coherence tomographic imaging of artificial demineralization on exposed surfaces of tooth roots. *Dent. Mater.*, **25**(6): 721-728.

Manesh, S. K., Darling, C. L. and Fried, D. (2009). Nondestructive assessment of dentin demineralization using polarization-sensitive optical coherence tomography after exposure to fluoride and laser irradiation. *J. Biomed. Mater. Res. B Appl. Biomater.*, **90**(2): 802-812.

Ngaotheppitak, P., Darling, C. L. and Fried, D. (2005). Measurement of the severity of natural smooth surface (interproximal) caries lesions with polarization sensitive optical coherence tomography. *Lasers Surg. Med.*, **37**(1): 78-88.

NIH (2001). Diagnosis and management of dental caries throughout life, *NIH Consensus Statement*, **18**: 1-24.

ten Cate, J. M. and van Amerongen, J. P. (1996). Caries diagnosis: conventional methods. *Proc. the 1st Annual Indiana Conference: Early Detection of dental caries*, Indianapolis, IN, 25-37.

CHAPTER III

AUTOMATED ASSESSMENT OF REMINERALIZATION OF ARTIFICIAL ENAMEL LESIONS WITH POLARIZATION-SENSITIVE OPTICAL COHERENCE TOMOGRAPHY

3.1 SUMMARY

Accurate measurement of the highly mineralized transparent surface layer that forms on caries lesions is important for diagnosis of the lesion activity because chemical intervention can slow or reverse the caries process via remineralization. Previous *in-vitro* and *in-vivo* studies have demonstrated that polarization-sensitive optical coherence tomography (PS-OCT) can nondestructively image the subsurface lesion structure and the highly mineralized transparent surface zone of caries lesions. The purpose of this work was to evaluate an approach to automatically process 3-dimensional PS-OCT images and to accurately assess the remineralization process in simulated enamel lesions. Artificial enamel lesions were prepared on twenty bovine enamel blocks using two models to produce varying degree of demineralization and remineralization. The thickness of the transparent surface layer and the integrated reflectivity of the subsurface lesion were measured using PS-OCT. The automated transparent surface layer detection algorithm was able to successfully detect the transparent surface layers with high sensitivity (= 0.92) and high specificity (= 0.97). The estimated thickness of the transparent surface layer showed a strong correlation with polarized light microscopy (PLM) measurements of all regions ($R^2 = 0.90$). The integrated reflectivity, ΔR , and the integrated mineral loss, ΔZ , showed a moderate correlation ($R^2 = 0.32$). This chapter demonstrates that PS-OCT can automatically measure the changes in artificial enamel lesion structure and severity upon exposure to remineralization solutions.

3.2 INTRODUCTION

The caries process is potentially preventable and curable (NIH 2001). It is widely accepted that fluoride reduces the incidence of dental caries and slows or reverses the progression of existing lesions (Fejerskov and Kidd 2003). In addition to the fluoride therapy, other preventive measures such as anti-bacterial therapy, dietary changes or low intensity laser irradiation can be used as non-surgical means to arrest or reverse caries activity (Featherstone 1996, NIH 2001). Clinicians must be able to accurately diagnose lesion activity to establish the need for preventive treatment. Therefore, one cannot overstate the importance of accurate diagnosis of the caries activity in its early stage of development at which point non-invasive preventive measures can be taken to halt further decay.

Early caries lesions in enamel have a chalky white appearance with an intact surface layer (Fejerskov and Kidd 2003). The intact surface is of paramount importance because therapeutic intervention can arrest or reverse the process by remineralization (Featherstone 2000). Calcium and phosphate ions are lost from the tooth enamel during the demineralization process and the surface layer may erode with more severe acid challenge or mechanical abrasion and form a cavity (ten Cate and Featherstone 1991). During remineralization, there is growth of existing partially demineralized crystals as well as growth of new crystals within the lesion body due to the increased influx of calcium and phosphate ions (Featherstone et al. 1990). The remnant crystal structure acts as a nucleation center for crystal growth. Fluoride plays a key role in the process of remineralization by enhancing the crystal growth and inhibiting future demineralization at the crystal surface. Remineralization therapy via fluoride produces fluorapatite

crystals that are much more resistant to acid challenge than the original hydroxyapatite of enamel and dentin. With a thick enough fluorapatite layer, diffusion of calcium and phosphate ions at the lesion body, can be dramatically reduced (ten Cate and Arends 1977, Kidd 1983, ten Cate and Featherstone 1991). This leads to the arrest of lesion progression and no further intervention is necessary.

The surface layer of a lesion is important for diagnosis of the current “state of the lesion”, i.e., whether or not the caries lesion is active and expanding or whether the lesion has been arrested and is undergoing remineralization. Current methods for lesion assessment are composed of a combination of visual and tactile exams, which are prone to subjective bias, interference from staining, limitation to exposed surfaces and potential permanent damage to dental tissue from sharp instruments (NIH 2001, Ekstrand et al. 2009). In addition, the remineralized caries lesion still retains the white coloration due to the subsurface demineralization, which may lead to an inconclusive diagnosis of caries activity (Ekstrand et al. 2009). The gold standards for lesion assessment such as transverse microradiography (TMR) and polarized light microscopy (PLM) require destruction of the tooth, making both methods unsuitable for use *in-vivo*. New technologies are needed to determine whether caries lesions have been partially remineralized and have become arrested. Previous studies have demonstrated that PS-OCT is uniquely capable of this task since it provides a measurement of the reflectivity from each layer of the lesion and is able to show the formation of a zone of increased mineral density and reduced light scattering due to remineralization (Jones et al. 2006, Manesh et al. 2009, Kang et al. 2012).

Polarization sensitivity is particularly valuable for resolving the structure of early caries lesions. PS-OCT images are typically processed in the form of phase and intensity images, and such images best show variations in the birefringence of the tissues (Baumgartner et al. 1998, Baumgartner et al. 2000). Caries lesions strongly scatter incident polarized light and the image in the orthogonal polarization axis to that of the incident polarization can provide improved lesion contrast. There are two mechanisms in which the intensity can arise in the cross-polarization axis. The native birefringence of the tooth enamel can rotate the phase angle of the incident light beam between the two cross-polarization axes as the light propagates through the enamel without changing the degree of polarization. The other mechanism is the scattering of incident light in which the degree of polarization is reduced. It is this mechanism that is exploited to measure the severity of demineralization. Strong scattering of the incident linearly polarized light scrambles the polarization and leads to equal distribution of the intensity in both orthogonal polarization axes. Demineralization of the enamel due to dental decay causes an increase in the scattering coefficient by a 1-2 orders of magnitude (Darling et al. 2006). This in turn causes a large rise in reflectivity in the cross-polarization axis. This approach also has the advantage of reducing the intensity of the strong surface reflection from the tooth allowing measurement of the lesion surface zone. A conventional OCT system is susceptible to strong Fresnel surface reflectance that can mask or resemble increased reflectivity from the lesion itself. Varying the angle of incidence and topical application of high index agents may be employed to mitigate the effect of the strong surface reflection in conventional OCT systems (Jones and Fried 2005, Nam et al. 2011). The reflectivity in the cross-

polarization OCT (CP-OCT) images can be directly integrated to quantify the lesion severity, regardless of the tooth topography. By using this approach, the difficult task of deconvolving the strong surface reflection from the lesion surface can be circumvented. We have demonstrated in several studies that the lesion severity can be represented by the integrated reflectivity with depth in the CP-OCT image (Fried et al. 2002, Ngaotheppitak et al. 2005, Jones et al. 2006, Jones et al. 2006, Chong et al. 2007, Lee et al. 2009, Manesh et al. 2009). The integrated reflectivity, ΔR , obtained from CP-OCT is a measurement analogous to the integrated mineral loss, ΔZ , obtained from TMR (Arends et al. 1997). In contrast to most PS-OCT studies, which combine the images in both channels to generate images of phase and intensity, we utilize only the intensity in the cross polarization image to calculate ΔR (Everett et al. 1999, Baumgartner et al. 2000).

In the approach presented in ref. (Lee et al. 2014), both polarization axes are required to determine the thickness of the surface zone. An accurate assessment of caries activity and severity is paramount for the clinical diagnosis of caries. Therefore, quantitative measurements of the transparent surface layer thickness and ΔR with PS-OCT are extremely valuable. In previous PS-OCT studies, we developed approaches to automatically quantify the severity of caries lesions and the depth of demineralized enamel for the rapid image processing of large 3D data sets (Kang et al. 2012). In this chapter, we evaluate an approach to automatically process the OCT images to accurately detect and measure the thickness of the transparent surface layer in simulated enamel lesions that have undergone remineralization.

3.3 MATERIALS AND METHODS

3.3.1 Sample Preparation

Enamel blocks (n = 20), approximately 8 – 12 mm in length with a width of 2 mm and a thickness of 3 mm were prepared from extracted bovine incisors acquired from a slaughterhouse. Each enamel and bovine sample was partitioned into five regions or windows (1 sound and 4 lesion regions) by etching small incisions 1.8 mm apart across each of the enamel blocks using a laser. Incisions were etched using a transverse excited atmospheric pressure (TEA) CO₂ laser, an Impact 2500, GSI Lumonics (Rugby, UK), operating at 9.3 μm with a pulse duration of 15 μs, a pulse repetition rate of 200 Hz and a fluence of 20 J/cm². A thin layer of acid-resistant varnish in the form of nail polish, Revlon (New York, NY) was applied to protect the sound control area on each end of the block before exposure to the demineralization solution.

Artificial enamel lesions were prepared using two different methods in order to produce varying degree of demineralization and remineralization. The neutral pH remineralization model utilizes an undersaturated calcifying solution that has been shown to remineralize enamel more completely than a supersaturated calcifying solution (Silverstone et al. 1981). The undersaturated solution maintains the porosity of the outer enamel lesion surface to promote the remineralization of the inner portions of the lesion. One group of enamel samples (n = 10) were immersed in a demineralization solution maintained at 37°C for 24 hours at pH 4.9 composed of a 40 mL aliquot of 2.0 mmol/L calcium, 2.0 mmol/L phosphate and 0.075 mol/L acetate. These samples were placed into the neutral pH remineralization solution composed of 1.5 mmol/L calcium,

0.9 mmol/L phosphate, 150 mmol/L KCl, 2 ppm F⁻, and 20 mmol/L HEPES buffer maintained at pH 7.0 and 37°C (ten Cate and Arends 1977).

It has been also shown that the supersaturated acidic calcifying solution can enhance the rate and extent of subsurface remineralization (Yamazaki and Margolis 2008). It has been hypothesized that the supersaturated acidic calcifying solution maintains the mineral ion diffusion channels within the outer enamel lesion due to the acidity of the solution. Another group of enamel samples (n = 10) were immersed in a demineralization solution maintained at 37°C for 8 hours at pH 4.6 composed of a 40 mL aliquot of 18 mmol/L calcium, 8 mmol/L phosphate, and 0.1 mol/L lactic acid. These samples were placed into acidic remineralization solution at pH 4.8 composed of a 40 mL aliquot of 4.1 mmol/L calcium, 15 mmol/L phosphate, 50 mmol/L lactic acid and 20 ppm F⁻ (Yamazaki and Margolis 2008).

Acid-resistant varnish was applied to the windows for 0, 4, 8 and 12 day periods of remineralization. After the fourth period, the samples were removed from the remineralization solution, and the acid resistant varnish was removed by immersion in acetone in an ultrasonic bath for 15 minutes. Each sample was then stored in 0.1% thymol solution to prevent fungal and bacterial growth.

3.3.2 PS-OCT System

The system used in this work has been described previously (Fried et al. 2002). An all fiber-based Optical Coherence Domain Reflectometry (OCDR) system with polarization maintaining (PM) optical fiber, high speed piezoelectric fiber-stretchers and two balanced InGaAs receivers PDR-13 that was designed and fabricated by Optiphase,

Inc., Van Nuys, CA was used to acquire the images. This two-channel system was integrated with a broadband superluminescent diode (SLD) DL-CS3159A, Denselight (Jessup, MD) and a high-speed XY-scanning system (ESP 300 controller & 850G-HS stages, National Instruments, Austin, TX) for in-vitro optical tomography. This system is based on a polarization-sensitive Michelson interferometer (Bush et al. 2000). The high power (15 mW) polarized SLD source operated at a center wavelength of 1317 nm with a spectral bandwidth full-width-half-maximum (FWHM) of 84 nm to provide an axial resolution of 9 μm in air and 6 μm in enamel (refractive index = 1.6). This light was aligned with the slow axis of the PM-fiber of the source arm of the interferometer. The sample arm was coupled to an anti-reflectance (AR) coated fiber-collimator to produce a 6 mm in diameter, collimated beam. That beam was focused onto the sample surface using a 20 mm focal length AR coated plano-convex lens. This configuration provided a lateral resolution of approximately 20 μm with a dynamic range of 48 dB. Both orthogonal polarization states of the light scattered from the tissue were coupled into the slow and fast axes of the pm-fiber of the sample arm. A quarter wave plate set at 22.5° to horizontal in the reference arm rotated the polarization of the light by 45° upon reflection. After being reflected from the reference mirror and the sample, the reference beams were recombined by the pm fiber-coupler. A polarizing cube splits the recombined beam into its horizontal and vertical polarization components or “slow” and “fast” axis components, which were then coupled by single mode fiber optics into two detectors. The light from the reference arm was polarized at 45° and therefore split evenly between the two detectors. Readings of the electronically demodulated signal from each receiver channel represent the intensity for each orthogonal polarization of

the backscattered light. Neutral density filters are added to the reference arm to reduce the intensity noise for shot limited detection. The all-fiber OCDR system is described in reference (Bush et al. 2000).

The PS-OCT system was completely controlled using LabView™ software (National Instruments, Austin, TX). Each B-scan consisted of 300 A-scans spaced 50 μm apart. The A-scan sweep rate was 100 Hz and each A-scan was averaged 10 times. The total number of data points in each A-scan was 2000 over a scan range of approximately 7 mm in air.

3.3.3 Image Processing

Images obtained from the PS-OCT were processed using a dedicated program constructed with Labview™ software. The automated image processing method is based on a previous study (Kang et al. 2010). There is a phase shift in PM-fiber between the two axes and the axial position calibration was performed only once prior to the experiment. A gold mirror was scanned at 100 Hz scan sweep rate and each A-scan was averaged 100 times. One hundred A-scans were acquired at 50 μm intervals over the entire scan range to determine the required axial position adjustments and the axial position of the cross-polarization scan images was adjusted to match the co-polarization scan images.

Background subtraction was carried out by subtracting the mean reflectivity of 200 data points measured in air acquired from the top 4 pixels of the 50 unprocessed A-scans outside the sample area for each B-scan. Those 200 data points provided consistent information about the system noise and manifested a standard deviation

smaller than 0.01 dB. Tomographic images of the sample were reconstructed from B-scans. The images were convolved with a 5x5x5 anisotropic diffusion Gaussian smoothing filter with σ (= 4 μm) based on the $\mu\text{m}/\text{pixel}$ ratio of sound enamel in each axis in order to reduce speckle noise. A 5x5 rotating kernel transformation (RKT) technique was applied in x-z and y-z spaces to emphasize thin edges while further suppressing speckle noise (Lee and Rhodes 1990). We determined that the 5x5x5 anisotropic diffusion Gaussian smoothing filter and the 5x5 RKT filter yielded the highest contrast of the transparent surface layer.

3.3.4 Transparent Surface Layer Detection and Measurement

Edge detection was applied to each A-scan using the zero-crossing first-order derivative. The position of the maximum peak of each A-scan was designated as the first peak and the respective edges of the first peak were found by locating the pixels for which the magnitude of the gradient exceeded a certain minimum for at least 4 consecutive pixels. If those edges were found, a second peak was located by searching for the maximum peak intensity outside of the initial edges. The intensity values of the two peaks were required to be greater than 3 standard deviations of the noise. The ratio of intensity values of the two peaks was required to be above a threshold of 0.1 and the ratio of the intensity values of the edge and the second peak was required to be less than a threshold of 0.75. If two peaks were found, the algorithm assumed the upper positioned peak to be the surface reflection and the lower positioned peak to be in lesion body. By carefully adjusting the threshold values, it was possible to detect only the desired peaks and ignore peaks that were too small, too wide, or too narrow, thus reducing false-

positives (Lee et al. 2014). These threshold values were specific to this PS-OCT system and the same threshold values were applied to all the samples.

The position of the strong surface reflection in the co-polarization axis and the strong scattering of polarized light from the underlying lesion body in the cross-polarization axis are used as previously described in the three diagrams of Fig. 2 in ref. (Lee et al. 2014). Binary images were generated to indicate either the presence or absence of the transparent surface layer and a 5x5 morphological closing operation with a 50% threshold was subsequently applied to the binary images in order to reduce false-negatives. Pixels were converted to microns in enamel using a refractive index correction of 1.6 to yield the final transparent surface layer thickness. The thickness of the transparent surface layer was estimated by averaging 25 A-scans from a 5x5 region of interest. A 5x5 median filter was applied to the final 2D projection image of the transparent surface layer thickness for improved visualization.

3.3.5 Lesion Depth Measurement

The previously developed algorithm to calculate the lesion depth utilized a threshold of $1/e^2$ of the peak maximum (Kang et al. 2010). We compared that approach with an algorithm that utilizes the full-width-half-maximum (FWHM). Images acquired in a previously study (n = 34) were analyzed (Chan et al. 2013) using the two methods. An edge locator was used to make two passes along each A-scan of the processed CP-OCT images to locate the respective positions at which the intensity has decreased to the threshold calculated with either $1/e^2$ or half of the lesion peak maximum. A linear relationship was established between the lesion depth using PS-OCT and the

histological lesion depths measured using polarized light microscopy (PLM) [32]. Based on this relationship, the goodness of fit, R^2 , was compared and a linear correction was applied to the lesion depth calculated from CP-OCT.

3.3.6 Integrated Reflectivity Measurement (ΔR)

Previous studies have shown that the integrated reflectivity, ΔR , over the estimated lesion depth positively correlates with the integrated mineral loss (volume percent mineral loss $\times \mu\text{m}$), ΔZ (Ngaotheppitak et al. 2005, Jones et al. 2006). A region of interest (ROI) was specified for the sound region from each sample in order to discriminate between demineralized and sound enamel. ΔR was calculated from the selected ROI and it was compared to the ΔR of the lesions in order to reduce false-positives in lesion detection. Remineralized lesions do not typically yield a complete reversal of demineralization and the original lesion body is partially retained under the transparent surface layer. (ten Cate and Featherstone 1991). ΔR was calculated by integrating from the base of the transparent layer through the entire estimated lesion body in the CP-OCT images. This had the added advantage of removing the contribution of the high specular reflection at the surface of the transparent layer, which was large enough to be present even in the CP-OCT images. A 5x5 median filter was applied to the final 2D projection image of ΔR for improved visualization.

3.3.7 Polarized Light Microscopy (PLM) and Transverse Microradiography (TMR)

After sample imaging was completed, approximately 200 μm thick serial sections were cut using an Isomet 5000 saw (Buehler, IL), for polarized light microscopy (PLM) and

transverse microradiography (TMR). PLM was carried out using a Meiji Techno Model RZT microscope (Meiji Techno Co., LTD, Saitama, Japan) with an integrated digital camera, Canon EOS Digital Rebel XT (Canon Inc., Tokyo, Japan). The sample sections were imbibed in water and examined in the brightfield mode with crossed polarizers and a red I plate with 500 nm retardation. PLM images were acquired at 350x magnification and had a resolution of 3264 x 2448 pixels.

A custom built digital microradiography (TMR) system was used to measure the volume percent mineral content in the areas of demineralization on the tooth sections (Darling et al. 2009). High- resolution microradiographs were taken using Cu K α radiation from a Philips 3100 X-ray generator and a Photonics Science FDI X-ray digital imager, Microphotonics, (Allentown, PA). The X-ray digital imager consists of a 1392 \times 1040 pixel interline CCD directly bonded to a coherent micro fiber-optic coupler that transfers the light from an optimized gadolinium oxysulfide scintillator to the CCD sensor. The pixel resolution is 2.1 μ m, and the images can be acquired in real time at a frame rate of 10 fps. A high-speed motion control system with Newport (Irvine, CA) UTM150 and 850G stages and an ESP 300 controller coupled to a video microscopy and laser targeting system was used for precise positioning of the tooth sample in the field of view of the imaging system. Sections with uneven thickness or fractured surface were excluded from statistical analysis.

3.3.8 Statistical Analysis

Sample groups were compared using repeated measures analysis of variance (ANOVA) with a Tukey–Kramer post hoc multiple comparison test. Linear regression with

Pearson's correlation was used to examine the relationship between data acquired from PS-OCT, PLM and TMR measurements, including sound, demineralization and remineralization areas. All statistical analyses were performed with 95% confidence with Prism™ (GraphPad software, San Diego, CA).

3.4 RESULTS

Figure 3.1 and 3.2 show PLM images, CP-OCT B-scans and TMR images of the samples prepared with the acidic pH remineralization model (**Fig. 3.1**) and the neutral pH remineralization model (**Fig. 3.2**). A transparent surface layer due to remineralization is clearly visible in both models with PLM, TMR and OCT. The transparent surface layer that was automatically detected with the software is highlighted in yellow in the OCT images as shown in **Figs. 3.1C and 3.2C**. The two remineralization models produce markedly different structures. The neutral pH remineralization model produced new mineral predominantly along the surface of the enamel lesion as shown in the TMR image (**Fig. 3.2D**). There was minimal mineralization of the body of the lesion with this approach (Liu et al. 2011). However, the acidic pH remineralization model produced mineralization in the lesion body as shown in **Fig. 3.1D**. Although mineralization was incomplete in this region compared to the sound enamel structure, it was much higher than the corresponding region produced with the neutral pH remineralization model. Some samples exposed to the acidic pH remineralization model exhibited demineralization of the surface of the transparent surface layer, which goes through constant demineralization at low pH with continued nucleation of fluorapatite (Yamazaki and Margolis 2008). These models represent different variations of demineralization and

remineralization that occur in the oral cavity.

The automated transparent surface layer detection algorithm was able to successfully detect the transparent surface layers. The smallest surface layer thickness detectable was 4 pixels (10 μm). Detection of the transparent surface layer with PLM and TMR is limited due to “edge-effects” which varied from 0 μm to 35 μm for the 200 μm thick sections. Edge-effects are caused by the uneven sample surface, which is often not perfectly perpendicular to the serial cut sections. The edge-effects in PLM can be seen as a blurry shadow at the edge of the sample and at the interface of the two materials such as the dentino-enamel junction, and the edge-effects in TMR result in underestimation of the volume percent mineral leading to inaccurate integrated mineral loss. It was possible to detect transparent surface layers smaller than 10 μm with PLM for some samples with minimal edge-effects (Lee et al. 2009). OCT does not suffer from edge-effects since it does not require serial cut sections. The algorithm detected the lesions with transparent surface layers with high sensitivity (0.92) and high specificity (0.97) compared with PLM, and the algorithm detected all the lesions with transparent surface layers thicker than 10 μm . The total number of windows was 80 from 20 samples with 44 true positives, 1 false-positive, 31 true-negatives and 4 false-positives. The thickness of the transparent surface layer estimated with PS-OCT showed a strong correlation with PLM measurements (Pearson’s correlation, $p < 0.0001$, $R^2 = 0.90$) as shown in **Fig. 3.3**.

The intensity of the lesion body is reduced due to attenuation and dispersion from the transparent surface layer and use of a threshold of $1/e^2$ of the peak maximum of the lesion body in the cross-polarization axis scan overestimates the lesion body

depth. Although the accurate estimation of the depth of the lesion body is confounded by dispersion from the thick transparent surface layer, approximation of the depth of the lesion body is still necessary in order to calculate the integrated reflectivity. Thus, the previously proposed algorithm for estimating lesion depth employing $1/e^2$ width of the peak maximum was compared to the one employing FWHM. The half value of the peak maximum provided a threshold that was well above 3 standard deviations of the noise and the variable intensity caused by birefringence banding in the enamel for most samples (Baumgartner et al. 1998). Enamel is composed of highly oriented hydroxyapatite crystals and changes in crystal orientation cause changes in birefringence, which show up as banding artifacts in PS-OCT images. Comparison with the PLM measurements indicated that the method that employed FWHM (Pearson's correlation, $p < 0.0001$, $R^2 = 0.91$) yielded higher correlation compared to the method that employed the $1/e^2$ width of the peak maximum (Pearson's correlation, $p < 0.0001$, $R^2 = 0.76$). Based on this relationship, linear regression was employed to correct the OCT lesion depth (Corrected lesion depth = $2.694 \times \text{OCT pixel depth} - 27.5$). The corrected lesion depth and the depth of the lesion body underlying the transparent surface layer were estimated with PS-OCT by using FWHM as a threshold. **Figure 3.4** shows strong correlation (Pearson's correlation, $p < 0.0001$, $R^2 = 0.58$) of the corrected lesion depth measured with PS-OCT and the lesion depth measured with PLM for the windows that did not exhibit the transparent surface layer (true-negatives). However, when the estimated depth measurements of the lesion body of all windows that exhibited the transparent surface layer (true-positives) with PS-OCT were compared with the depth measurements with PLM, there was a significant reduction in the

correlation (Pearson's correlation, $p = 0.0258$, $R^2 = 0.11$) as well as an overestimation of the depth of the lesion body due to dispersion from the varying thickness of the transparent surface layer.

The integrated reflectivity, ΔR , over the estimated depth of the lesion body and the integrated mineral loss, ΔZ , of the windows with uniform thickness ($n = 52$) exhibited a moderate correlation (Pearson's correlation, $p < 0.0001$, $R^2 = 0.32$) as shown in **Fig. 3.5**. TMR is also prone to edge-effects due to the 200 μm section thickness and most of the lesions are shallow, less than 100 μm . In addition, the mineral loss in the area was small $\sim 5\%$, which is difficult to resolve with TMR. The lesion severity and the thickness of transparent surface layer measurements for PS-OCT, PLM and TMR are tabulated in **Table 3.1** for both models.

The transparent surface layer thickness and ΔR , lesion severity, can be displayed as 2D projection images in order to aid in visualization of the lesion. Surface projection images of a sample prepared via the acidic pH remineralization model are shown in **Fig. 3.6**. Selection of the sound region as a control allowed better discrimination of the sound and demineralized enamel.

3.5 DISCUSSION

It is challenging to simulate the complex processes of demineralization and remineralization that occur in the oral cavity with a single *in-vitro* model (White 1995). The use of two different demineralization and remineralization models in this chapter produced transparent surface layers that varied markedly. It is believed that the remineralization process *in-vivo* is not simple superficial mineral deposition that leads to

lesion arrestment. It is suspected that it is mostly due to a repair of the existing enamel crystal remnants (Silverstone et al. 1981). In addition, there is likely a constant intra-oral mechanical force that prevents cariogenic plaque accumulation and superficial mineral deposition (Thylstrup et al. 1994). It is highly unlikely that the superficial mineral deposition that was shown with the neutral pH remineralization model (**Fig. 3.2**) replicates the remineralization process *in-vivo*. The acidic pH remineralization model showed increased mineral deposition in the lesion body (**Fig. 3.1**), which appears to better emulate *in-vivo* remineralization. It is encouraging that the algorithm was able to detect both transparent surface layer types with varying mineral profiles.

Although it was computationally intensive, the incorporation of 3D image-processing approaches such as the RKT and the anisotropic diffusion Gaussian convolution filter dramatically improved image quality compared to processing 2D B-scans individually as used in our previous OCT studies. The anisotropic diffusion Gaussian convolution filter accurately accounted for the difference between axial and transverse resolution in 3D versus 2D and the RKT filter was able to highlight the continuity of edges in 3D rather than in 2D. This enabled more accurate measurement of the transparent surface layer. In addition, using FWHM as opposed to $1/e^2$ width for the peak maximum resulted in higher correlation with histology as well as better differentiation from artifacts caused by the optical system and the enamel birefringence. Dispersion from the transparent surface layer may have caused the depth of the lesion body to be over-estimated as shown in **Fig. 3.4**. The total amount of dispersion increases linearly with the length of a dispersive medium (Fercher et al. 2001). The dispersion mismatch causes broadening of the coherence function in the sample arm by

unbalanced dispersion and reduction in peak intensity. Thus, the lesion body depth may be dependent on the thickness of the transparent surface layer. ΔR is not expected to change significantly due to peak broadening since the overall reflectivity should be similar. Dispersion compensation for such a highly variable composite mineral layer via correlation or deconvolution techniques is extremely complex and is beyond the scope of this dissertation (Fercher et al. 2001). Nonetheless, the lesion severity, which is of greater interest, can still be accurately determined by calculating ΔR over the FWHM provided by the system.

3.6 CONCLUSION

This chapter demonstrates that PS-OCT can be used to nondestructively measure the changes in the artificial enamel lesion structure and severity upon exposure to remineralization solutions using these two different models. The automated detection and measurement of the transparent surface layer process with high sensitivity and specificity can provide extremely useful information about lesion activity to aid clinicians in the diagnosis of caries lesions. There is no accepted gold standard that can be used to differentiate between an active and an arrested lesion. The conventional lesion activity assessment methods currently available such as visual and tactile methods are not reliable and reproducible (NIH 2001). The remineralized fluorapatite rich surface layer above the lesion body has enhanced resistance to acid dissolution (ten Cate and Arends 1977, Kidd 1983, ten Cate and Featherstone 1991) and the detection of this layer with PS-OCT is of great clinical significance.

3.7 FIGURES AND FIGURE LEGENDS

Table 3.1 Mean \pm S.D. of PS-OCT, PLM and TMR measurements for the four periods of exposure to the remineralization solution. Groups with the same letter are statistically similar, $P > 0.05$ in each row.

	0-Day	4-Day	8-Day	12-Day
Acidic pH Remineralization Model (n = 10)				
Transparent Layer Thickness (PS-OCT, μm)	9.2 \pm 13.7 a	42.8 \pm 12.2 b	44.4 \pm 9.7 b	48.8 \pm 10.5 b
Transparent Layer Thickness (PLM, μm)	10.6 \pm 15.9 a	40.5 \pm 11.5 bc	45.1 \pm 10.2 bd	50.5 \pm 8.7 cd
Integrated Reflectivity, ΔR (dB \times μm)	483 \pm 172 a	402 \pm 118 ab	346 \pm 148 bc	299 \pm 119 c
Integrated Mineral Loss ^{**} , ΔZ (vol% \times μm)	800 \pm 141 a	683 \pm 180 ab	612 \pm 235 ab	469 \pm 201 b
Neutral pH Remineralization Model (n=10)[*]				
Transparent Layer Thickness (PS-OCT, μm)	0 a	8.2 \pm 10.6 a	9.0 \pm 16.1 a	11.3 \pm 18.0 a
Transparent Layer Thickness (PLM, μm)	0 a	5.8 \pm 9.2 a	8.5 \pm 13.3 a	10.3 \pm 15.3 a
Integrated Reflectivity, ΔR (dB \times μm)	805 \pm 142 a	826 \pm 137 ab	767 \pm 126 b	694 \pm 134 c
Integrated Mineral Loss ^{***} , ΔZ (vol% \times μm)	1017 \pm 250 a	911 \pm 265 ab	772 \pm 168 b	615 \pm 132 b

^{*}In half of the samples, the transparent surface layer was not visible using PLM.

^{**}n = 5 and ^{***}n = 8, samples with uneven thickness or fractured surface were excluded from TMR analysis.

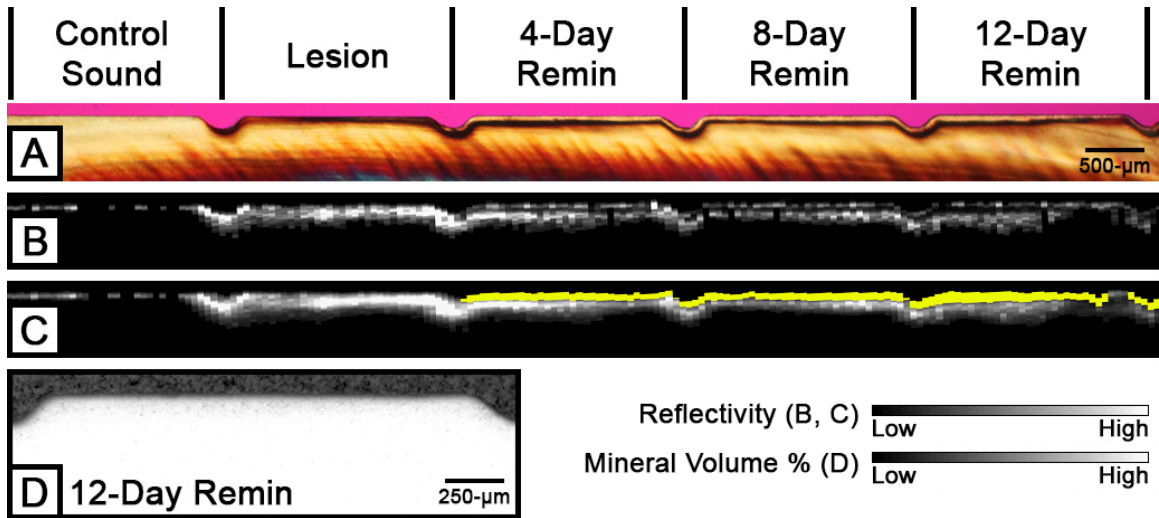


Figure 3.1 PLM, CP-OCT and TMR images of the samples from the acidic pH remineralization model for the four time periods of exposure to the remineralization solution. PLM (A) and CP-OCT B-scans (unprocessed B; processed C) images show decreased depth of the lesion body as well as an increase in transparent surface layer thickness over the periods of exposure to remineralization solution. The transparent surface layer is highlighted in yellow in PS-OCT image (C). TMR image (D) shows increased mineralization of the lesion after exposure to remineralization solution for 12 days.

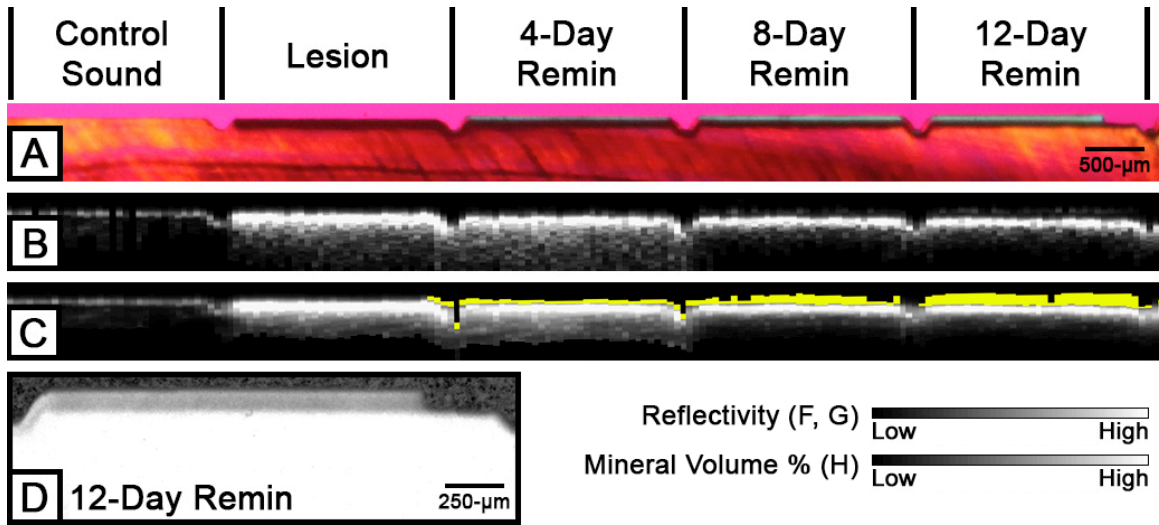


Figure 3.2 PLM, CP-OCT and TMR images of the samples from the neutral pH remineralization model for the four time periods of exposure to the remineralization solution. PLM (A) and CP-OCT B-scans (unprocessed B; processed C) images show decreased depth of the lesion body as well as an increase in transparent surface layer thickness over the periods of exposure to remineralization solution. The transparent surface layer is highlighted in yellow in PS-OCT image (C). TMR image (D) shows increased mineralization of the lesion after exposure to remineralization solution for 12 days.

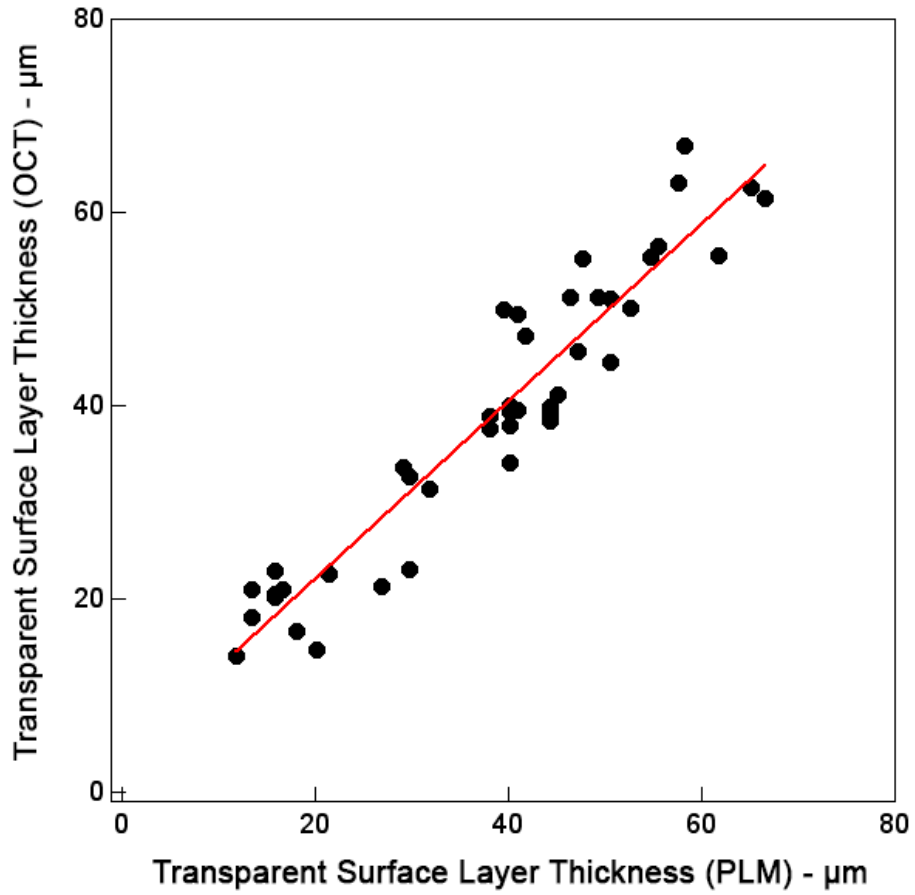


Figure 3.3 A plot of transparent surface layer thickness estimated from the automated algorithm (PS-OCT) vs. thickness determined with histology (PLM). Only the true-positive windows are shown above (n = 44).

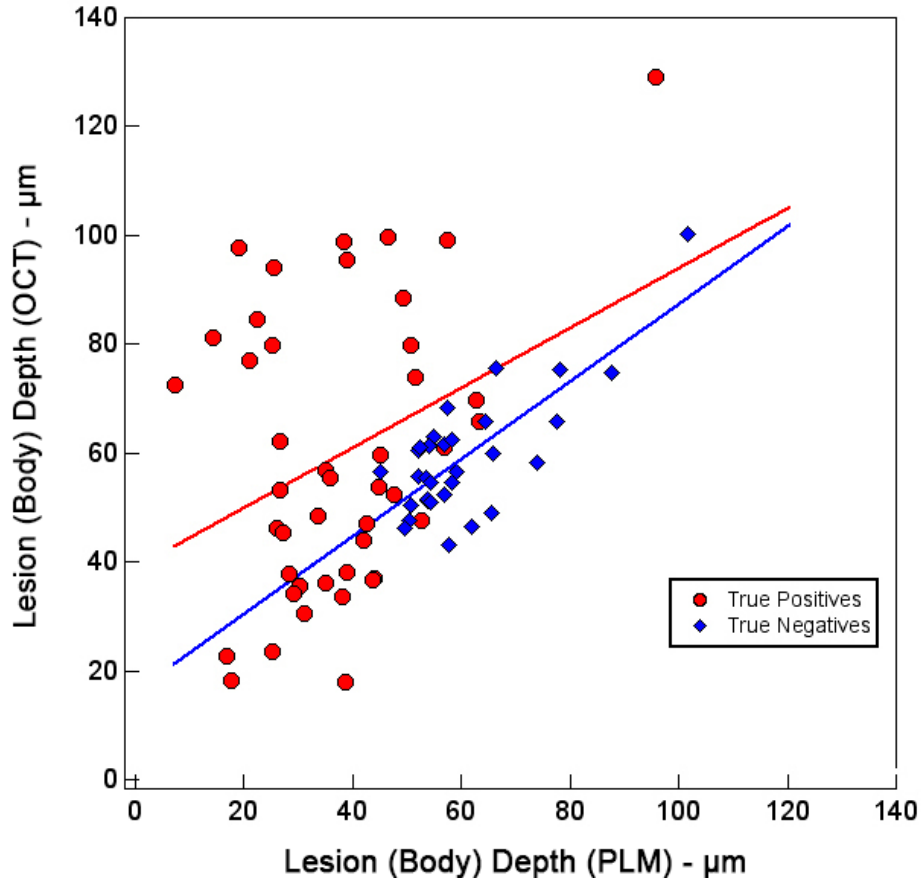


Figure 3.4 A plot of estimated lesion (body) depth measurements vs. lesion (body) depth determined with histology (PLM). True-positive windows exhibited the transparent surface layer with both PS-OCT and PLM (n = 44). True-negative windows did not exhibit the transparent surface layer with both PS-OCT and PLM (n = 31). The FWHM method was used for lesion (body) depth estimation. The line with matching color represents the best-fit line.

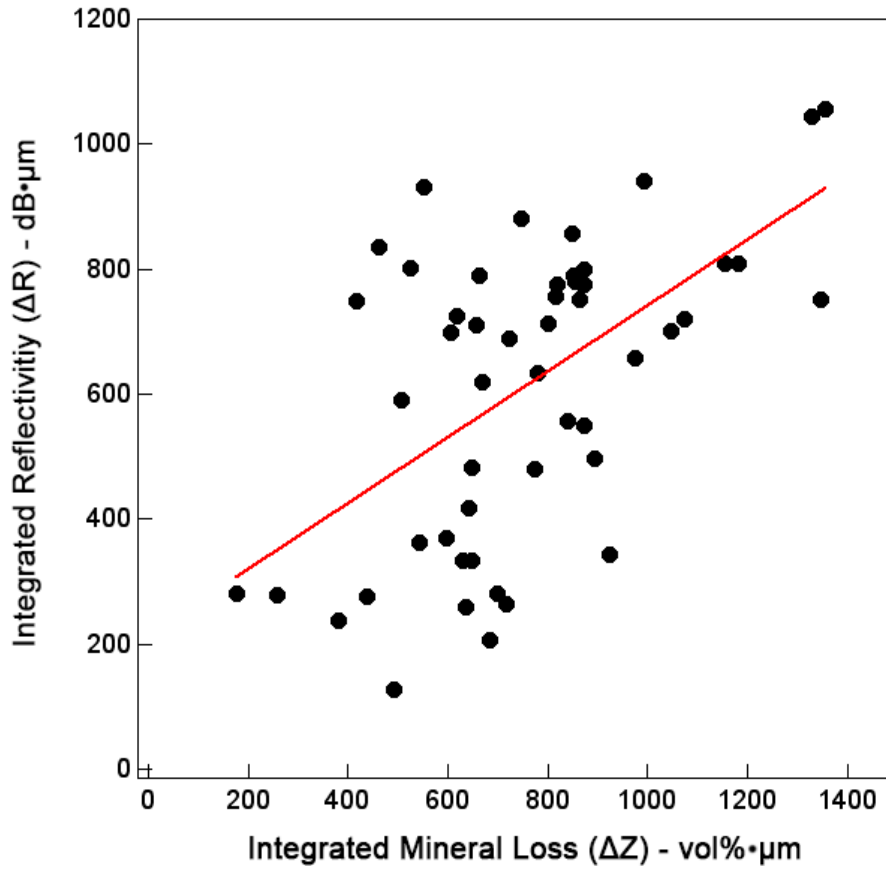


Figure 3.5 A plot of integrated reflectivity, ΔR , over the estimated lesion (body) depth (PS-OCT) vs. integrated mineral loss, ΔZ , over 200 μm (TMR). Windows with uneven thickness or fractured surface were excluded from the comparison (n = 52).

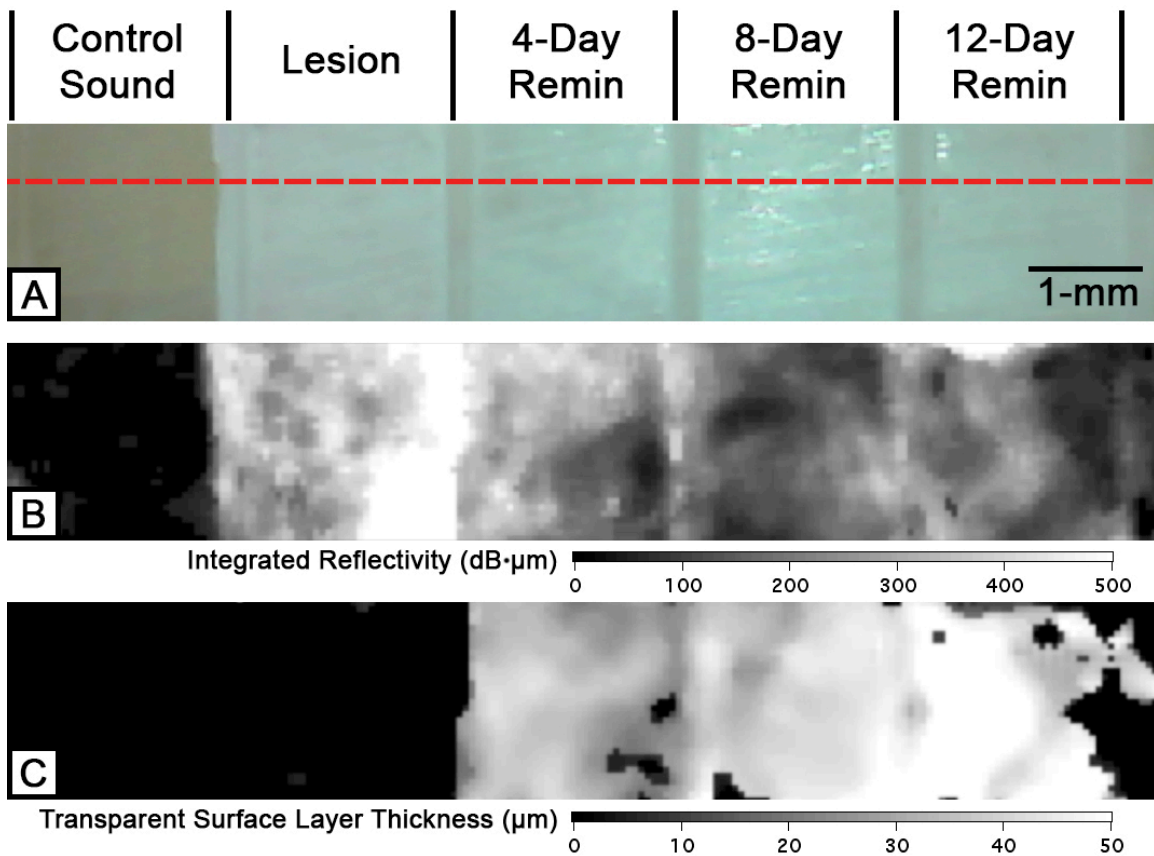


Figure 3.6 Two-dimensional projection images of the acidic pH remineralization sample. A red dotted line in the visible light reflectance image (A) represents the section shown in Figs. 1A-C. Two-dimensional OCT surface projection images of the same sample are shown including (B) the integrated reflectivity and (C) the transparent surface layer thickness.

3.8 REFERENCES

- Arends, J., Ruben, J. L. and Inaba, D. (1997). Major topics in quantitative microradiography of enamel and dentin: R parameter, mineral distribution visualization, and hyper-remineralization. *Adv. Dent. Res.*, **11**(4): 403-414.
- Baumgartner, A., Dicht S., Hitzenberger, C. K., Sattmann, H., Robi, B., Moritz, A., Sperr, W. and Fercher, A. F. (2000). Polarization-sensitive optical coherence tomography of dental structures. *Caries Res.*, **34**: 59-69.
- Baumgartner, A., Hitzenberger, C. K., Dicht, S., Sattmann, H., Moritz, A., Sperr, W. and Fercher, A. F. (1998). Optical coherence tomography for dental structures. *Proc. SPIE Lasers in Dentistry IV*, San Jose, CA, **3248**: 130-136.
- Bush, J., Davis, P. and Marcus, M. A. (2000). All-fiber optic coherence domain interferometric techniques. *Proc. SPIE Fiber Optic Sensor Technology II*, San Jose, CA, **4204**: 71-80.
- Chan, K. H., Chan, A. C., Fried, W. A., Simon, J. C., Darling, C. L. and Fried, D. (2013). Use of 2D images of depth and integrated reflectivity to represent the severity of demineralization in cross-polarization optical coherence tomography. *J. Biophotonics*, **8**: 36-45.
- Chong, S. L., Darling, C. L. and Fried, D. (2007). Nondestructive measurement of the inhibition of demineralization on smooth surfaces using polarization-sensitive optical coherence tomography. *Lasers Surg. Med.*, **39**(5): 422-427.
- Darling, C. L., Featherstone, J. D. B., Le, C. Q. and Fried, D. (2009). An automated digital microradiography system for assessing tooth demineralization. *Proc. SPIE Lasers in Dentistry VX*, San Jose, CA, **7162**: T1-7.
- Darling, C. L., Huynh, G. D. and Fried, D. (2006). Light scattering properties of natural and artificially demineralized dental enamel at 1310 nm. *J. Biomed. Opt.*, **11**(3): 34023.
- Ekstrand, K. R., Zero, D. T., Martignon, S. and Pitts, N. B. (2009). Lesion activity assessment. *Monogr. Oral Sci.*, **21**: 63-90.
- Everett, M. J., Colston, B. W., Sathyam, U. S., Silva, L. B. D., Fried, D. and Featherstone, J. D. B. (1999). Non-invasive diagnosis of early caries with polarization sensitive optical coherence tomography (PS-OCT). *Proc. SPIE Lasers in Dentistry V*, San Jose, CA, **3593**: 177-182.
- Featherstone, J. D. (2000). The science and practice of caries prevention. *J. Am. Dent. Assoc.*, **131**(7): 887-899.

- Featherstone, J. D. B. (1996). Clinical implications: new strategies for caries prevention. *Proc. the 1st Annual Indiana Conference: Early Detection of dental caries*, Indianapolis, IN, 287-296.
- Featherstone, J. D. B., Glena, R., Shariati, M. and Shields, C. P. (1990). Dependence of *in vitro* demineralization and remineralization of dental enamel on fluoride concentration. *J. Dent. Res.*, **69**: 620-625.
- Fejerskov, O. and Kidd, E., Eds. (2003). *Dental caries: the disease and its clinical management*. Oxford, Blackwell.
- Fercher, A., Hitzengerger, C., Sticker, M., Zawadzki, R., Karamata, B. and Lasser, T. (2001). Numerical dispersion compensation for Partial Coherence Interferometry and Optical Coherence Tomography. *Opt. Express*, **9**(12): 610-615.
- Fried, D., Xie, J., Shafi, S., Featherstone, J. D. B., Breunig, T. M. and Le, C. Q. (2002). Early detection of dental caries and lesion progression with polarization sensitive optical coherence tomography. *J. Biomed. Opt.*, **7**(4): 618-627.
- Jones, R. S., Darling, C. L., Featherstone, J. D. B. and Fried, D. (2006). Imaging artificial caries on the occlusal surfaces with polarization-sensitive optical coherence tomography. *Caries Res.*, **40**(2): 81-89.
- Jones, R. S., Darling, C. L., Featherstone, J. D. B. and Fried, D. (2006). Remineralization of *in vitro* dental caries assessed with polarization sensitive optical coherence tomography. *J. Biomed Opt.*, **11**(1): 014016.
- Jones, R. S. and Fried, D. (2005). The effect of high-index liquids on PS-OCT imaging of dental caries. *Proc. SPIE Lasers in Dentistry XI*, San Jose, CA, **5687**: 34-41.
- Kang, H., Darling, C. L. and Fried, D. (2012). Nondestructive monitoring of the repair of enamel artificial lesions by an acidic remineralization model using polarization-sensitive optical coherence tomography. *Dent. Mater.*, **28**(5): 488-494.
- Kang, H., Jiao, J. J., Lee, C., Le, M. H., Darling, C. L. and Fried, D. L. (2010). Nondestructive assessment of early tooth demineralization using cross-polarization optical coherence tomography. *IEEE J. Sel. Top. Quantum Electron.*, **16**(4): 870-876.
- Kidd, E. A. (1983). The histopathology of enamel caries in young and old permanent teeth. *Br. Dent. J.*, **155**(6): 196-198.
- Lee, C., Darling, C. L. and Fried, D. (2009). Polarization-sensitive optical coherence tomographic imaging of artificial demineralization on exposed surfaces of tooth roots. *Dent. Mater.*, **25**(6): 721-728.

Lee, R. C., Darling, C. L. and Fried, D. (2014). Automated detection of remineralization in simulated enamel lesions with PS-OCT. *SPIE Lasers in Dentistry XX*, San Jose, CA, **8929**: E1-8.

Lee, Y. K. and Rhodes, W. T. (1990). Nonlinear image processing by a rotating kernel transformation. *Opt. Lett.*, **15**(23): 1383-1385.

Liu, Y., Mai, S., Li, N., Yiu, C. K., Mao, J., Pashley, D. H. and Tay, F. R. (2011). Differences between top-down and bottom-up approaches in mineralizing thick, partially demineralized collagen scaffolds. *Acta. Biomater.*, **7**(4): 1742-1751.

Manesh, S. K., Darling, C. L. and Fried, D. (2009). Polarization-sensitive optical coherence tomography for the nondestructive assessment of the remineralization of dentin. *J. Biomed. Opt.*, **14**(4): 044002.

Nam, K. H., Jeong, B., Jung, I. O., Ha, H., Kim, K. H. and Lee, S. J. (2011). Measurement of anisotropic reflection of flowing blood using optical coherence tomography. *J. Biomed. Opt.*, **16**(12): 120502.

Ngotheppitak, P., Darling, C. L. and Fried, D. (2005). Measurement of the severity of natural smooth surface (interproximal) caries lesions with polarization sensitive optical coherence tomography. *Lasers Surg. Med.*, **37**(1): 78-88.

NIH (2001). Diagnosis and management of dental caries throughout life, *NIH Consensus Statement*, **18**: 1-24.

Silverstone, L. M., Wefel, J. S., Zimmerman, B. F., Clarkson, B. H. and Featherstone, M. J. (1981). Remineralization of natural and artificial lesions in human dental enamel in vitro. Effect of calcium concentration of the calcifying fluid. *Caries Res.*, **15**(2): 138-157.

ten Cate, J. M. and Arends, J. (1977). Remineralization of artificial enamel lesions in vitro. *Caries Res.*, **11**(5): 277-286.

ten Cate, J. M. and Featherstone, J. D. B. (1991). Mechanistic aspects of the interactions between fluoride and dental enamel. *Crit. Rev. Oral Biol. Med.*, **2**: 283-296.

Thylstrup, A., Bruun, C. and Holmen, L. (1994). In vivo caries models-mechanisms for caries initiation and arrestment. *Adv. Dent. Res.*, **8**(2): 144-157.

White, D. J. (1995). The application of in vitro models to research on demineralization and remineralization of the teeth. *Adv. Dent. Res.*, **9**(3): 175-197.

Yamazaki, H. and Margolis, H. C. (2008). Enhanced enamel remineralization under acidic conditions in vitro. *J. Dent. Res.*, **87**(6): 569-574.

CHAPTER IV

ASSESSMENT OF REMINERALIZATION VIA MEASUREMENT OF DEHYDRATION RATES WITH THERMAL AND NEAR-INFRARED REFLECTANCE IMAGING

4.1 SUMMARY

Previous studies have demonstrated that the optical changes due to the loss of water from porous lesions can be exploited to assess lesion severity with QLF, thermal and NIR imaging. Since arrested lesions are less permeable to water due to the highly mineralized surface layer, changes in the rate of water loss can be related to changes in lesion structure. The purpose of this work was to investigate whether the rate of water loss correlates with the degree of remineralization and whether that rate can be measured using thermal and NIR reflectance imaging. Artificial bovine (n=30) enamel lesions were prepared by immersion in a demineralization solution for either 8 and 24 hours and they were subsequently placed in an acidic remineralization solution for different periods. The samples were dehydrated using an air spray for 30 seconds and surfaces were imaged using a thermal camera and an InGaAs camera at 1300-1700 nm wavelengths. The area enclosed by the time-temperature curve, ΔQ , from thermal imaging showed significant differences ($P < 0.05$) between the lesion window and other windows. NIR reflectance intensity differences, ΔI , before and after dehydration decreased with longer periods of remineralization. Only NIR reflectance imaging was capable of detecting significant differences ($P < 0.05$) between the different periods of remineralization. This chapter demonstrates that both thermal and NIR reflectance imaging are suitable for the detection of remineralization in simulated caries lesions and NIR wavelengths longer than 1400 nm are well suited for the assessment of remineralization.

4.2 INTRODUCTION

Dental caries is a major oral health problem in most industrialized countries (Petersen 2003). Since the introduction of fluoride to the drinking water, use of fluoride dentifrices and rinses, application of topical fluoride in dental office and improved dental hygiene, the rate of dental caries declined significantly (1994, NIH 2001, Fejerskov and Kidd 2003). Fluoride slows demineralization and enhances remineralization by promoting crystal growth and producing fluorapatite crystals that are much more resistant to acid challenge than the original hydroxyapatite of enamel and dentin. Lesions can be arrested by the preferential deposition of mineral at the lesion surface that inhibits diffusion (ten Cate and Arends 1977, Kidd 1983, ten Cate and Featherstone 1991). An accurate assessment of lesion activity and severity is paramount for clinical diagnosis. Current methods for lesion assessment are composed of visual and tactile exams, which are prone to subjective bias, interference from staining, are limited to exposed surfaces and may cause permanent damage to the tooth structure (NIH 2001, Ekstrand et al. 2009). In addition, arrested lesions still retain the white coloration due to reflectance from the underlying body of the lesion (Fejerskov and Kidd 2003), which may lead to an incorrect diagnosis of caries activity (Ekstrand et al. 2009). Gold standards for lesion assessment such as transverse microradiography (TMR) and polarized light microscopy (PLM) require destruction of the tooth, and are unsuitable for use *in-vivo*. New methods are needed to assess lesion activity and avoid unnecessary cavity preparations. Several studies have demonstrated that PS-OCT is uniquely capable of this task since it provides a measurement of the reflectivity from each layer of the lesion and is able to show the formation of a zone of increased mineral density

and reduced light scattering due to remineralization (Jones et al. 2006, Manesh et al. 2009, Kang et al. 2010). In a previous PS-OCT study, we developed approaches to automatically detect the surface layer and measure its thickness with high accuracy (Lee et al. 2014).

Early caries lesions can be described as non-cavitated subsurface lesions with an intact surface layer (Fejerskov and Kidd 2003). The lesion body manifests increased porosity due to mineral loss while the surface layer is maintained due to mineral deposition from the saliva. Mobile water filling the pores of the lesion body can evaporate through micropores in the surface layer (Zahradnik and Moreno 1977). As the lesion becomes arrested or undergoes remineralization, the permeability of the surface layer significantly decreases (Lepri et al. 2013). Thus, the rate of evaporation of water from the lesion depends on the lesion structure. The optical changes associated with water loss have been exploited via quantitative light-induced fluorescence (QLF) (Ando et al. 2006), thermal imaging (Kaneko et al. 1999, Zakian et al. 2010) and NIR imaging (Usenik et al. 2014). Evaporation of water from a lesion is an endothermic process, which causes a temperature decrease followed by a recovery to thermal equilibrium as the lesion becomes dry. Kaneko et al. and Zakian et al. carried out thermal imaging studies using an infrared camera and an air-jet for evaporation on occlusal and smooth natural tooth surfaces (Kaneko et al. 1999, Zakian et al. 2010). Ando et al. reported that pulse thermography is sensitive to the mineralization state of the tooth and has potential to be used in lesion activity assessment (Ando et al. 2012).

Near-infrared (NIR) imaging has been also exploited for caries detection since sound enamel is transparent in the NIR and the scattering coefficient increases

exponentially with increasing mineral loss (Darling et al. 2006). Other studies have shown that reflectance and transillumination imaging were able to show demineralization on buccal and occlusal surfaces with high contrast at NIR wavelengths (Lee et al. 2009, Wu and Fried 2009). Zakian et al. carried out NIR reflectance measurements from 1000–2500 nm using a hyperspectral imaging system and showed that the reflectance from sound tooth areas decreases at longer wavelengths where water absorption is higher (Zakian et al. 2009). Recent studies at NIR wavelengths coincident with high water absorption, i.e. 1460 nm and > 1500-nm for artificial and natural lesions demonstrated extremely high lesion contrast (Chung et al. 2011, Fried et al. 2013, Simon et al. 2014). In this chapter, NIR reflectance imaging was used to determine if this phenomenon could be similarly exploited to monitor remineralization.

In a previous study, we found that the mean attenuation coefficient of enamel increased significantly at 1310 nm if samples are dehydrated (Maung et al. 2010, Chung et al. 2011). This suggests that changes in water content have a more profound effect on enamel transparency at NIR wavelengths than in the visible. Usenik et al. demonstrated that the rate of water evaporation from enamel increased with the severity of demineralization using NIR hyperspectral imaging and that the water content could be estimated with an appropriate drying model (Usenik et al. 2014). The magnitude of water absorption increases between 1400 and 1700 nm and we hypothesize these NIR wavelengths are more sensitive to changes in lesion hydration (Chung et al. 2011).

The influence of hydration on enamel lesions can be investigated as an indirect indicator of the decreased permeability of water due to remineralization. In this chapter, we measured optical changes in simulated enamel lesions that have undergone

remineralization during controlled drying using thermography and NIR reflectance imaging.

4.3 MATERIALS AND METHODS

4.3.1 Sample Preparation

Enamel blocks (n = 30), approximately 8–12 mm in length with a width of 2 mm and a thickness of 3 mm were prepared from extracted bovine incisors acquired from a slaughterhouse. The surfaces of the bovine enamel blocks were ground to a 9 µm finish. Each sample was partitioned into six regions or windows (1 sound control, 4 lesion and 1 remineralization control) by etching small incisions 1.8 mm apart across each of the enamel blocks using a laser. Incisions were etched using a transverse excited atmospheric pressure (TEA) CO₂ laser, an Impact 2500, GSI Lumonics (Rugby, UK), operating at 9.3 µm with a pulse duration of 15 µs, a pulse repetition rate of 200 Hz and a fluence of 20 J/cm².

A thin layer of acid-resistant varnish in the form of nail polish, Revlon (New York, NY), was applied to protect the sound and remineralization control windows before exposure to the demineralization solution. Two groups (n = 15 per group) of enamel samples each with four exposed lesion windows were immersed in 45 mL aliquots of the demineralization solution for 8 and 24 hours, respectively. The demineralization solution, which was maintained at 37°C and pH 4.8, was composed of 2.0 mmol/L calcium, 2.0 mmol/L phosphate and 0.075 mol/L acetate. After the demineralization period, the acid resistant varnish was removed by immersion in acetone in an ultrasonic

bath for 15 minutes and the acid-resistant varnish was applied again to the sound and lesion windows.

Sample windows were subsequently exposed to an acidic remineralization solution for 4, 8 or 12-days by covering appropriate windows with acid resistant varnish at each time point. It has been hypothesized that the lower pH reduces preferential deposition of mineral in the outer enamel, enhancing remineralization of the lesion body (Yamazaki and Margolis 2008). The acidic remineralization solution was composed of 4.1 mmol/L calcium, 15 mmol/L phosphate, 50 mmol/L lactic acid, 20 mmol/L HEPES buffer and 2 ppm F⁻ maintained at 37°C and a pH of 4.8 (Yamazaki and Margolis 2008). The remineralization control window was exposed to the acidic remineralization solution for 12 days in order to examine its effect on sound enamel. After the 12 days of remineralization, the acid resistant varnish was removed and the samples were stored in 0.1 % thymol solution to prevent fungal and bacterial growth.

4.3.2 PS-OCT System

The PS-OCT system used in this work has been described previously (Fried et al. 2002). An all fiber-based Optical Coherence Domain Reflectometry (OCDR) system with polarization maintaining (PM) optical fiber, high speed piezoelectric fiber-stretchers and two balanced InGaAs receivers that was designed and fabricated by Optiphase, Inc., Van Nuys, CA was used to acquire the images (Bush et al. 2000). This two-channel system was integrated with a broadband superluminescent diode (SLD) DL-CS3159A, Denselight (Jessup, MD) and a high-speed XY-scanning motion controller system, ESP 300 controller with ILS100PP and 850G-HS stages, (Newport, Irvine, CA) for *in-vitro*

optical tomography. A high power (15 mW) polarized SLD source operated at a center wavelength of 1317 nm with a spectral bandwidth full-width-half-maximum (FWHM) of 84 nm was used to provide an axial resolution of 9 μm in air and 6 μm in enamel (refractive index = 1.6). Light from the sample arm was focused onto the sample surface using a 20 mm focal length plano-convex lens providing a lateral resolution of approximately 20 μm .

The PS-OCT system was completely controlled using LabView™ software (National Instruments, Austin, TX). Samples were dried with pressurized air for 30 seconds prior to scanning. Each B-scan consisted of 300 A-scans spaced 50 μm apart. The A-scan sweep rate was 150 Hz with a dynamic range of 48 dB and each A-scan was an average of 10 scans. The total number of data points in each A-scan was 2000 over a scan range of approximately 5 mm in air.

4.3.3 Calculation of Transparent Surface Layer Thickness, Lesion Depth and Integrated Reflectivity (ΔR)

PS-OCT images were processed using a dedicated program constructed with LabView™ software. There was a phase shift in the PM-fiber between the two axes, so an axial position calibration was performed once prior to the experiment. A gold mirror was scanned at a 150 Hz sweep rate and each A-scan was an average of 100 scans. Five hundred A-scans were acquired at 10 μm intervals over the entire scan range to determine the required axial position adjustments and the axial position of the cross-polarization scan images was adjusted to match the co-polarization scan images.

Image processing methods for surface layer detection and measurement method utilized an edge detection technique using the zero-crossing first-order derivative as described previously (Lee et al. 2014, Lee et al. 2014). In this work, the threshold values for the ratio of the intensities of the two peaks were further specified to 0.1 for the co-polarization axis and 0.5 for the cross-polarization axis.

Previous studies have shown that the integrated reflectivity, ΔR , over the estimated lesion depth positively correlates with the integrated mineral loss (volume percent mineral loss $\times \mu\text{m}$), ΔZ (Ngaotheppitak et al. 2005, Jones et al. 2006). ΔR was calculated by integrating from the base of the transparent layer through the entire estimated lesion body in the CP-OCT images (Lee et al. 2014). This had the added advantage of removing the contribution of the high specular reflection at the surface of the transparent layer, which was large enough to be present even in the CP-OCT images.

A region of interest (ROI) was specified for the sound region from each sample in order to discriminate between demineralized and sound enamel. ΔR was calculated from the selected ROI and it was compared to the ΔR of the lesions in order to reduce false-positives in lesion detection. The transparent surface layer, lesion depth and ΔR measurements were estimated by averaging 25 A-scans from a 5×5 pixel region of interest. A 5×5 pixel median filter was applied to the final 2D projection images for improved visualization.

4.3.4 Dehydration Measurements

The following setup was used for the dehydration experiments of sec. 4.3.5 and 4.3.6. Each sample was placed in a mount connected to a high-speed XY-scanning motion controller system, Newport ESP 300 controller & 850G-HS stages coupled with an air nozzle and a light source as shown in **Fig. 4.1**. All surfaces excluding the windows were covered with black nail polish, OPI (North Hollywood, CA) in order to confine water loss to the exposed surface and prevent the transmission of light through the sides of the sample. Each sample was immersed in the water bath for 30 seconds while being vigorously shaken to enhance water diffusion. After the sample was removed from the water bath, an image was captured as an initial reference image and the air spray was activated. The air pressure was set to 15 psi and the computer controlled air nozzle was positioned 2 cm away from the sample. Each measurement consisted of capturing a sequence of images at 4 frames per second for 30 seconds. For each measurement, the air nozzle and the light source were centered on the ROI, and this process was repeated for each window (6 times per sample). The dehydration setup was completely automated using LabView™ software. All windows from all samples were exposed to the same dehydration protocol.

4.3.5 Thermal Imaging and Analysis

A Model A65 infrared (IR) thermography camera (FLIR Systems, Wilsonville, OR) sensitive from 7.5 - 13 μm with a resolution of 640 x 512 pixels, a thermal sensitivity of 50 mK and a lens with a 13 mm focal length was used to record temperature changes during the dehydration process. The area per pixel was approximately 0.02 mm^2 . The

ambient room temperature, flowing air temperature and water bath temperature were approximately 21 °C (294.15 K) and were consistent throughout the experiment. The object emissivity was set to 0.91 (Lin et al. 2009), and the atmospheric temperature was set to 294.15 K. Relative humidity was set at a default value of 50%; humidity values were not recorded, but every sample was measured under the same conditions. Previous studies have shown that ΔQ , the area enclosed by the time-temperature curve, can be used as a quantitative measure of porosity and can be used to discriminate between sound and demineralized enamel *in-vitro* (Kaneko et al. 1999, Zakian et al. 2010).

Thermal images were processed and analyzed using a dedicated program written in Labview™. The thermography camera outputs a series of temperature measurements over time. The initial reference temperature measurements varied slightly (± 0.5 K) due to the different emissivity, lesion structure, mineral composition and water content among windows. Calibration was carried out via matching the measurements from the initial reference image to the ambient temperature. ΔQ was calculated from the area enclosed by the initial temperature and the time-temperature curve, acquired from an average measurement of a 3 × 3 pixel ROI for each window.

4.3.6 NIR Reflectance Imaging and Analysis

An Indigo Alpha NIR camera (FLIR Systems, Wilsonville, OR) with an InGaAs focal plane array, a spectral sensitivity range from 900 nm to 1750 nm, a resolution of 320 x 256 pixels and an InfiniMite™ lens (Infinity, Boulder, CO) was used to acquire all the images during the dehydration process. The area per pixel was approximately 0.003

mm². Light from a 150 W fiber-optic illuminator FOI-1 (E Licht Company, Denver, CO) was directed at the sample at an incident angle of approximately 60 ° in order to reduce specular reflection as shown in **Fig. 4.1**. Several band-pass (BP) and long-pass (LP) filters were used to provide different spectral distributions of NIR light. Band-pass filters centered at 1300 nm with 90 nm bandwidth (1260–1340 nm), 1460 nm with 85 nm bandwidth (1420–1500 nm) (Spectrogon, Parsippany, NJ) and long-pass filters at 1400 nm (1400–1700 nm) and 1500 nm (1500–1700 nm) (FEL LP series from Thorlabs, Newton, NJ) were used. The illuminating light intensity was set to its maximum for 1300 nm BP, 1460 nm BP and 1500 nm BP filters and to 80% of the maximum for 1400 nm LP filter in order to avoid oversaturation. Source to sample distance was fixed at 5 cm for all samples.

NIR reflectance images were processed and automatically analyzed using a dedicated program constructed with LabView™ software. A 5 × 5 pixel ROI was specified for each window and an average measurement was recorded for each time point. The image contrast was calculated using $(I_L - I_S)/I_L$ for the final image ($t = 30$), where I_S is the mean intensity of the sound enamel and I_L is the mean intensity of the lesion. In addition to lesion contrast, the intensity difference between the final and initial images, $\Delta I(t=30)$, was calculated using $I(t=30) - I_i$, where $I(t=30)$ is the mean intensity at $t = 30$ seconds and I_i is the mean intensity prior to turning on the air nozzle.

In order to investigate the rate of intensity change in conjunction with the overall intensity change, the "S"-shaped time-intensity curve was fit to a sigmoid function:

$$I(t) = \frac{a}{1+e^{b(c-t)}} + d, \quad (1)$$

where $I(t)$ is intensity value at time (t) in seconds and d was fixed at I_1 . I_1 was substituted with d in Equation 1 to yield:

$$\Delta I(t) = \frac{a}{1+e^{b(c-t)}} \quad . \quad (2)$$

Some lesion windows exhibited a "bump" in the intensity profile as shown in **Fig. 4.7** by the asterisk. If such phenomenon was observed, the time-intensity difference curve was cropped to ignore the excursion. This phenomenon was detected if an intensity value exceeded all measurements collected in the subsequent five seconds with at least a 2% difference. The Levenberg-Marquardt algorithm was used to estimate the best fit to equation 2 with parameters (a) , (b) and (c) . Since (a) represents the amplitude or the difference between two asymptotes of the sigmoid function and (b) represents the growth rate of the function, the product of these two parameters representing the overall growth rate (OGR) was calculated.

4.3.7 Polarized Light Microscopy (PLM) and Transverse Microradiography (TMR)

After sample imaging was completed, 200 μm thick serial sections were cut using an Isomet 5000 saw (Buehler, IL), for polarized light microscopy (PLM) and transverse microradiography (TMR). PLM was carried out using a Meiji Techno Model RZT microscope (Meiji Techno Co., LTD, Saitama, Japan) with an integrated digital camera, Canon EOS Digital Rebel XT (Canon Inc., Tokyo, Japan). The sample sections were imbibed in water and examined in the brightfield mode with crossed polarizers and a red

I plate with 500 nm retardation. PLM images were acquired at 40x magnification and had a resolution of 3264 x 2448 pixels.

A custom built digital microradiography (TMR) system was used to measure the volume percent mineral content in the areas of demineralization on the tooth sections (Darling et al. 2009). High-resolution microradiographs were taken using Cu K α radiation from a Philips 3100 X-ray generator and a Photonics Science FDI X-ray digital imager, Microphotonics (Allentown, PA). The X-ray digital imager consisted of a 1392 \times 1040 pixel interline CCD directly bonded to a coherent micro fiber-optic coupler that transfers the light from an optimized gadolinium oxysulfide scintillator to the CCD sensor. The pixel resolution was 2.1 μ m and the images were acquired at 10 frames per second. A high-speed motion control system with Newport UTM150 and 850G stages and an ESP 300 controller coupled to a video microscopy and a laser targeting system was used for precise positioning of the sample in the field of view of the imaging system.

4.3.8 Statistical Analysis

Sample groups were compared using repeated measures analysis of variance (ANOVA) with a Tukey–Kramer post hoc multiple comparison test. Linear regression with Pearson’s correlation was used to examine the relationship between data acquired from PS-OCT, PLM and TMR measurements. All statistical analyses were performed with 95% confidence with PrismTM (GraphPad software, San Diego, CA).

4.4 RESULTS

Figure 4.2 shows the visible, PS-OCT and PLM images of one of the samples from the initial 24-hour demineralization group after exposure to remineralization. Windows exposed to the demineralization solution could be discriminated from sound and remineralization control windows by visual examination as shown in **Fig. 4.2A**, but not from the 4, 8, or 12-day remineralization windows. In contrast, the changes to the mineral subsurface structure upon demineralization and remineralization could be easily seen with PS-OCT and histology (PLM), **Figs. 4.2D and 4.2E**. The transparent surface layer was clearly visible in the PLM image of a cross-section (**Fig. 4.2D**) and the algorithm was able to detect the transparent surface layer highlighted in yellow in the CP-OCT b-scan image as shown in **Fig. 4.2E**. Even though the pH of the remineralization solution was acidic at 4.8, the remineralization control window was not affected by the supersaturated acidic calcifying solution with 2 ppm fluoride as shown in the PLM image (**Fig. 4.2D**) and no significant changes from the sound window were detected by PS-OCT (**Figs. 4.2B, 4.2C and 4.2E**). There was a significant increase in the thickness of transparent surface layer and a significant decrease in the lesion severity with increasing period of remineralization. The transparent surface layer thickness, lesion depth and lesion severity measurements taken with PS-OCT, PLM and TMR are listed in **Table 4.1**.

In our previous study, the algorithm successfully detected the transparent surface layers with high sensitivity (0.92) and high specificity (0.97) (Lee et al. 2014). In this work, the modified algorithm was able to detect the transparent surface layer without any false positives and false negatives. The total number of windows was 150 from 30

samples, with 90 true positives and 60 true negatives. The thickness of the transparent surface layer estimated with PS-OCT, showed a strong correlation with PLM measurements (Pearson's correlation, $p < 0.0001$, $R^2 = 0.61$). The correlation coefficient, R^2 , reported in this work is weaker than the previously reported value ($R^2 = 0.90$ - ref (Lee et al. 2014)), likely due to the variations in the surface layer thickness (33 μm vs. 55 μm).

The time-lapse thermal images of the sample from **Fig. 4.2** are shown in **Fig. 4.3** and its time-temperature profiles are shown in **Fig. 4.4**. With forced air-drying, most samples approached ambient temperature within 30 seconds. **Figures 4.3 and 4.4** show that the lesion window exhibited the greatest temperature drop in the first 5 seconds of forced drying and manifested the slowest recovery to equilibrium. As the lesion was exposed to the remineralization solution, these changes became less noticeable and ΔQ measurements showed no significant difference from those of sound and the remineralization control windows as shown in **Fig. 4.5**. The mean ΔQ of the lesion windows was significantly larger than those of all the other windows for both the 8-hour and 24-hour groups as shown in **Table 4.2**. Variations in magnitude of ΔQ for the samples of the initial 24-hour demineralization group were larger than those of the initial 8-hour demineralization group.

Time-lapse NIR reflectance images acquired with the 1460 nm band-pass filter of the sample from **Fig. 4.2** are shown in **Fig. 4.6** and its time-intensity difference profile is shown in **Fig. 4.7**. The intensity difference, $\Delta I(t)$, was recorded instead of raw intensity data due to differences in anatomical structure of the sample, i.e. variation in depth to DEJ, presence of cracks, enamel tufts and birefringence due to orientation of enamel

spindles. Variation of $\Delta I(t=30)$ nicely followed changes in the lesion structure as shown in **Fig. 4.9** and **Table 4.3**. As seen in **Fig. 4.7**, the time-intensity difference profiles closely resembled a sigmoid function curve. In addition, 10 of the 15 lesion windows from the initial 24-hour demineralization group and one of the 15 lesion windows from initial 8-hour demineralization group exhibited a sharp excursion in the intensity profiles. In the cases where the "bump", noted as * in **Fig. 4.7**, was observed, curve fitting was performed ignoring that excursion for calculation of OGR. This phenomenon was confined only to the lesion windows with the most severe lesions. We explored this phenomenon further by imaging with crossed polarizers, which reduced specular reflection and successfully eliminated the bump from the profile. Therefore, it is likely that the excursion in the intensity profile is due to specular reflection from the surface of the lesion. Although the light source was directed at the sample at an incident angle of approximately 60° , the highly roughened and porous surface of the demineralized enamel may have deflected some specular reflection to the camera.

NIR reflectance performance was also analyzed at different wavelengths using four different filters as shown in **Table 4.3**. The 1300 nm band-pass (1260–1340 nm) filter yielded the lowest lesion contrast as well as the smallest differences among windows due to lower water absorption. The three other filters, 1460 nm band-pass (1420–1500 nm), 1400 nm long-pass (1400–1700 nm) and 1500 nm long-pass (1500–1700 nm), showed higher contrast.

There was considerable variation in contrast from sample to sample (large standard deviation) due to structural variations and in a few cases negative contrast values were measured. The use of intensity difference values provided more consistent

results; $\Delta I(t=30)$ manifested a decrease in intensity with increasing degree of remineralization with a 3 – 4 fold difference in magnitude between the sound and lesion windows for the samples treated for both the 8-hour and 12-hour demineralization groups, **Fig. 4.9**. OGR also showed a decreasing trend as the lesion remineralized displaying greater differences between the sound and lesion windows compared to the intensity difference (**Fig. 4.10**); the sound and lesion windows of the samples treated with the initial 24-hour demineralization showed an approximately 20 fold difference and those treated with the initial 8-hour demineralization showed an approximately 4 fold difference. Most importantly, OGR showed a significant difference between the lesion and the 4-day remineralization window while that difference was not significant for $\Delta I(t=30)$.

4.5 DISCUSSION

These results suggest that both the thermal and NIR reflectance imaging modalities are suitable for monitoring enamel remineralization. Enamel is permeable (Atkinson 1947) and it is composed of approximately 96 % mineral and up to 3% water by weight (Weatherell 1975). Demineralized enamel can lose as much as 41% of its mineral content near the surface of the lesion by acid dissolution and remain intact as shown by depth-mineral density profiles from TMR (Arends et al. 1997) and these pores are occupied by mobile water after demineralization (Myers 1965, Zahradnik and Moreno 1977). However, in remineralized lesions, the highly mineralized surface layer inhibits free diffusion from the lesion body to the outer surface. Therefore, the rate of loss of

mobile water from the lesion is likely to be highly dependent on the thickness and mineral content of that highly mineralized surface layer.

During the dehydration process, heat loss is caused by two major mechanisms: the varying temperature between the flowing air and the sample, as well as the highly endothermic evaporation of water molecules from the surface of the sample (Zahradnik and Moreno 1977). Kaneko et al. reported that thermography data could be used to obtain quantitative information on the extent of demineralization such as lesion area, mineral loss and lesion depth and that ΔQ was correlated with ΔZ (Kaneko et al. 1999). Zakian et al. showed that ΔQ maps created on the tooth occlusal surface manifested high correlation with histological scores based on visual diagnosis (Zakian et al. 2010).

We expected ΔQ to decrease as the lesion was exposed to the remineralization solution. Although there were significant differences in the mean ΔQ values between the lesion and the other windows, thermal imaging failed to show significant differences between the individual remineralization windows or between the sound and remineralization windows as shown in **Fig. 4.5** and **Table 4.2**.

Changes in water and mineral composition due to demineralization can be observed as changes in optical properties such as light scattering and birefringence (Baumgartner et al. 2000, Zhang et al. 2000). Since sound enamel is virtually transparent in the NIR with optical attenuation 1-2 orders magnitude less than in the visible, demineralized enamel can be discriminated from sound enamel with high contrast at NIR wavelengths (Chung et al. 2011, Fried et al. 2013, Simon et al. 2014). In a previous study, it was shown that the state of hydration of the tooth had a profound effect on the optical transparency of sound enamel; empty pores act as scattering sites

at NIR wavelengths (Chung et al. 2011). **Figure 4.8** and **Table 4.3** show a decreasing trend in lesion contrast measurements with periods of remineralization at all NIR wavelengths. Wavelengths between 1400 nm and 1700 nm yielded the largest differences between windows due to increased absorption by water (Chung et al. 2011). However, the lesion contrast measurements were highly variable due to anatomical variation among samples and $\Delta I(t)$ was employed to minimize this discrepancy. The $\Delta I(t)$ profiles closely resembled a sigmoid function and OGR was calculated from the curve-fit to explain their behavior. **Figure 4.10** and **Table 4.3** show that OGR is also useful for detecting and assessing progression of remineralization.

4.6 CONCLUSION

The highly mineralized surface layer plays an important role in the dehydration process of remineralized enamel lesions. It appears that both the thermal and NIR imaging methods are suitable for detection of remineralization and are therefore highly promising for the clinical assessment of lesion activity. However, NIR reflectance imaging at wavelengths between 1400 nm and 1700 nm was also capable of detecting significant differences between different periods of remineralization and was therefore the most effective for imaging during the dehydration process.

4.7 FIGURES AND FIGURE LEGENDS

Table 4.1 Mean \pm S.D. of PS-OCT, PLM and TMR measurements for the 8 and 24-hour demineralization groups. Groups with the same letters are statistically similar, $P > 0.05$ in each row ($n = 15$).

	Lesion	4-day Remin	8-day Remin	12-day Remin	Remin Control
24-hour Demineralization (n = 15)					
Transparent Layer Thickness (PS-OCT, μm)	0 a	24.9 \pm 5.3 b	30.8 \pm 4.7 c	35.2 \pm 6.1 d	0 a
Transparent Layer Thickness (PLM, μm)	0 a	25.5 \pm 6.6 b	31.0 \pm 4.6 c	35.6 \pm 4.6 d	0 a
Lesion Body Depth (PS-OCT, μm)	40.2 \pm 6.1 a	46.2 \pm 10.6 a	45.4 \pm 11.6 a	42.3 \pm 12.9 a	0 b
Lesion Body Depth (PLM, μm)	42.3 \pm 8.1 a	44.9 \pm 9.5 a	46.6 \pm 10.0 a	44.0 \pm 15.9 a	0 b
Integrated Reflectivity, ΔR (dB \times μm)	1033 \pm 121 a	952 \pm 171 ab	900 \pm 145 b	777 \pm 102 c	0 d
Integrated Mineral Loss, ΔZ (vol% \times μm)	1433 \pm 612 a	736 \pm 270 b	693 \pm 283 b	393 \pm 278 c	-43 \pm 130 d
8-hour Demineralization (n = 15)					
Transparent Layer Thickness (PS-OCT, μm)	1.3 \pm 5.2 a*	23.6 \pm 5.6 b	24.6 \pm 5.5 b	24.3 \pm 7.7 b	0 a
Transparent Layer Thickness (PLM, μm)	1.2 \pm 4.5 a*	21.7 \pm 5.0 b	22.7 \pm 6.3 b	22.7 \pm 8.2 b	0 a
Lesion Body Depth (PS-OCT, μm)	30.7 \pm 7.6 a	42.9 \pm 9.2 b	44.9 \pm 15.9 b	47.0 \pm 14.3 b	0 c
Lesion Body Depth (PLM, μm)	29.3 \pm 6.3 a	29.8 \pm 12.4 a	26.4 \pm 15 a	20.0 \pm 13.9 a	0 b
Integrated Reflectivity, ΔR (dB \times μm)	790 \pm 146 a	734 \pm 173 a	756 \pm 161 a	666 \pm 101 a	0 b
Integrated Mineral Loss, ΔZ (vol% \times μm)	800 \pm 317 a	347 \pm 264 b	300 \pm 257 b	195 \pm 262 b	1 \pm 129 c

*One lesion window exhibited the transparent surface layer.

Table 4.2 Mean \pm S.D. ΔQ from thermal imaging measurements for each window for the 8 and 24-hour demineralization groups. Groups with the same letters are statistically similar, $P > 0.05$ in each row ($n = 15$).

	Sound	Lesion	4 Day Remin	8 Day Remin	12 Day Remin	Remin Control
24 Hour Demineralization (n = 15)						
ΔQ (K x s)	24.7 \pm 14.4 a	46.3 \pm 14.9 b	21.5 \pm 11.2 a	18.2 \pm 9.2 a	18.7 \pm 7.9 a	15.1 \pm 6.0 a
8 Hour Demineralization (n = 15)						
ΔQ (K x s)	15.6 \pm 14.8 a	24.6 \pm 14.4 b	9.6 \pm 9.5 a	7.9 \pm 6.8 a	9.0 \pm 6.4 a	8.8 \pm 7.6 a

Table 4.3 NIR reflectance measurements: mean \pm S.D. for lesion contrast measurements, intensity differences at $t = 30s$ ($\Delta I_{t=30}$) and overall growth rate (OGR) acquired from curve fitting for different spectral bands and periods of demineralization. Groups with the same letters are statistically similar, $P > 0.05$ in each row ($n = 15$).

	Sound	Lesion	4 Day Remin	8 Day Remin	12 Day Remin	Remin Control
Wavelength $\lambda = 1260\text{--}1340$ nm, 24-h demineralization ($n = 15$)						
Contrast	-	0.14 \pm 0.05 a	0.15 \pm 0.07 a	0.13 \pm 0.09 a	0.07 \pm 0.11 b	-0.05 \pm 0.15 c
$\Delta I(t=30)$	60 \pm 49 a	201 \pm 56 b	176 \pm 65 b	113 \pm 66 ac	98 \pm 64 ac	38 \pm 35 ad
OGR	19 \pm 10 abc	311 \pm 184 d	46 \pm 30 a	28 \pm 16 b	24 \pm 13 b	13 \pm 6 c
$\lambda = 1420\text{--}1500$ nm						
Contrast	-	0.27 \pm 0.12 a	0.21 \pm 0.16 ab	0.14 \pm 0.18 b	0.05 \pm 0.21 c	-0.16 \pm 0.34 d
$\Delta I(t=30)$	99 \pm 57 ab	385 \pm 68 c	319 \pm 128 c	229 \pm 103 d	183 \pm 79 a	75 \pm 39 b
OGR	24 \pm 14 ab	497 \pm 246 c	85 \pm 73 a	49 \pm 28 a	42 \pm 23 a	18 \pm 10 b
$\lambda = 1400\text{--}1700$ nm						
Contrast	-	0.19 \pm 0.11 a	0.18 \pm 0.13 a	0.15 \pm 0.15 a	0.05 \pm 0.16 b	-0.16 \pm 0.31 c
$\Delta I(t=30)$	166 \pm 81 ab	679 \pm 147 c	555 \pm 240 c	386 \pm 224 a	310 \pm 163 a	129 \pm 79 b
OGR	45 \pm 20 ab	898 \pm 422 c	134 \pm 70 d	92 \pm 50 a	76 \pm 41 a	32 \pm 18 b
$\lambda = 1500\text{--}1700$ nm						
Contrast	-	0.21 \pm 0.06 a	0.21 \pm 0.93 ab	0.17 \pm 0.12 b	0.09 \pm 0.11 c	-0.08 \pm 0.22 d
$\Delta I(t=30)$	103 \pm 51 ab	325 \pm 86 c	295 \pm 127 c	200 \pm 111 a	163 \pm 86 a	67 \pm 50 b
OGR	23 \pm 12 abc	441 \pm 219 d	78 \pm 66 a	43 \pm 26 b	39 \pm 20 b	15 \pm 10 c
Wavelength $\lambda = 1260\text{--}1340$ nm, 8-h demineralization ($n = 15$)						
Contrast	-	0.13 \pm 0.08 abc	0.15 \pm 0.13 ab	0.14 \pm 0.17 a	0.09 \pm 0.20 b	-0.02 \pm 0.27 c
$\Delta I(t=30)$	38 \pm 59 a	128 \pm 78 b	88 \pm 69 a	67 \pm 72 a	73 \pm 60 ab	47 \pm 38 a
OGR	9 \pm 25 a	36 \pm 19 b	19 \pm 15 a	15 \pm 12 a	23 \pm 22 ab	16 \pm 14 a
$\lambda = 1420\text{--}1500$ nm						
Contrast	-	0.18 \pm 0.15 ab	0.16 \pm 0.17 ab	0.13 \pm 0.26 a	0.05 \pm 0.31 b	-0.09 \pm 0.33 c
$\Delta I(t=30)$	69 \pm 67 a	225 \pm 81 b	127 \pm 74 c	112 \pm 73 ac	124 \pm 71 c	82 \pm 37 ac
OGR	15 \pm 8 a	83 \pm 40 b	23 \pm 4 a	18 \pm 13 a	26 \pm 26 a	17 \pm 7 a
$\lambda = 1400\text{--}1700$ nm						
Contrast	-	0.22 \pm 0.11 ab	0.20 \pm 0.14 ab	0.20 \pm 0.17 a	0.10 \pm 0.22 b	-0.05 \pm 0.29 c
$\Delta I(t=30)$	140 \pm 98 a	436 \pm 224 b	259 \pm 173 c	203 \pm 157 a	201 \pm 119 a	156 \pm 91 a
OGR	32 \pm 19 ab	166 \pm 116 b	47 \pm 31 a	32 \pm 25 b	44 \pm 36 ab	31 \pm 15 ab
$\lambda = 1500\text{--}1700$ nm						
Contrast	-	0.20 \pm 0.12 ab	0.17 \pm 0.18 ab	0.15 \pm 0.25 a	0.08 \pm 0.26 b	-0.03 \pm 0.30 c
$\Delta I(t=30)$	68 \pm 52 a	212 \pm 101 b	139 \pm 82 c	106 \pm 76 ac	109 \pm 58 ac	80 \pm 39 ac
OGR	15 \pm 11 a	58 \pm 24 b	25 \pm 16 c	17 \pm 13 ac	19 \pm 11 ac	13 \pm 7 ac

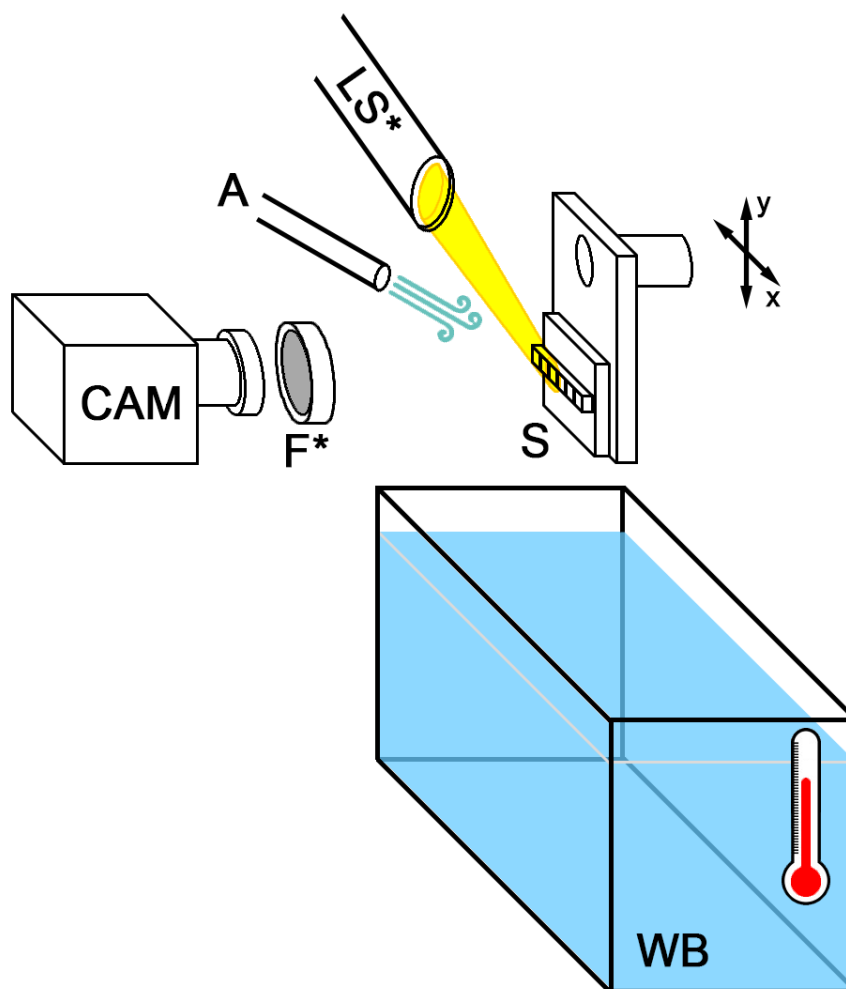


Figure 4.1 Dehydration experimental setup: CAM: image capturing device, A: compressed air nozzle, LS*: tungsten light source, S: sample, F*: filter, WB: water bath.

*Light source and filter were absent in the thermal imaging setup.

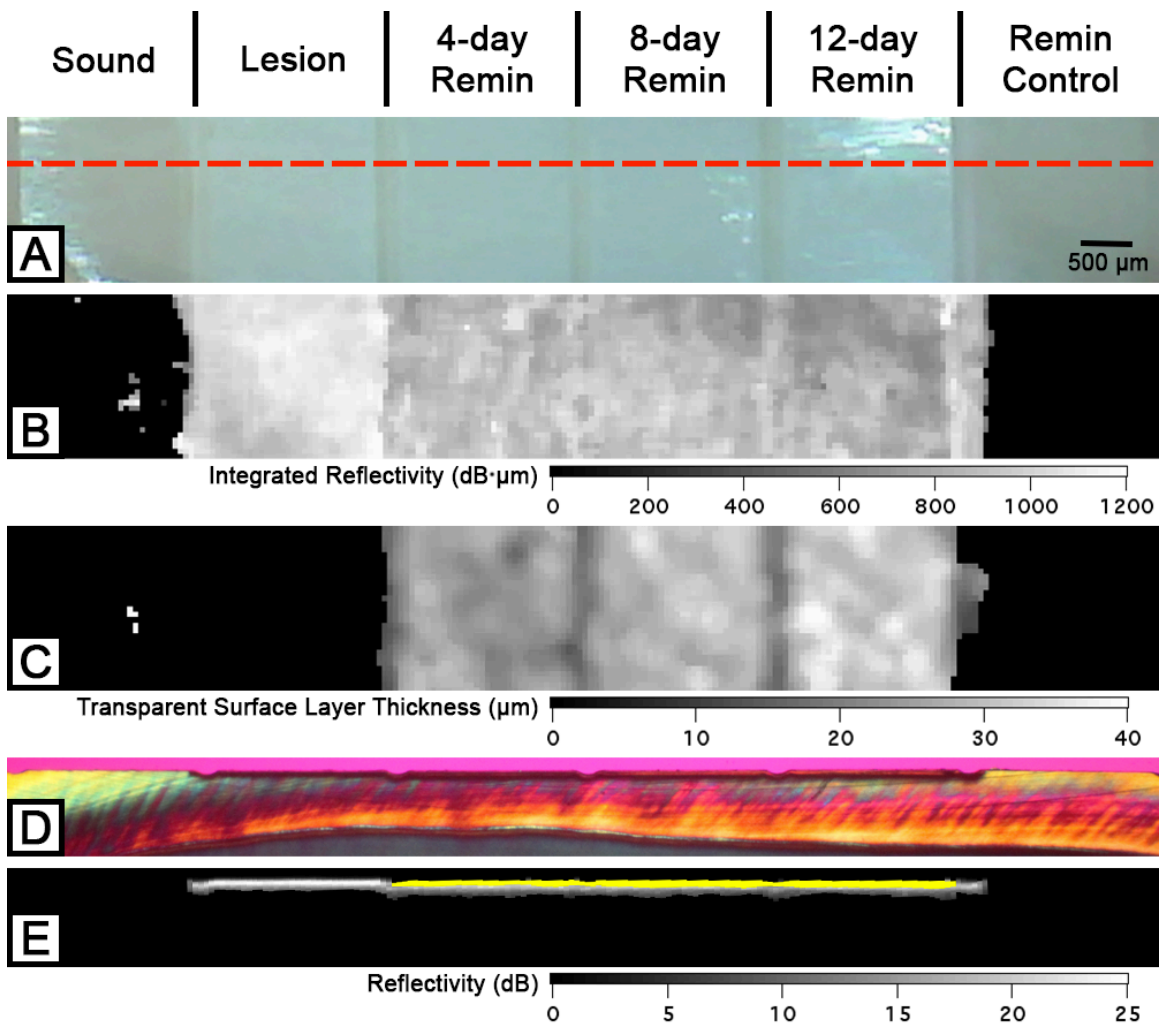


Figure 4.2 Two-dimensional projection and cross-sectional PLM and OCT images of the six windows on a 24-h demineralization sample. The red dotted line in the visible light reflectance image (A) represents the position of the section shown in (D) and (E). Two-dimensional OCT surface projection images of the same sample are shown including (B) integrated reflectivity and (C) the transparent surface layer thickness. PLM (D) and processed CP-OCT B-scan (E) images show an increase in transparent surface layer thickness over the periods of exposure to the remineralizing solution. The transparent surface layer is highlighted in yellow (E).

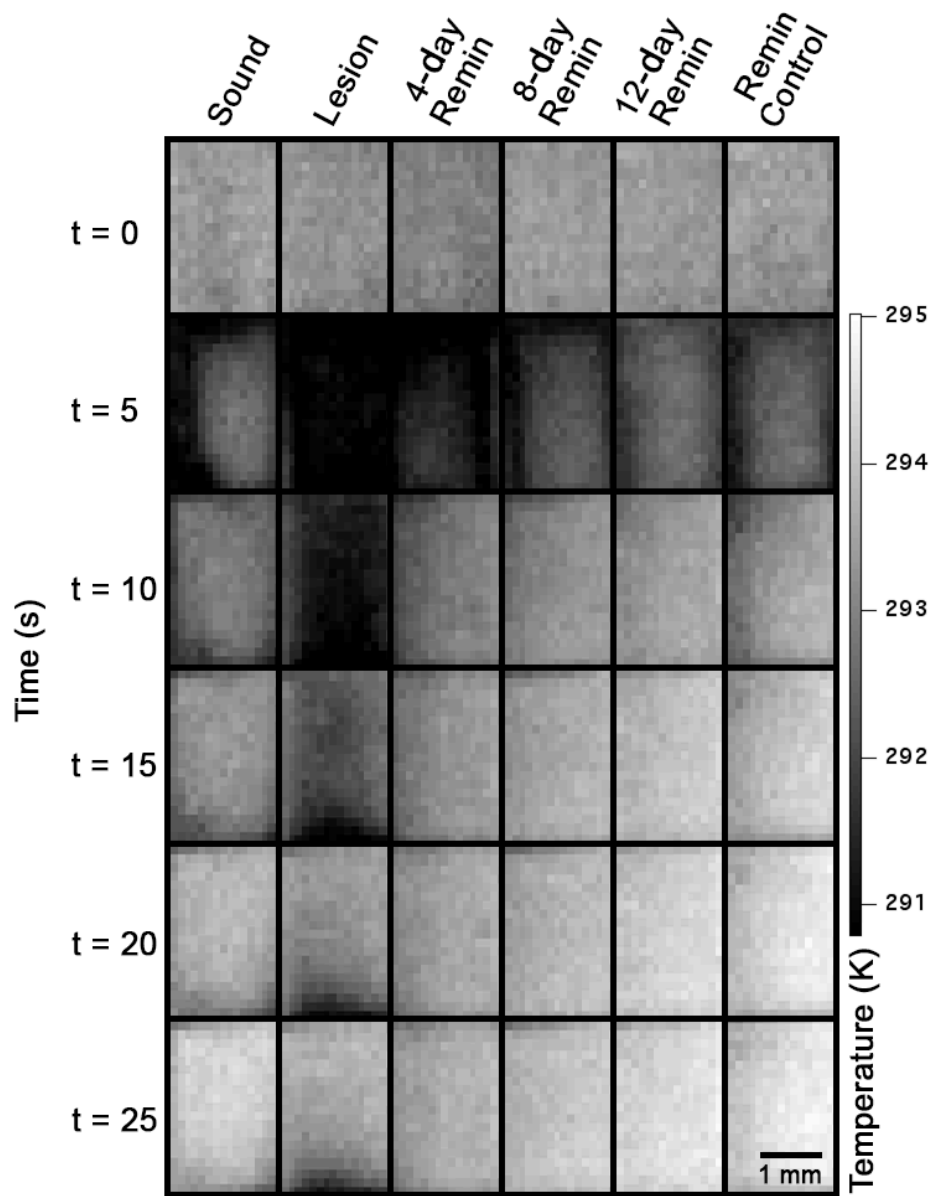


Figure 4.3 Time-lapse thermal images of the sample shown in **Fig. 4.2**. Time axis on left represents time elapsed after turning on the air nozzle.

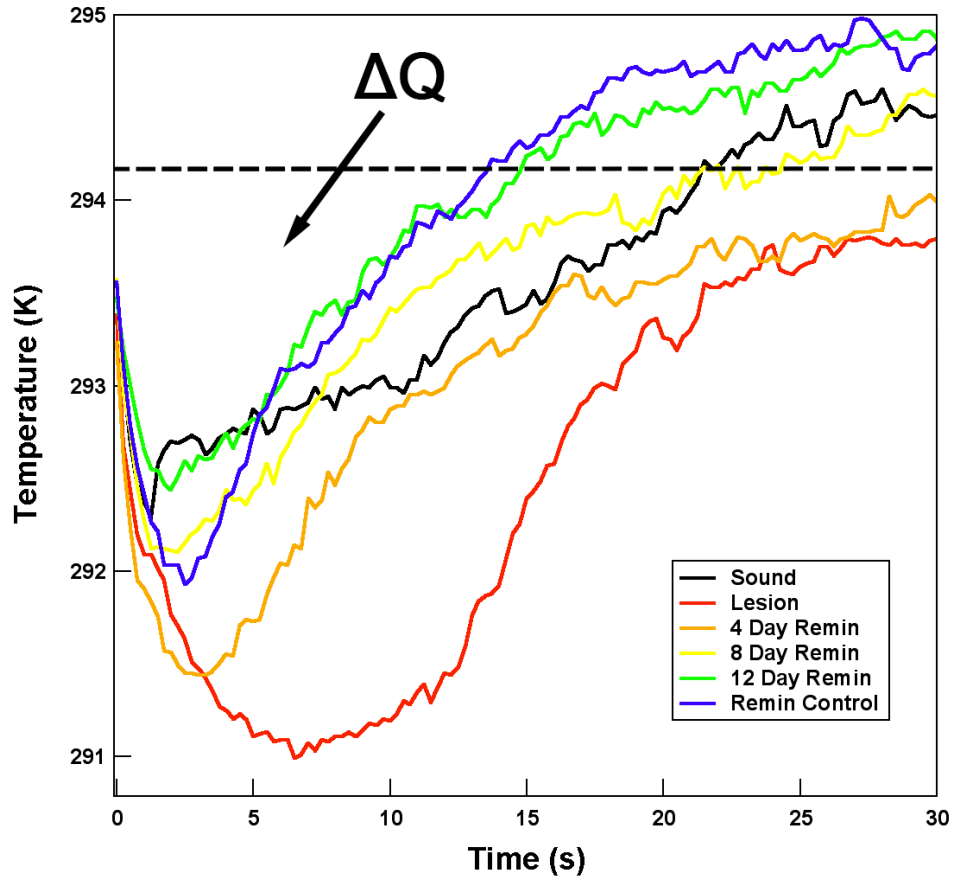


Figure 4.4 Typical time–temperature profiles over 30s of the sample shown in **Fig. 4.2**. ΔQ is the area enclosed by the dotted line representing the ambient temperature and the time–temperature curve.

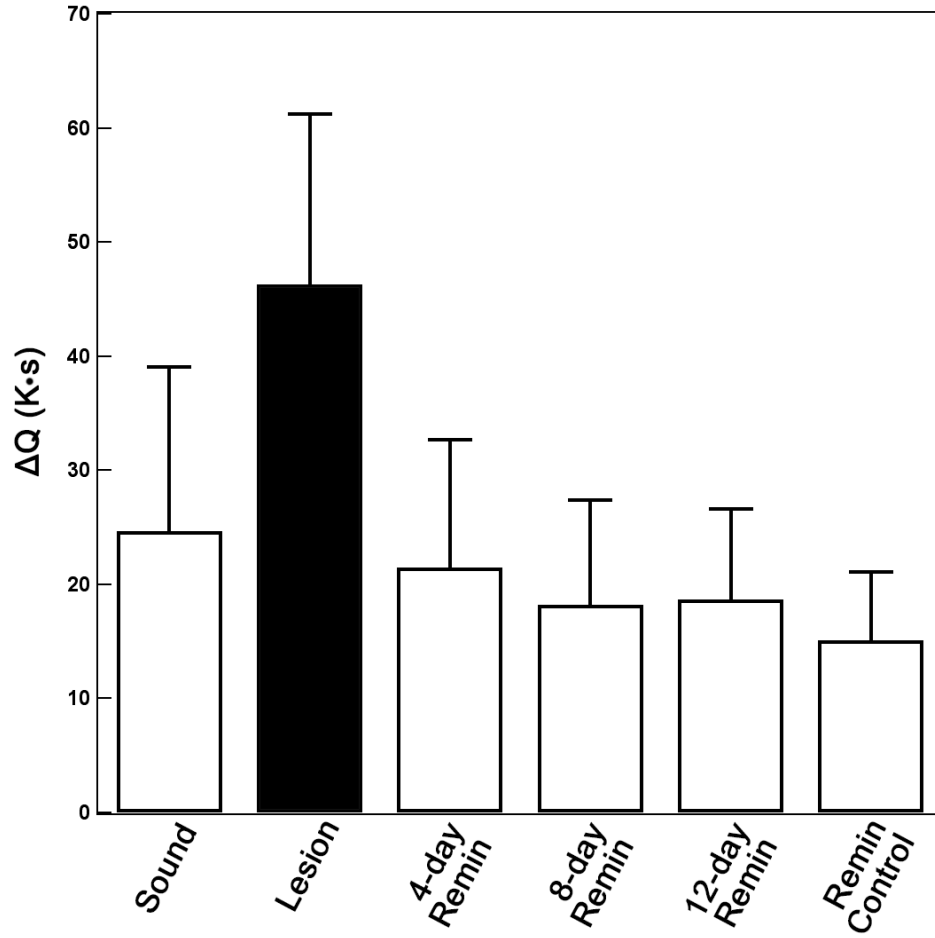


Figure 4.5 Mean \pm S.D. ΔQ measurements of the 24-h demineralization samples.

Bars not sharing any common colors were significantly different, $P < 0.05$ ($n = 15$).

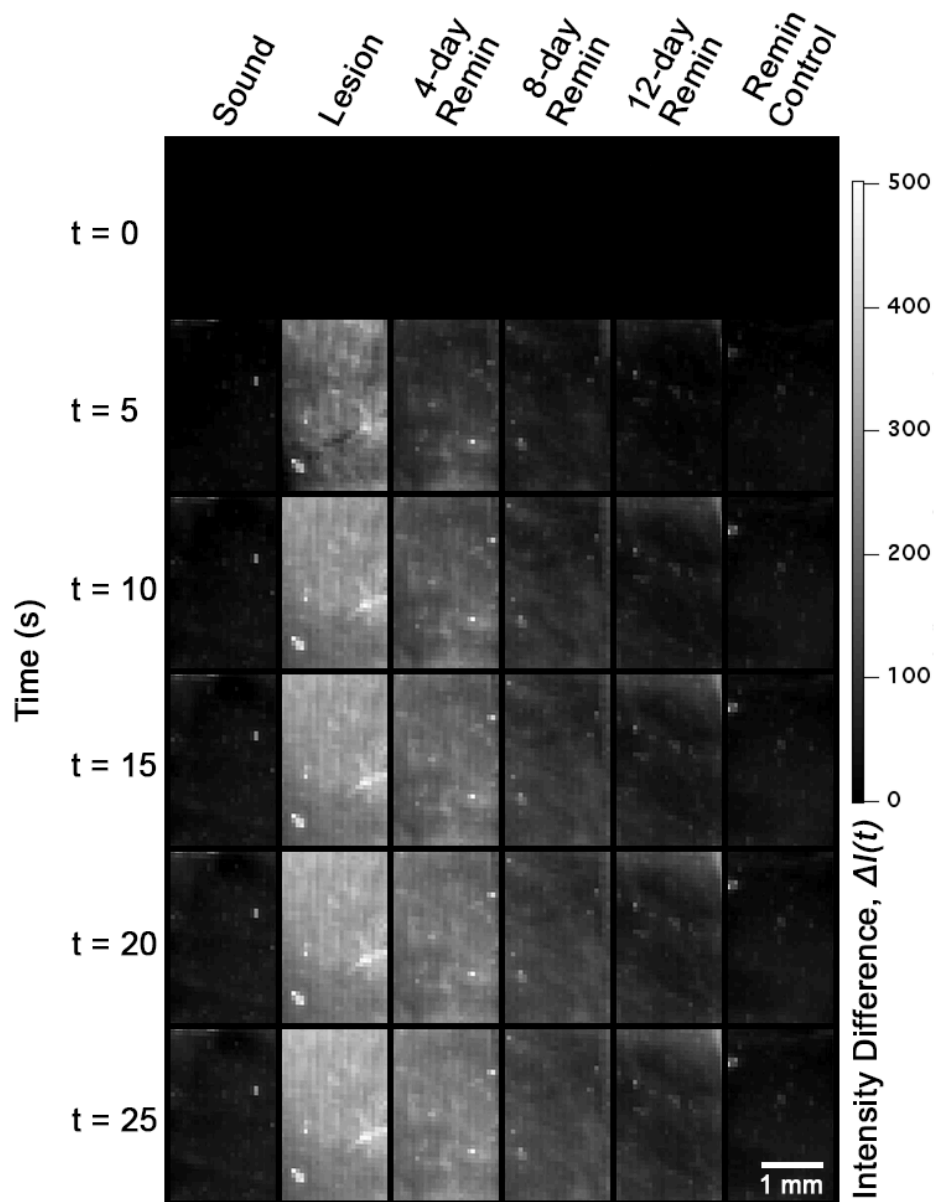


Figure 4.6 Time-lapse NIR reflectance images with a 1460 nm band-pass filter of the sample shown in **Fig. 4.2**. Time axis on left represents time elapsed after turning on the air nozzle.

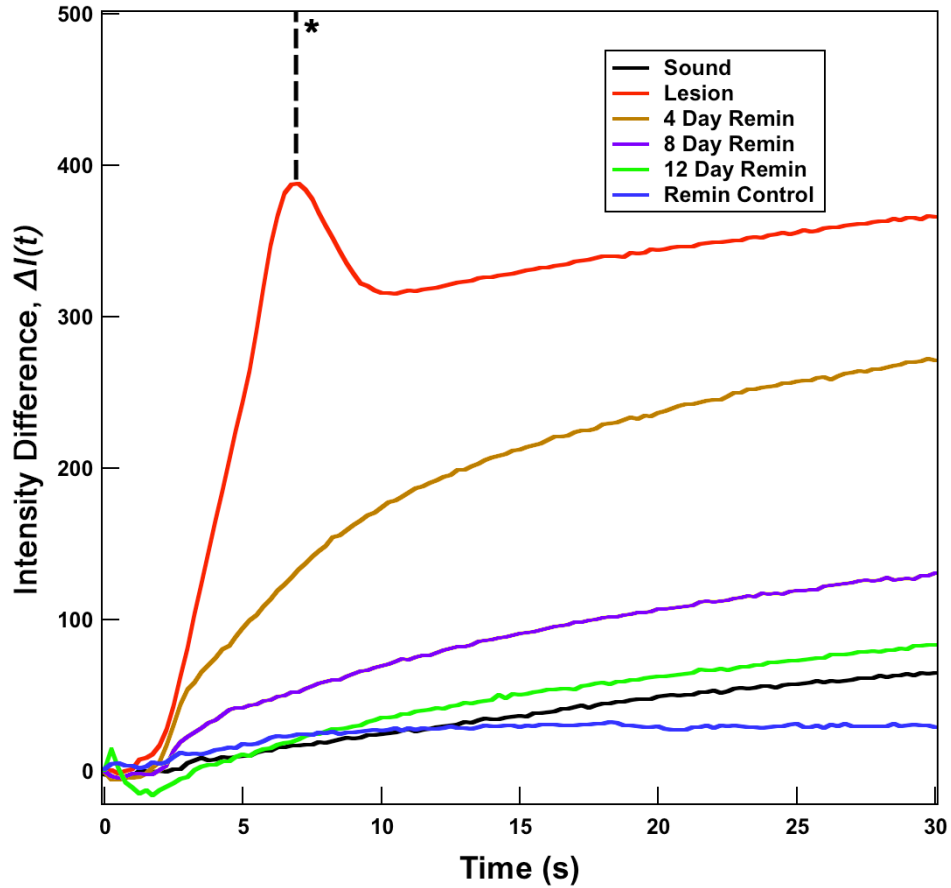


Figure 4.7 Typical time-NIR reflectance intensity difference profiles over 30s of the sample shown in **Fig. 4.2** when the 1460 nm band-pass filter was used. The time-intensity difference curve was cropped up to the dotted line* for curve fitting to the sigmoid function if the window exhibited a sudden excursion in intensity as shown in the lesion window (red).

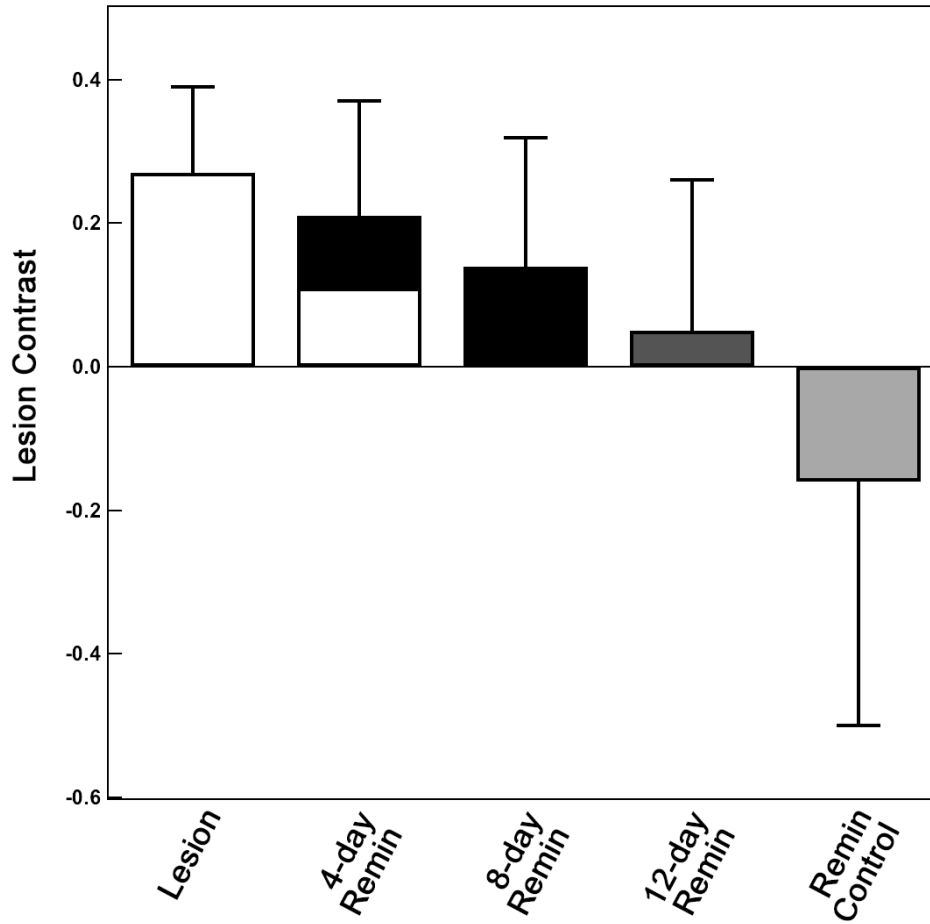


Figure 4.8 Mean \pm S.D. lesion contrast measurements of the 24-h demineralization samples. Bars not sharing any common colors were significantly different, $P < 0.05$ ($n = 15$).

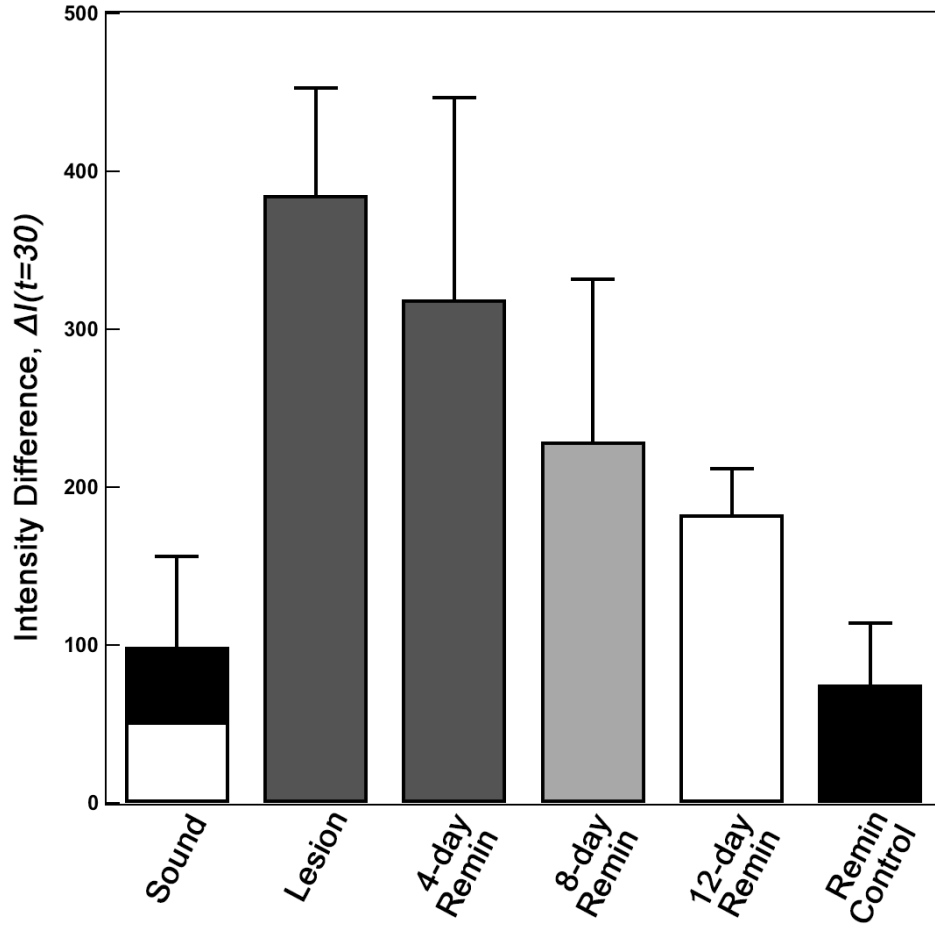


Figure 4.9 Mean \pm S.D. intensity differences at $t = 30s$ of the 24-h demineralization samples. Bars not sharing any common colors were significantly different, $P < 0.05$ ($n = 15$).

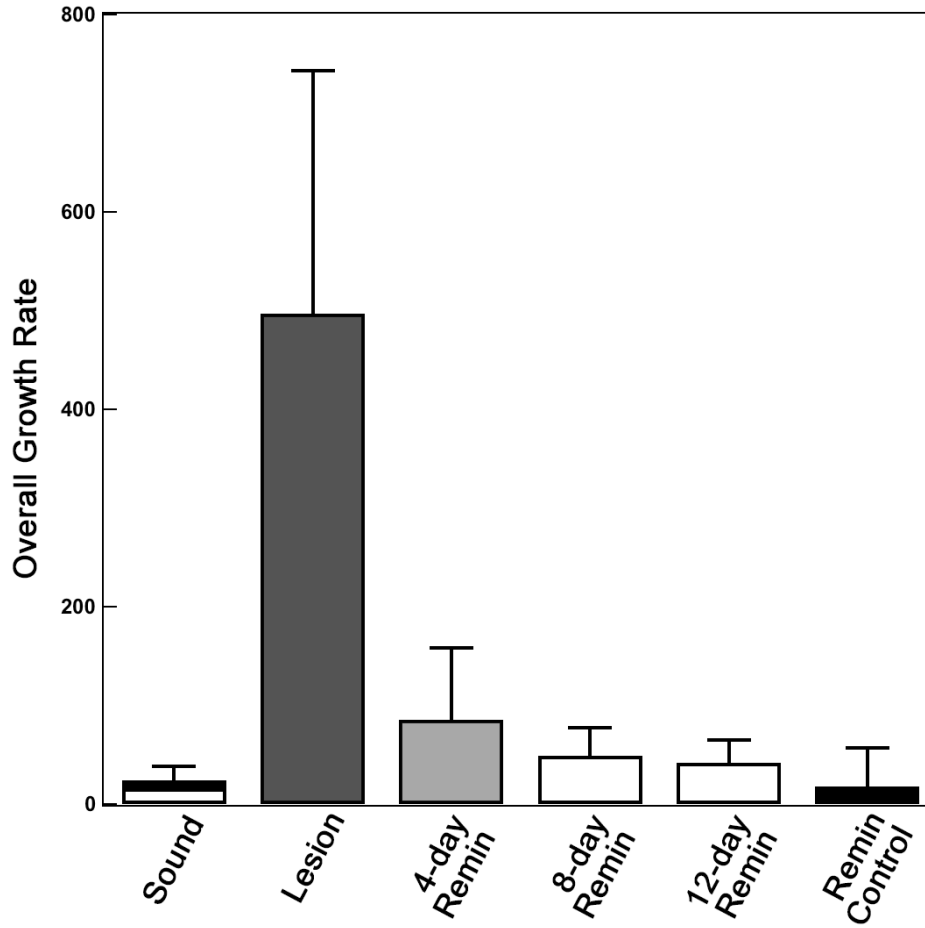


Figure 4.10 Mean \pm S.D. OGR values acquired from the curve fitting of the 24-h demineralization samples. Bars not sharing any common colors were significantly different, $P < 0.05$ ($n = 15$).

4.8 REFERENCES

- Ando, M., Sharp, N. and Adams, D. (2012). Pulse thermography for quantitative nondestructive evaluation of sound, de-mineralized and re-mineralized enamel. *Proc. SPIE Health Monitoring of Structural and Biological Systems I*, San Diego, CA, **8348**: S1-7.
- Ando, M., Stookey, G. K. and Zero, D. T. (2006). Ability of quantitative light-induced fluorescence (QLF) to assess the activity of white spot lesions during dehydration. *Am. J. Dent.*, **19**(1): 15-18.
- Arends, J., Ruben, J. L. and Inaba, D. (1997). Major topics in quantitative microradiography of enamel and dentin: R parameter, mineral distribution visualization, and hyper-remineralization. *Adv. Dent. Res.*, **11**(4): 403-414.
- Atkinson, H. F. (1947). An investigation into the permeability of human enamel using osmotic methods. *Br. Dent. J.*, **83**(10): 205-214.
- Baumgartner, A., Dicht S., Hitzenberger, C. K., Sattmann, H., Robi, B., Moritz, A., Sperr, W. and Fercher, A. F. (2000). Polarization-sensitive optical coherence tomography of dental structures. *Caries Res.*, **34**: 59-69.
- Bush, J., Davis, P. and Marcus, M. A. (2000). All-fiber optic coherence domain interferometric techniques. *Proc. SPIE Fiber Optic Sensor Technology II*, San Jose, CA, **4204**: 71-80.
- Chung, S., Fried, D., Staninec, M. and Darling, C. L. (2011). Multispectral near-IR reflectance and transillumination imaging of teeth. *Biomed. Opt. Express*, **2**(10): 2804-2814.
- Darling, C. L., Featherstone, J. D. B., Le, C. Q. and Fried, D. (2009). An automated digital microradiography system for assessing tooth demineralization. *Proc. SPIE Lasers in Dentistry VX*, San Jose, CA, **7162**: T1-7.
- Darling, C. L., Huynh, G. D. and Fried, D. (2006). Light scattering properties of natural and artificially demineralized dental enamel at 1310 nm. *J. Biomed. Opt.*, **11**(3): 34023.
- Ekstrand, K. R., Zero, D. T., Martignon, S. and Pitts, N. B. (2009). Lesion activity assessment. *Monogr. Oral Sci.*, **21**: 63-90.
- Fejerskov, O. and Kidd, E., Eds. (2003). Dental caries: the disease and its clinical management. Oxford, Blackwell.
- Fried, D., Xie, J., Shafi, S., Featherstone, J. D. B., Breunig, T. M. and Le, C. Q. (2002). Early detection of dental caries and lesion progression with polarization sensitive optical coherence tomography. *J. Biomed. Opt.*, **7**(4): 618-627.

- Fried, W. A., Darling, C. L., Chan, K. and Fried, D. (2013). High contrast reflectance imaging of simulated lesions on tooth occlusal surfaces at near-IR wavelengths. *Lasers Surg. Med.*, **45**(8): 533-541.
- Jones, R. S., Darling, C. L., Featherstone, J. D. B. and Fried, D. (2006). Imaging artificial caries on the occlusal surfaces with polarization-sensitive optical coherence tomography. *Caries Res.*, **40**(2): 81-89.
- Jones, R. S., Darling, C. L., Featherstone, J. D. B. and Fried, D. (2006). Remineralization of in vitro dental caries assessed with polarization sensitive optical coherence tomography. *J. Biomed Opt.*, **11**(1): 014016
- Kaneko, K., Matsuyama, K. and Nakashima, S. (1999). Quantification of early carious enamel lesions by using an infrared camera. *Proc. the 4th Annual Indiana Conference: Early Detection of dental caries II*, Indianapolis, IN, 83-99.
- Kang, H., Jiao, J. J., Lee, C., Le, M. H., Darling, C. L. and Fried, D. L. (2010). Nondestructive assessment of early tooth demineralization using cross-polarization optical coherence tomography. *IEEE J. Sel. Top. Quantum Electron*, **16**(4): 870-876.
- Kidd, E. A. (1983). The histopathology of enamel caries in young and old permanent teeth. *Br. Dent. J.*, **155**(6): 196-198.
- Lee, D., Fried, D. and Darling, C. (2009). Near-IR multi-modal imaging of natural occlusal lesions. *Proc. SPIE Lasers in Dentistry XV*, San Jose, CA, **7162**: X1-7.
- Lee, R. C., Darling, C. L. and Fried, D. (2014). Automated detection of remineralization in simulated enamel lesions with PS-OCT. *SPIE Lasers in Dentistry XX*, San Jose, CA, **8929**: E1-8
- Lee, R. C., Kang, H., Darling, C. L. and Fried, D. (2014). Automated assessment of the remineralization of artificial enamel lesions with polarization-sensitive optical coherence tomography. *Biomed. Opt. Express*, **5**(9): 2950-2962.
- Lepri, T. P., Colucci, V., Turssi, C. P. and Corona, S. A. (2013). Permeability of eroded enamel following application of different fluoride gels and CO2 laser. *Lasers Med. Sci.*, **28**(1): 235-240.
- Lin, M., Liu, Q. D., Xu, F., Bai, B. F. and Lu, T. J. (2009). In vitro investigation of heat transfer in human tooth. *Proc. SPIE Experimental Mechanics IV*, Singapore, Singapore, **7522**: N1-7.
- Manesh, S. K., Darling, C. L. and Fried, D. (2009). Polarization-sensitive optical coherence tomography for the nondestructive assessment of the remineralization of dentin. *J. Biomed. Opt.*, **14**(4): 044002.

Maung, L. H., Lee, C. and Fried, D. (2010). Near-IR Imaging of thermal changes in enamel during laser ablation. *SPIE Lasers in Dentistry XVI*, San Jose, CA, **7549**: 21-26.

Myers, H. M. (1965). Trapped water of dental enamel. *Nature*, **206**(985): 713-714.

Ngotheppitak, P., Darling, C. L. and Fried, D. (2005). Measurement of the severity of natural smooth surface (interproximal) caries lesions with polarization sensitive optical coherence tomography. *Lasers Surg. Med.*, **37**(1): 78-88.

NIH (2001). Diagnosis and management of dental caries throughout life, *NIH Consensus Statement*, **18**: 1-24.

Petersen, P. E. (2003). The world oral health report 2003: continuous improvement of oral health in the 21st century--the approach of the WHO global oral health programme. *Community Dent. Oral. Epidemiol.*, **31**: 3-23.

Simon, J. C., Chan, K. H., Darling, C. L. and Fried, D. (2014). Multispectral near-IR reflectance imaging of simulated early occlusal lesions: Variation of lesion contrast with lesion depth and severity. *Lasers Surg. Med.*, **46**(3): 203-215.

ten Cate, J. M. and Arends, J. (1977). Remineralization of artificial enamel lesions in vitro. *Caries Res.*, **11**(5): 277-286.

ten Cate, J. M. and Featherstone, J. D. B. (1991). Mechanistic aspects of the interactions between fluoride and dental enamel. *Crit. Rev. Oral Biol. Med.*, **2**: 283-296.

Usenik, P., Bürmen, M., Fidler, A., Pernuš, F. and Likar, B. (2014). Near-infrared hyperspectral imaging of water evaporation dynamics for early detection of incipient caries. *J. Dent.*, **42**(10):1242-1247.

Weatherell, J. A. (1975). Composition of dental enamel. *Br. Med. Bull.* **31**(2): 115-119.

WHO. (1994). Fluorides and oral health. Report of a WHO expert committee on oral health status and fluoride use. *World Health Organ. Tech. Rep. Ser.*, **846**: 1-37.

Wu, J. and Fried, D. (2009). High contrast near-infrared polarized reflectance images of demineralization on tooth buccal and occlusal surfaces at $\lambda = 1310\text{-nm}$. *Lasers Surg. Med.*, **41**(3): 208-213.

Yamazaki, H. and Margolis, H. C. (2008). Enhanced enamel remineralization under acidic conditions in vitro. *J. Dent. Res.*, **87**(6): 569-574.

Zahradnik, R. T. and Moreno, E. C. (1977). Progressive stages of subsurface demineralization of human tooth enamel. *Arch. Oral. Biol.*, **22**(10-11): 585-591.

Zakian, C., Pretty, I. and Ellwood, R. (2009). Near-infrared hyperspectral imaging of teeth for dental caries detection. *J. Biomed. Opt.*, **14**(6): 064047.

Zakian, C. M., Taylor, A. M., Ellwood, R. P. and Pretty, I. A. (2010). Occlusal caries detection by using thermal imaging. *J. Dent.*, **38**(10): 788-795.

Zhang, X. Z., Anderson, P., Dowker, S. E. and Elliott, J. C. (2000). Optical profilometric study of changes in surface roughness of enamel during in vitro demineralization. *Caries Res.*, **34**(2): 164-174.

CHAPTER V

INFRARED METHODS FOR ASSESSMENT OF THE ACTIVITY OF NATURAL ENAMEL CARIES LESIONS

5.1 SUMMARY

New diagnostic methods are needed for the accurate assessment of caries lesion activity to establish the need for surgical treatment. Detection of the highly mineralized surface layer that forms near the surface of the lesions as a result of remineralization is important for diagnosis of the lesion activity. Previous studies have demonstrated that novel imaging methods can be used to detect remineralization of artificial enamel caries lesions. In this chapter, the activity of natural enamel caries lesions was assessed in-vitro via detection of the surface layer with PS-OCT and dehydration rate measurements with NIR reflectance and thermal imaging modalities. An automated approach for detecting the surface layer with PS-OCT yielded high sensitivity (= 0.79) and high specificity (= 0.93) with moderate correlation ($R^2 = 0.5920$) with histology. Significant differences in dehydration rate measurements were found between the active and the arrested lesions using both the NIR reflectance and thermal imaging modalities. These results demonstrate that these novel imaging methods are ideally suited for nondestructive, noninvasive and quantitative measurement of lesion activity during a single clinical examination in real-time.

5.2 INTRODUCTION

New diagnostic methods are needed for the accurate assessment of caries lesion activity to establish the need for surgical treatment. It is well known that remineralization therapy via fluoride produces fluorapatite crystals that are much more resistant to acid challenge than the original hydroxyapatite of tooth enamel and dentin (Kidd and

Joyston-Bechal 1997). With a thick enough fluorapatite-rich surface layer, diffusion of calcium and phosphate ions at the lesion body, can be dramatically reduced (ten Cate and Arends 1977, Kidd 1983, ten Cate and Featherstone 1991). This leads to the arrest of lesion progression and no further intervention is necessary. The surface layer of a lesion is important for diagnosis of the current “state of the lesion”, i.e., whether or not the caries lesion is active and expanding or whether the lesion has been arrested and is undergoing remineralization. Therefore, one cannot overstate the importance of accurate diagnosis of the lesion activity in its early stage of development at which point non-invasive preventive measures can be taken to halt further decay. It is advantageous to assess lesion activity using a nondestructive, noninvasive and quantitative method during a single clinical examination.

Current methods for lesion assessment are composed of a combination of visual and tactile exams, which are prone to subjective bias, interference from staining, are limited to exposed surfaces and there is the potential for permanent damage to the intact lesion surface layer from sharp instruments (NIH 2001, Ekstrand et al. 2009). In addition, the remineralized caries lesion still retains the white coloration due to the subsurface demineralization, which may lead to an inconclusive diagnosis of caries lesion activity (Ekstrand et al. 2009). The histological analyses for lesion assessment such as transverse microradiography (TMR) and polarized light microscopy (PLM) require destruction of the tooth, making both methods unsuitable for use *in-vivo*. Ekstrand et al. reported that it is extremely difficult to differentiate active lesions from inactive lesions in a single clinical examination without training or calibration (Ekstrand et al. 2005). Clinical criteria for caries lesion activity has been introduced by Nyvad et al.

and incorporated by the ICDAS II caries classification system, but both also utilize visual-tactile examination (Nyvad et al. 1999, Banting et al. 2005). At advanced stages of caries, the surface of the lesion becomes further demineralized chalky white surface due to irregular surface erosion and cavitation (Thylstrup et al. 1994, Nyvad et al. 1999). The arrested caries lesions exhibit a glossy appearance with a surface hardness that is comparable to sound enamel because they have a highly mineralized surface layer on the outer surface of the lesion (Thylstrup et al. 1994, Nyvad et al. 1999, Ekstrand et al. 2005). Differences in surface porosity between arrested and active caries lesions may be discriminated using novel optical imaging methods.

Since optical diagnostic tools exploit changes in the light scattering of the lesion, they have great potential for the diagnosis of lesion activity. Optical coherence tomography (OCT) is a non-invasive technique for creating cross-sectional images of internal biological structures. Several studies both *in-vitro* and *in-vivo* have demonstrated that polarization-sensitive OCT (PS-OCT) is uniquely capable of this task since it provides a measurement of the reflectivity from each layer of the lesion and is able to show the formation of a zone of increased mineral density and reduced light scattering due to remineralization (Amaechi et al. 2001, Fried et al. 2002, Jones et al. 2006, Louie et al. 2010). Polarization sensitivity is particularly valuable for resolving the structure of early caries lesions because caries lesions strongly scatter incident polarized light and the image in the cross-polarization axis to that of the incident polarization can provide improved lesion contrast. We have demonstrated in several studies that the lesion severity can be represented by the integrated reflectivity with depth in the CP-OCT image and the integrated reflectivity, ΔR , is analogous to the

integrated mineral loss, ΔZ , obtained from TMR (Arends et al. 1997, Ngaotheppitak et al. 2005, Jones et al. 2006, Chong et al. 2007). The presence of a surface zone of reduced light scattering in the OCT image may indicate the lesion is arrested. PS-OCT images are particularly valuable for resolving these highly mineralized surface layers since the image in the incident polarization shows the position of the tooth surface while the image in the cross-polarization shows the body of the subsurface lesion.

Recently, swept-source OCT (SS-OCT) systems have been introduced that are capable of operating at very high scan rates without a marked loss in the signal to noise ratio. Previous studies have shown that the high quality OCT images of caries lesions can be acquired using SS-OCT systems (Shimada et al. 2010, Natsume et al. 2011, Nee et al. 2014). A combination of PS-OCT with SS-OCT (PS-SS-OCT) would allow rapid acquisition of high-resolution tomographic images in a clinical setting.

In a previous PS-OCT study, we developed approaches to automatically detect the surface layer and measure its thickness with high accuracy in artificial enamel caries lesions (Lee et al. 2014). Accurate detection and measurement of the transparent surface layer can provide extremely useful information about lesion activity. In this chapter, we evaluate whether PS-OCT coupled with the automated algorithm can be used to nondestructively measure these changes in the structure of natural occlusal and smooth surface enamel caries lesions.

As the lesion becomes arrested or undergoes remineralization, the permeability of the surface layer significantly decreases and the rate of water dehydration from the lesion depends on the lesion structure. The optical changes with water loss have been exploited via quantitative light-induced fluorescence (QLF), thermal imaging and near-

infrared (NIR) imaging (Kaneko et al. 1999, Ando et al. 2006, Zakian et al. 2010, Usenik et al. 2014). Kaneko et al. and Zakian et al. carried out caries detection studies with a thermal camera and an air-jet for evaporation on occlusal and smooth natural tooth surfaces (Kaneko et al. 1999, Zakian et al. 2010). The endothermic behavior of the water evaporation causes a temperature decrease followed by a recovery to thermal equilibrium as the lesion becomes dry. Ando et al. reported that pulsed thermography is sensitive to the mineralization state of the tooth and has potential to be used for lesion activity assessment (Ando et al. 2012). NIR imaging has also been exploited for caries detection since sound enamel is transparent in the NIR and the scattering coefficient increases exponentially with increasing mineral loss. Recent studies on NIR reflectance imaging with wavelengths coincident with high water absorption, at 1460 nm and beyond 1500 nm, demonstrated high lesion contrast for artificial and natural enamel caries lesions (Chung et al. 2011, Fried et al. 2013, Simon et al. 2014). This suggests that changes in water content have a more profound effect on enamel transparency at NIR wavelengths than in the visible. In a previous study, we demonstrated that rate of water evaporation from artificial enamel lesions could be imaged with thermal and NIR reflectance imaging (Lee et al. 2015). We also reported that the NIR reflectance imaging at wavelengths between 1400 nm and 1700 nm was capable of detecting significant differences between different periods of remineralization in artificial enamel lesions during the dehydration process (Lee et al. 2015). The influence of hydration on enamel lesions can be investigated as an indirect indicator of the decreased permeability of water due to remineralization. In this chapter, we test the hypothesis that the thermal and NIR reflectance imaging methods can be used to selectively and accurately

discriminate active natural enamel caries lesions from arrested natural enamel caries lesions and ultimately determine the caries lesion activity during the dehydration process.

5.3 MATERIALS AND METHODS

5.3.1 Sample Selection and Examination

Teeth extracted from patients in the San Francisco Bay area were collected, cleaned and sterilized with Gamma radiation. Sixty teeth with suspected enamel caries lesions were selected; lesions were identified as white or brown/black (pigmented spots) on the tooth surface. The teeth with an obvious cavitation to dentin and calculus were excluded from the experiment. The roots were cut off and the coronal portions of teeth were mounted on 1.2 cm x 1.2 cm x 3 cm delrin blocks.

Prior to the experiment, two clinicians that had been extensively trained and calibrated through practical exercises independently examined the teeth with 2.5x magnifying surgical loupes and a ball ended periodontal probe to gently check for loss of tooth structure and surface texture without damaging the tooth structure. Teeth were scored according to both the ICDAS II lesion classification and the ICDAS II lesion activity assessment criteria (Banting et al. 2005). A total of 42 teeth were mutually classified with ICDAS II scores of 1, 2 and 3 by the two examiners and there were 22 smooth surface and 20 occlusal pits and fissure caries lesions. The two examiners subsequently used the ICDAS II lesion activity assessment criteria for determining the activity of the suspected lesions; the ICDAS II lesion activity assessment criteria utilizes

color (white-black), luster (dull-shiny) and texture (smooth-rough) before and after 5 seconds of air-drying (Banting et al. 2005).

5.3.2 PS-OCT System

The PS-OCT system used in this work has been described previously (Fried et al. 2002). An all fiber-based Optical Coherence Domain Reflectometry (OCDR) system with polarization maintaining (PM) optical fiber, high speed piezoelectric fiber-stretchers and two balanced InGaAs receivers that was designed and fabricated by Optiphase, Inc., Van Nuys, CA was used to acquire the images (Bush et al. 2000). This two-channel system was integrated with a broadband superluminescent diode (SLD) DL-CS3159A, Denselight (Jessup, MD) and a high-speed XY-scanning motion controller system, ESP 300 controller with ILS100PP and 850G-HS stages, (Newport, Irvine, CA) for *in-vitro* optical tomography. A high power (15 mW) polarized SLD source operated at a center wavelength of 1317 nm with a spectral bandwidth full-width-half-maximum (FWHM) of 84 nm was used to provide an axial resolution of 9 μm in air and 6 μm in enamel (refractive index = 1.6). Light from the sample arm was focused onto the sample surface using a 20 mm focal length plano-convex lens providing a lateral resolution of approximately 20 μm .

The PS-OCT system was completely controlled using LabViewTM software (National Instruments, Austin, TX). Samples were dried with pressurized air for 30 seconds prior to scanning. The A-scan sweep rate was 150 Hz with a dynamic range of 48 dB. Each A-scan was an average of 10 raw A-scans and was spaced 50 μm apart. The total number of data points in each A-scan was 2000 over a scan range of

approximately 5 mm in air.

5.3.3 Calculation of Transparent Surface Layer Thickness, Lesion Depth and Integrated Reflectivity (ΔR)

PS-OCT images were processed using a dedicated program constructed with LabView™ software. There was a phase shift in the PM-fiber between the two axes, so an axial position calibration was performed once prior to the experiment. A gold mirror was scanned at a 150 Hz sweep rate and each A-scan was an average of 100 scans. Five hundred A-scans were acquired at 10 μm intervals over the entire scan range to determine the required axial position adjustments and the axial position of the cross-polarization scan images was adjusted to match the co-polarization scan images.

The position of the strong surface reflection in the co-polarization axis and the strong scattering of polarized light from the underlying lesion body in the cross-polarization axis were used to measure the thickness of the transparent surface layer. Surface layer detection and measurement utilized an edge detection technique using the zero-crossing first-order derivative as described previously (Lee et al. 2014, Lee et al. 2014). Binary images were generated to indicate either the presence or absence of the transparent surface layer and a 5x5 morphological closing operation with a 50% threshold was subsequently applied to the binary images in order to reduce false-negatives (Lee et al. 2014). Pixels were converted to microns in enamel using a refractive index correction of 1.6 to yield the final transparent surface layer thickness.

The lesion depth was calculated using a previously developed algorithm (Lee et al. 2014). An edge locator was used to make two passes along each A-scan of the

processed CP-OCT images to locate the respective positions at which the intensity has decreased to half of the lesion peak maximum. A linear relationship was established between the lesion depth using PS-OCT and the histological lesion depths measured using polarized light microscopy (PLM) (Chan et al. 2013, Lee et al. 2014).

Previous studies have shown that the integrated reflectivity, ΔR , over the estimated lesion depth positively correlates with the integrated mineral loss (volume percent mineral loss $\times \mu\text{m}$), ΔZ (Ngaotheppitak et al. 2005, Jones et al. 2006). ΔR was calculated by integrating from the base of the transparent layer through the entire estimated lesion body in the CP-OCT images (Lee et al. 2014). This had the added advantage of removing the contribution of the high specular reflection at the surface of the transparent layer, which was large enough to be present even in the CP-OCT images. A 5×5 pixel median filter was applied to the final 2D projection images for improved visualization.

5.3.4 Dehydration Measurements

The following setup was used for the dehydration experiments of sections 5.3.5 and 5.3.6. Each sample was placed in a mount connected to a high-speed XY-scanning motion controller system, Newport ESP 300 controller & 850G-HS stages coupled with air nozzles connected together to a compressed air and a light source (Lee et al. 2015). Each sample was immersed in the water bath for 60 seconds while being vigorously shaken to enhance water diffusion. After the sample was removed from the water bath, the excess water on the surface of the lesion with a disposable cotton roll. An image was captured as an initial reference image and the air spray was activated. Seven air

nozzles were positioned 5 cm away from sample and the air pressure was set to 12 psi. Each measurement consisted of capturing a sequence of images at 4 frames per second for 60 seconds. The air nozzles and the light source were centered on the suspected lesion. The dehydration setup was completely automated using LabView™.

5.3.5 Thermal Imaging and Analysis

A Model A65 infrared (IR) thermography camera (FLIR Systems, Wilsonville, OR) sensitive from 7.5 - 13 μm with a resolution of 640 x 512 pixels, a thermal sensitivity of 50 mK and a lens with a 13 mm focal length was used to record temperature changes during the dehydration process. The area per pixel was approximately 0.02 mm^2 . The ambient room temperature, flowing air temperature and water bath temperature were approximately 21 °C (294.15 K) and were consistent throughout the experiment. The object emissivity was set to 0.91, and the atmospheric temperature was set to 294.15 K (Lin et al. 2009). Relative humidity was set at a default value of 50%; humidity values were not recorded, but every sample was measured under the same conditions. Previous studies have shown that ΔQ , the area enclosed by the time-temperature curve, can be used as a quantitative measure of porosity and can be used to discriminate between sound and demineralized enamel *in-vitro* (Kaneko et al. 1999).

Thermal images were processed and analyzed using a dedicated program written in Labview™. The thermography camera outputs a series of temperature measurements over time. The initial reference temperature measurements varied slightly (± 0.5 K) due to variations in emissivity, lesion structure, mineral composition and water content among windows. Calibration was carried out via matching the

measurements from the initial reference image to the ambient temperature. ΔQ was calculated from the area enclosed by the initial temperature and the time-temperature curve.

5.3.6 NIR Reflectance Imaging and Analysis

An Indigo Alpha NIR camera (FLIR Systems, Wilsonville, OR) with an InGaAs focal plane array, a spectral sensitivity range from 900 nm to 1750 nm, a resolution of 320 x 256 pixels and an InfiniMite™ lens (Infinity, Boulder, CO) was used to acquire all the images during the dehydration process. The area per pixel was approximately 0.003 mm². Light from a 150 W fiber-optic illuminator FOI-1 (E Licht Company, Denver, CO) was directed at the sample with crossed polarizers and a long-pass filter at 1400 nm (1400 – 1700 nm). Source to sample distance was fixed at 5 cm for all samples.

NIR reflectance images were processed and automatically analyzed using a dedicated program constructed with LabView™ software. The intensity difference between the final and initial images, ΔI , was calculated using $I(t=60) - I_i$, where $I(t=60)$ is the mean intensity at $t = 60$ seconds and I_i is the mean intensity prior to turning on the air nozzle.

In order to investigate the rate of intensity change in conjunction with the overall intensity change, the "S"-shaped time-intensity curve was fit to a sigmoid function previously described in Eq (2) in (Lee et al. 2015), and the overall growth rate (OGR) was calculated.

5.3.7 Polarized Light Microscopy (PLM), Transverse Microradiography (TMR) and Histological Validation of Lesion Activity

After sample imaging was completed, 200 μm thick serial sections were cut using an Isomet 5000 saw (Buehler, IL) for PLM and TMR. PLM was carried out using a Meiji Techno Model RZT microscope (Meiji Techno Co., LTD, Saitama, Japan) with an integrated digital camera, Canon EOS Digital Rebel XT (Canon Inc., Tokyo, Japan). The sample sections were imbibed in water and examined in the brightfield mode with crossed polarizers and a red I plate with 500 nm retardation. PLM images were acquired at 35x magnification and had a resolution of 3264 x 2448 pixels.

A custom built digital microradiography (TMR) system was used to detect the surface zone of the increased mineral content on the tooth sections (Darling et al. 2009). High-resolution microradiographs were taken using Cu K α radiation from a Philips 3100 X-ray generator and a Photonics Science FDI X-ray digital imager, Microphotonics (Allentown, PA). The X-ray digital imager consisted of a 1392 \times 1040 pixel interline CCD directly bonded to a coherent micro fiber-optic coupler that transfers the light from an optimized gadolinium oxysulfide scintillator to the CCD sensor. The pixel resolution was 2.1 μm and the images were acquired at 10 frames per second. A high-speed motion control system with Newport UTM150 and 850G stages and an ESP 300 controller coupled to a video microscopy and a laser targeting system was used for precise positioning of the sample in the field of view of the imaging system.

For the histological validation of the lesion activity, changes in mineral content were measured with PLM and TMR. Arrested caries lesions have a distinct transparent

surface layer with islands of negatively birefringent enamel within the positively birefringent body of the enamel in water (Thylstrup et al. 1994). Irregular surface defects such as cavitation were also recorded. The thickness of transparent surface layer was measured using the image analysis package incorporated in Igor Pro (Wavemetrics, Lake Oswego, OR). If a distinct transparent surface layer was found, the activity of the suspected caries lesion was categorized as “arrested”. If the lesion did not have a transparent surface layer or a discontinuity of the surface layer due to surface irregularities, the lesion activity was categorized as “active”.

5.3.8 Statistical Analysis

Sample groups were compared using analysis of variance (ANOVA) with a Tukey–Kramer post hoc multiple comparison test. Linear regression with Pearson’s correlation was used to examine the relationship between data acquired from PS-OCT and PLM measurements. Performances of the infrared imaging methods were evaluated using receiver operating characteristic (ROC) curves. All statistical analyses were performed with 95% confidence with Prism™ (GraphPad software, San Diego, CA).

5.4 RESULTS

5.4.1 ICDAS II Lesion Activity Assessment

Two examiners relied on the ICDAS II lesion classification criteria for determining the stages of the caries process of the suspected natural caries lesion samples solely to screen teeth for lesion activity assessment. The ICDAS II scores ranged from 0 to 4 and a total of 42 teeth were mutually scored as 1, 2 and 3 by the two examiners. The inter-

examiner agreement for ICDAS II lesion classification criteria was 81%, and kappa values were 0.594 (unweighted) and 0.620 (weighted).

For the activity of the smooth surface enamel caries lesion samples, the inter-examiner agreement was 95%; kappa values were not reported because kappa statistics is not reliable due to its limitations for skewed data sets. With the true-positive being the successful diagnosis of an active lesion based on histological findings, the two examiners yielded an average sensitivity of 0 and an average specificity of 0.97; one examiner diagnosed all lesions as arrested and another examiner diagnosed one lesion as an active lesion. Eighteen of the 22 smooth surface lesion samples exhibited the transparent surface layer with histology and were categorized as arrested caries lesions.

For the activity of the occlusal pits and fissure caries lesion samples, the inter-examiner agreement was 45% with a kappa value of -0.06. The two examiners yielded an average sensitivity of 0.65 and an average specificity of 0.50. Ten of the 20 occlusal pits and fissure lesion samples exhibited a transparent surface layer in the center of pits and fissures with histology and were categorized as arrested caries lesions. Some samples exhibited the transparent surface layer on the smooth surface around pits and fissures but with distinct surface demineralization or micro-cavitation in the pits and fissures. Such samples were categorized as active lesions. When the two data sets were combined and analyzed, the inter-examiner agreement was 71% agreement of diagnoses with a kappa value of 0.32. The two examiners yielded an average sensitivity of 0.46 and an average specificity of 0.80 for all samples.

5.4.2 Infrared Imaging Methods for Lesion Activity Assessment

Arrested and active smooth surface enamel lesions are shown in **Figs. 5.1 and 5.2**,

respectively, with the visible images (**A**), histology with PLM (**B & C**) and results from PS-OCT (**D – F**), thermal (**G**) and NIR reflectance (**H & I**) methods. PLM images of the arrested smooth surface enamel caries lesion (**Figs. 5.1B & 5.1C**) show a thin layer of the transparent surface layer above the subsurface lesion, and PS-OCT was able to estimate the severity and location of the subsurface lesion and accurately estimate the thickness of the transparent surface layer (**Figs. 5.1D – 5.1F**). The active smooth surface enamel caries lesions show microcavitation of the surface without a distinctive surface layer (**Figs. 5.2B & 5.2C**). The thermal imaging (**Figs. 5.1G & 5.2G**) and the NIR reflectance images (**Figs. 5.1H – 5.1I & 5.2H – 5.2I**) show significant differences in ΔQ , ΔI and OGR measurements in the suspected lesion area.

An arrested occlusal pit and fissure caries lesion is shown in **Fig. 5.3** and an active occlusal caries lesion is shown in **Fig. 5.4** with the visible images shown in (**A**), histology with PLM (**B & C**) and results from PS-OCT (**D – F**), thermal (**G**) and NIR reflectance (**H & I**) methods. PLM images of the arrested occlusal lesion (**Figs. 5.3B & 5.3C**) show a thin layer of the transparent surface layer above the subsurface lesion. However, **Fig. 5.4** shows both active and arrested occlusal pits and fissure caries lesions in one sample; **Fig. 5.4B** shows demineralization of the surface structure with cavitation at pits and fissures, and **Fig. 5.4C** shows an arrested pit and fissure lesion with a distinct surface layer. PS-OCT was able to estimate the severity and location of the subsurface lesion and accurately estimate the thickness of the transparent surface layer (**Figs. 5.3D – 5.3F & 5.4D – 5.4F**). The thermal imaging (**Figs. 5.3G & 5.4G**) and the NIR reflectance images (**Figs. 5.3H – 5.3I & 5.4H – 5.4I**) show significant differences in ΔQ , ΔI and OGR measurements in the suspected lesion area.

In our previous study, the automated algorithm for detection and measurement of the transparent surface layer using PS-OCT proved to have high accuracy and high correlation with histology for the artificial enamel caries lesions (Lee et al. 2014). In this work, PS-OCT accurately detected lesions without the transparent surface layer; PS-OCT yielded a sensitivity of 0.75 and a specificity of 0.94 for the smooth surface lesions, a sensitivity of 0.80 and a specificity of 0.90 for the occlusal pits and fissure lesions, and a sensitivity of 0.79 and a specificity of 0.93 for all lesions. For the all true-negative samples ($n = 26$), the thickness of the transparent surface layer estimated with PS-OCT showed a moderate correlation with the thickness measured with PLM as shown in **Fig. 5.5** (Pearson's correlation, $p < 0.0001$, $R^2 = 0.5920$). There was a significant difference in the integrated reflectivity, ΔR , between active and arrested lesion groups of the pits and fissure caries lesion samples, but there was no significant difference between active and arrested lesion groups of the smooth surface caries lesion samples as shown in **Table 5.1**.

It has been shown that the highly mineralized surface layer plays an important role in the dehydration process of remineralized artificial enamel lesions and both the thermal and NIR imaging methods are suitable for detection of remineralization in artificial enamel models (Lee et al. 2015). All three methods, ΔQ , ΔI and OGR, showed a significant reduction in measurements with the presence of transparent surface layer ($P < 0.05$) as shown in **Table 5.1**, and these infrared imaging modalities showed strong performances in accurately diagnosing active lesions as indicated by the area under the curve from the ROC analysis, which are summarized in **Table 5.2**.

5.5 DISCUSSION

Detection of the highly mineralized surface layer that forms near the surface of the lesions as a result of remineralization is critical for the accurate diagnosis of lesion activity. The principal aim of this work was to demonstrate that the rate of water evaporation measured using thermal and NIR reflectance imaging methods could be used to assess the lesion activity of natural enamel caries lesions. A secondary aim was to determine whether the automated transparent surface layer detection algorithm for PS-OCT could accurately detect and measure the thickness of the highly mineralized surface layer in natural enamel caries lesions.

There are significant challenges for the accurate diagnosis of caries lesion activity. Wenzel claimed that lesions confined to enamel might not be evident radiographically until there is approximately 30 – 40 % mineral loss (Wenzel 2008). Thus, radiographs are not suitable in lesion activity assessment of early caries lesions. Clinicians currently rely heavily on visual and tactile examination when a suspected lesion is not evident radiographically. Since conventional methods for diagnosis of lesion activity are highly subjective, rigorous training and calibration are required. Examiners classified most of the smooth surface enamel lesions as arrested lesions and this caused a large discrepancy in sensitivity and specificity. In addition, the inter-examiner reliability was poor for the activity of the occlusal pits and fissure caries lesion samples, and the diagnostic performance of lesion activity assessment via ICDAS II guideline was also poor based on the low sensitivity and low specificity. This result suggests that clinicians cannot easily distinguish subtle tactile and visual changes in early enamel lesions and the subjectivity plays a large role with conventional diagnostic

methods for lesion activity assessment. As reported in this work and another study by Ekstrand et al., the inter-examiner reproducibility was in general poor for the conventional lesion activity diagnostic methods (Ekstrand et al. 2005). Therefore, the ICDAS II training or score system was not accurate for assessing lesion activity.

ICDAS II Lesion Activity Assessment criteria recommends that examiners use a ball-pointed probe with a diameter of 400 μm for tactile examination, but most pits and fissures are often too narrow for accurate lesion assessment (Banting et al. 2005). The suspected caries lesion may contain microcavitations that are not visible to the naked eye, and this can further confound the conventional diagnostic approach.

Conventional lesion activity assessment that relies on visual and tactile examination lacks certainty and reproducibility, and this work reinforces the importance of new methods with improved diagnostic performance. In a previous PS-OCT study, we demonstrated that an algorithm for automatic detection and measurement of the highly mineralized surface layer could be used on artificial enamel lesions with high accuracy and correlation (Lee et al. 2014). When the algorithm was applied to the PS-OCT images for natural enamel caries lesions, higher sensitivity and specificity were achieved in determining enamel caries lesion activity compared to the conventional tactile and visual exams. In addition, thickness measurements of the highly mineralized surface layer showed strong correlation with histology indicating that PS-OCT could be used for estimating the degree of remineralization.

ICDAS II lesion activity assessment criteria provides a guideline in predicting lesion activity based on lesion location (Banting et al. 2005). Ekstrand et al. classified cariogenic plaque stagnation areas (PSA) on different surfaces (occlusal, buccal, lingual

and proximal surfaces) as an activity predictor (Ekstrand et al. 2007). Our results indicate that the majority of the natural enamel lesions are indeed found in PSA's, but the location of the lesion cannot be used as a sole predictor of lesion activity. For the occlusal pits and fissures lesions, visual and tactile examination is further challenged by the complex anatomy of the tooth. Ekstrand et al. stated that PSA's on occlusal surfaces depends on the size of the pits and fissures, i.e., pits and fissures greater than 400 μm were categorized as PSA's (Ekstrand et al. 2007). However, the histological analysis showed multiple active caries lesions confined within the pits and fissures much smaller than 400 μm diameter.

Furthermore, there was a significant decrease in ΔR , integrated reflectivity, in the arrested lesion group of the pits and fissure caries lesions compared to all other groups as shown in **Table 5.1**. All the arrested caries lesions found in the pits and fissures were incipient enamel caries lesions, which were confined within the outer half of enamel, and most of the active caries lesions in the pits and fissures presented with surface discontinuities. On the contrary, over 80 % of the smooth surface enamel lesions were categorized as arrested lesions.

In a previous study, we also reported that the highly mineralized surface layer plays an important role in the dehydration process and both the thermal and NIR reflectance imaging methods are suitable for detection of remineralization (Lee et al. 2015). In this work, ΔQ , ΔI and OGR measurements were recorded and showed significant differences between active and arrested lesions. The results for smooth surface enamel caries were similar to the measurements from the previous artificial enamel caries lesion study as expected (Lee et al. 2015). However, the occlusal caries

lesions were mostly confined within the center of the pits and fissures and the differences in ΔQ , ΔI and OGR measurements between active and arrested lesions for the pits and fissure caries lesions were greater than those in the smooth surface enamel caries lesions. The anatomic structure of occlusal surface is complex; there are variations in the occlusal anatomy, the distance between surface to DEJ, and the orientation of enamel spindle among different dentition. We implemented seven air-jet nozzles in order to facilitate uniform pressurized air coverage and excess water was removed from the tooth surface with a cotton roll, water still accumulated within the pits and fissures extending the time for dehydration. Although we reported that thermal imaging showed a significant difference in detecting occlusal pits and fissures caries lesions from sound tissue as shown in **Table 5.1**, the difference in ΔQ measurements between the sound pits and fissures and the sound smooth surface was large enough to cause false-positives as shown in **Figs. 5.3G and 5.4G**. Other factors such as differences in the heat dissipation of different materials and the presence of cracks may also influence ΔQ measurements. Zakian et al. reported that a larger ΔQ was observed at the cavity openings because the fissure pattern would be the principal escape route for water (Zakian et al. 2010).

NIR reflectance imaging also suffered from similar problems during the dehydration process but to a lesser extent; the differences in ΔI and OGR measurements between the pits and fissure caries lesions and the smooth surface enamel caries lesions were smaller than ΔQ measurements. Although the complex anatomy of the occlusal surface also introduces challenges in NIR reflectance imaging including greater variation in the angle of incidence, surface scattering, and reflectivity,

the NIR wavelengths utilized in this work are not adversely affected by heat dissipation problem found in ΔQ measurements. Thus, the NIR measurements are more localized and provide higher spatial resolution compared to thermal imaging. Our findings suggest that both the ΔI and OGR measurements provide useful information about the remineralization status of the lesion. In our previous study, we reported that OGR could be used to accentuate the active enamel lesions in artificial enamel model (Lee et al. 2015). As shown in **Figs. 5.2I and 5.4I**, OGR shows the location of active enamel caries lesions with high contrast.

5.6 CONCLUSION

Our findings suggest that dehydration measurements with thermal and NIR reflectance imaging are suitable for assessment of enamel caries lesion activity. NIR reflectance imaging was the most effective and selective method in detecting active enamel caries lesions during the dehydration process. PS-OCT coupled with the automated algorithm was effective in detection and measurement of the highly mineralized surface layer in natural caries lesions. Images generated with PS-OCT provide useful information for estimating the severity and the degree of remineralization of the lesion. This chapter shows that the novel optical imaging methods are suitable for enamel caries lesion activity assessment in a single examination and that these imaging methods are superior in accuracy and selectivity in enamel caries lesion activity assessment compared to the conventional visual and tactile examination.

5.7 FIGURES AND FIGURE LEGENDS

Table 5.1 ΔR , ΔQ , ΔI and OGR measurements. Groups with the same letters are statistically similar, $P > 0.05$ in each row.

	Smooth Surfaces		Pits and Fissures	
	Active (n = 4)	Arrested (n = 18)	Active (n = 10)	Arrested (n = 10)
ΔR (dB $\times\mu\text{m}$)	1276 \pm 456 a	1226 \pm 445 a	1139 \pm 582 a	548 \pm 271 b
ΔQ (K \times s)	16.9 \pm 17.1 ab	0.9 \pm 1.7 c	31.0 \pm 15.6 a	7.3 \pm 4.2 bc
ΔI	207 \pm 88 ab	41 \pm 28 c	231 \pm 205 a	48 \pm 28 bc
OGR	33.3 \pm 16.1 ab	3.4 \pm 2.5 c	45.3 \pm 38.1 a	6.5 \pm 4.4 bc

Table 5.2 ROC curve analysis of ΔR , ΔQ , ΔI and OGR measurements.

	Smooth Surfaces		Pits and Fissures	
	AUC*	P-value	AUC*	P-value
ΔR (PS-OCT)	0.51	0.9322	0.84	0.0102
ΔQ (Thermal)	0.97	0.0038	0.95	0.0007
ΔI (NIR)	0.99	0.0029	0.97	0.0004
OGR (NIR)	1.00	0.0022	0.94	0.0009

*AUC represents the area under the curve of the ROC analysis

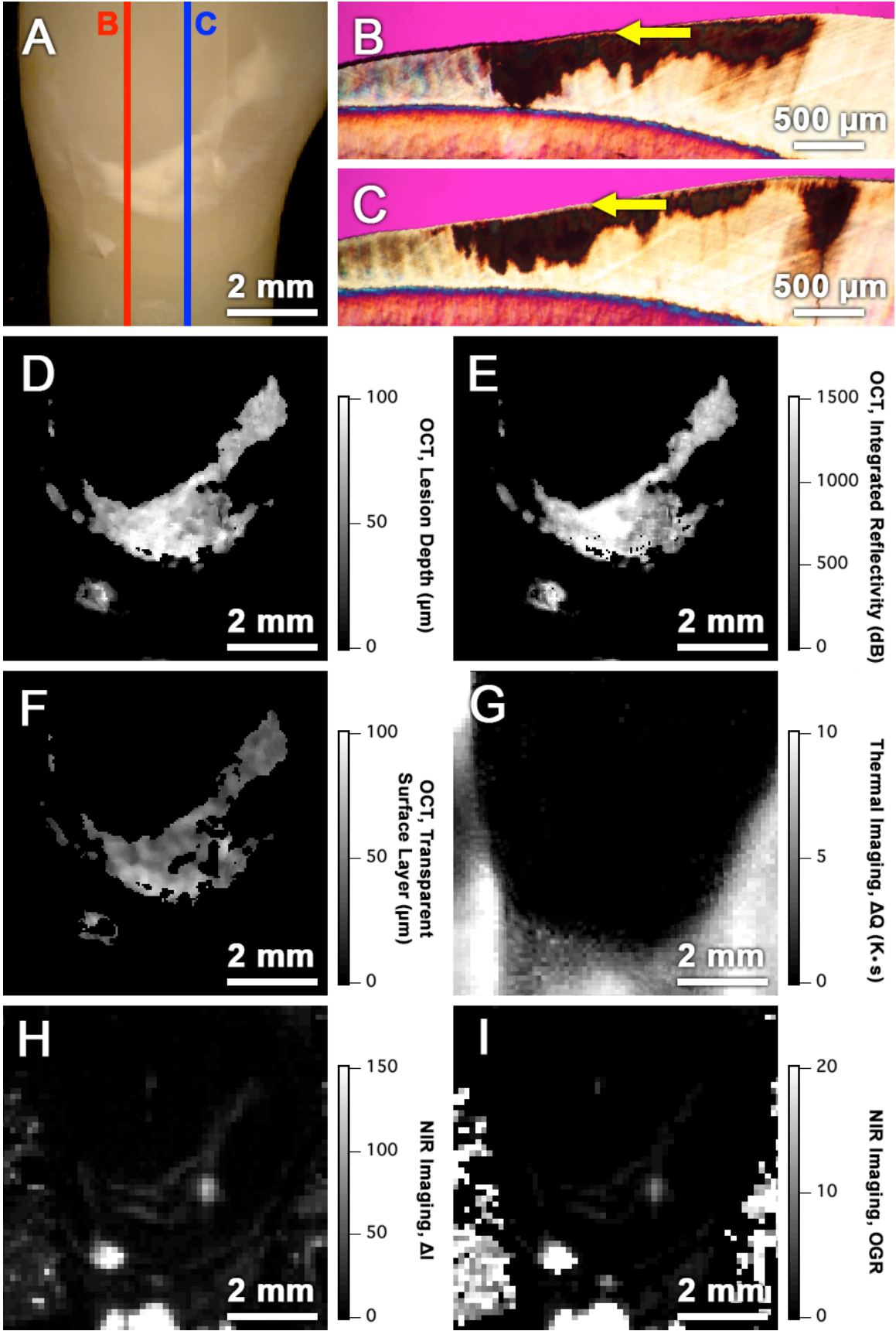


Figure 5.1 Visible, cross-sectional PLM, PS-OCT, thermal, and NIR reflectance images of an arrested smooth surface enamel caries lesion. The red line in the visible light reflectance image (A) represents the position of the PLM section shown in (B) and the blue line represents the position of the PLM section shown in (C). Lesion depths (D), lesion severity, estimated with integrated reflectivity (E), and transparent surface layer thickness (F) measurements with PS-OCT correlate well with histology (B and C). ΔQ (G) measurements with thermal imaging and ΔI (H) and OGR (I) measurements with NIR imaging show the suspected lesion. Yellow arrows designate the position of the respective surface zones.

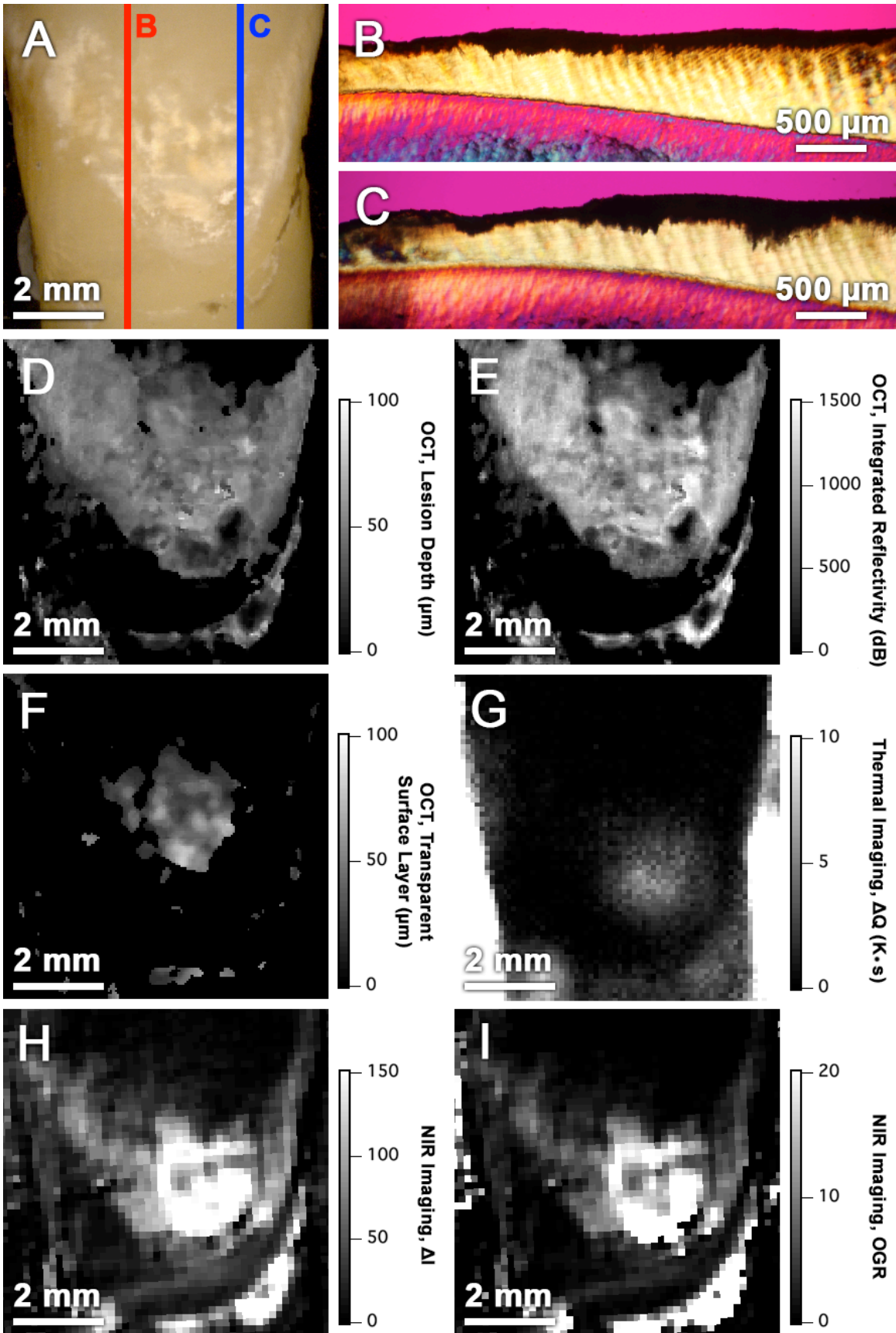


Figure 5.2 Visible, cross-sectional PLM, PS-OCT, thermal, and NIR reflectance images of an active smooth surface enamel caries lesion. The red line in the visible light reflectance image (A) represents the position of the PLM section shown in (B) and the blue line represents the position of the PLM section shown in (C). Lesion depths (D), lesion severity, estimated with integrated reflectivity (E), and transparent surface layer thickness (F) measurements with PS-OCT correlate well with histology (B and C). ΔQ (G) measurements with thermal imaging and ΔI (H) and OGR (I) measurements with NIR imaging show the suspected lesion.

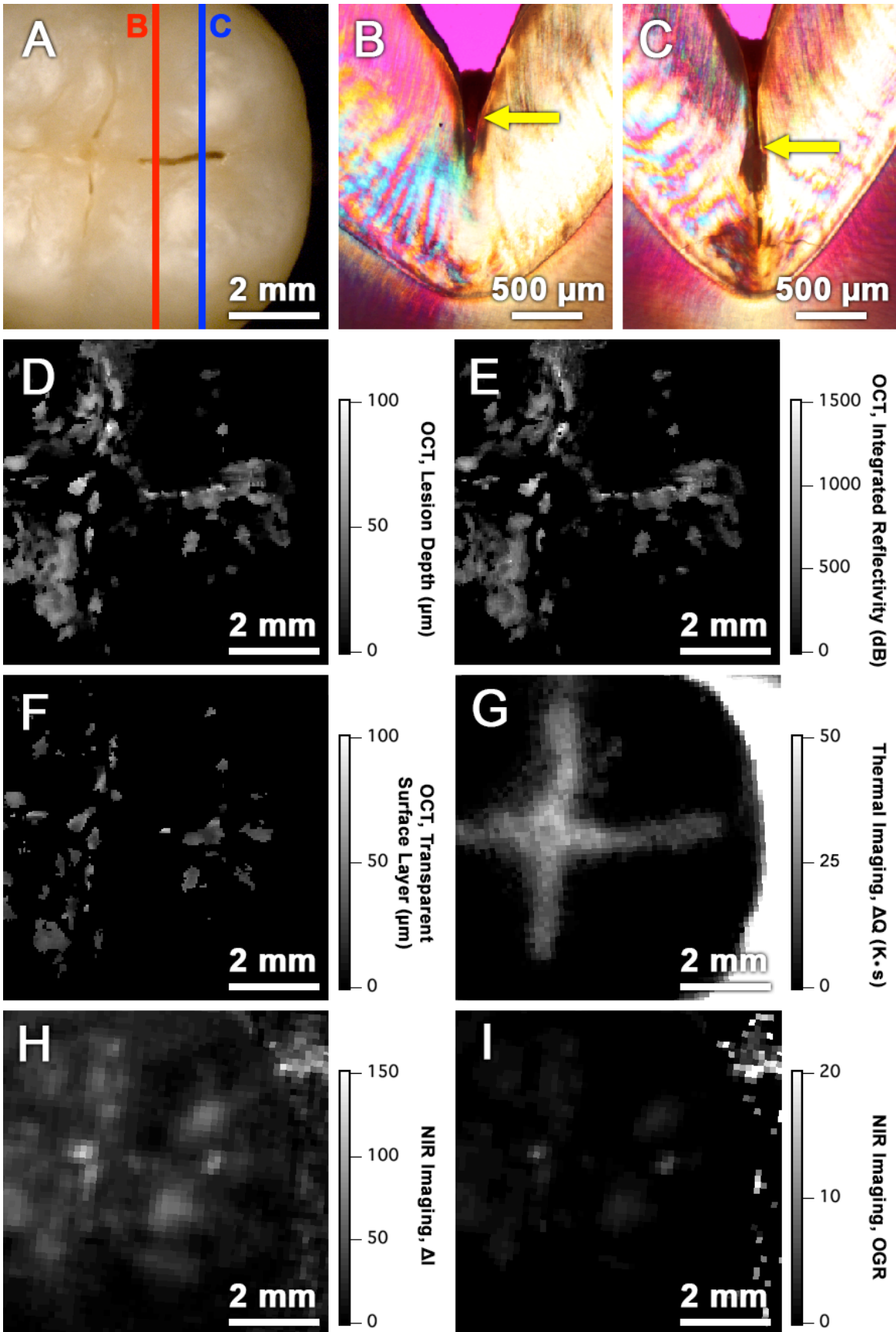


Figure 5.3 Visible, cross-sectional PLM, PS-OCT, thermal, and NIR reflectance images of an arrested occlusal pits and fissure caries lesion. The red line in the visible light reflectance image (A) represents the position of the PLM section shown in (B) and the blue line represents the position of the PLM section shown in (C). Lesion depths (D), lesion severity, estimated with integrated reflectivity (E), and transparent surface layer thickness (F) measurements with PS-OCT correlate well with histology (B and C). ΔQ (G) measurements with thermal imaging and ΔI (H) and OGR (I) measurements with NIR imaging show the suspected lesion. Yellow arrows designate the position of the respective surface zones.

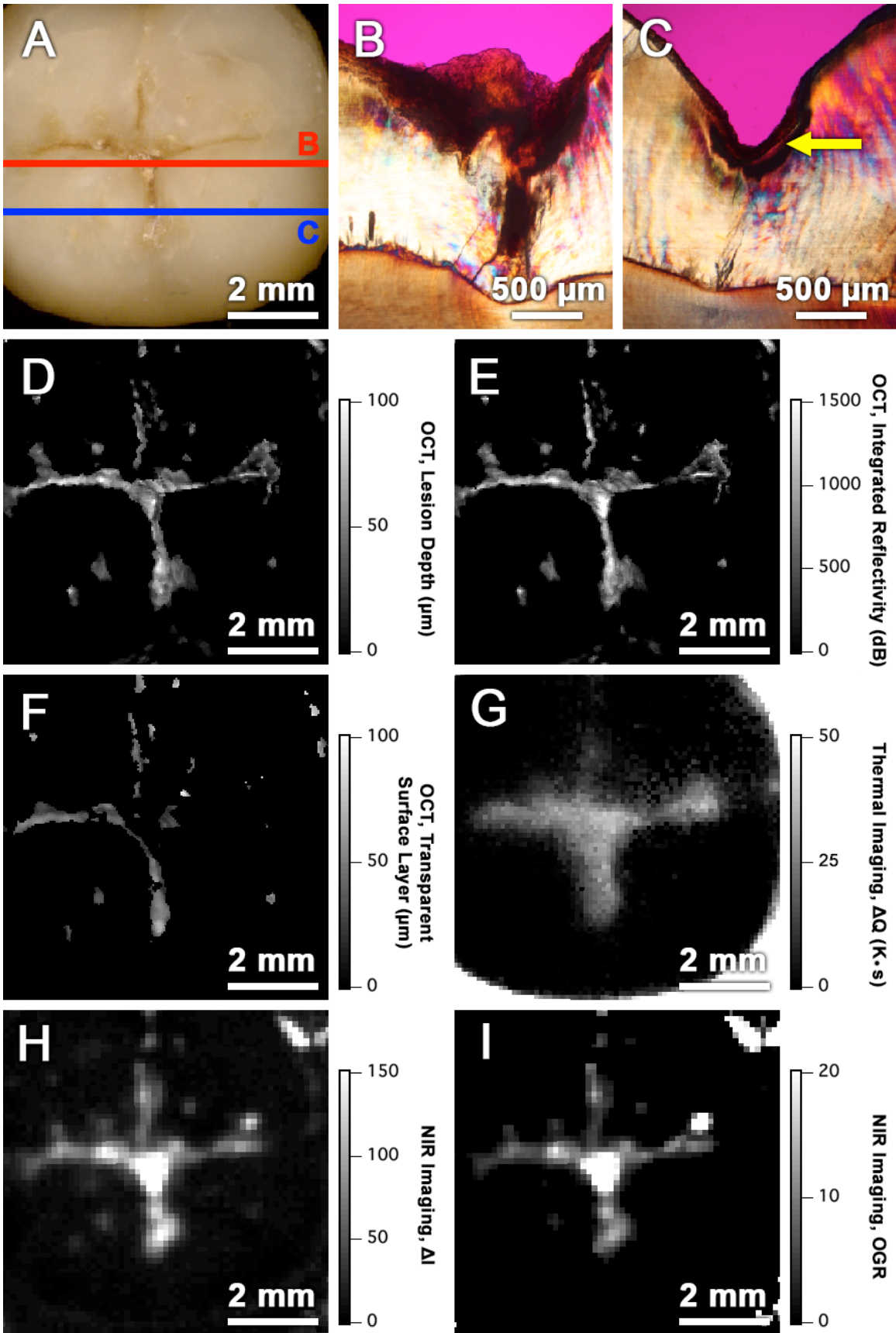


Figure 5.4 Visible, cross-sectional PLM, PS-OCT, thermal, and NIR reflectance images of an active occlusal pits and fissure caries lesion. The red line in the visible light reflectance image (A) represents the position of the PLM section shown in (B) and the blue line represents the position of the PLM section shown in (C). Lesion depths (D), lesion severity, estimated with integrated reflectivity (E), and transparent surface layer thickness (F) measurements with PS-OCT correlate well with histology (B and C). ΔQ (G) measurements with thermal imaging and ΔI (H) and OGR (I) measurements with NIR imaging show the suspected lesion. A yellow arrow designates the position of the respective surface zones.

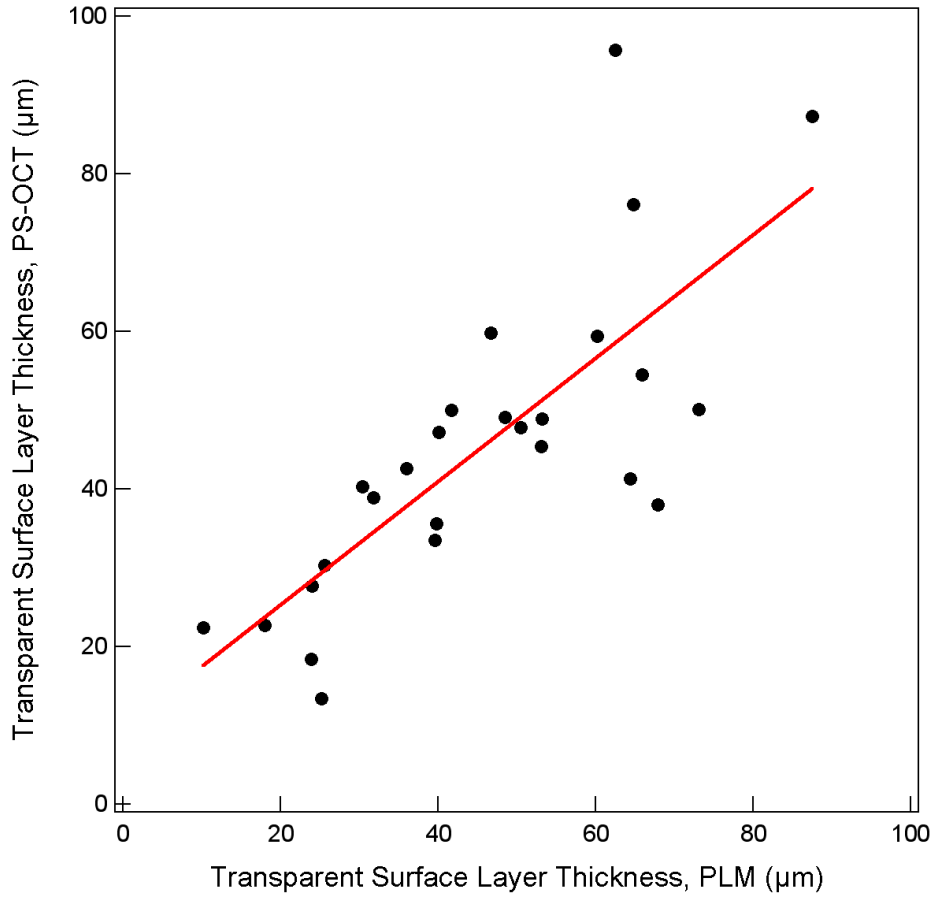


Figure 5.5 A plot of transparent surface layer thickness determined with histology (PLM) vs. thickness estimated from the automated algorithm (PS-OCT). Only the true-negative samples are shown above (n = 26).

5.8 REFERENCES

- Amaechi, B. T., Higham, S. M., Podoleanu, A. g., Rodgers, J. A. and Jackson, D. A. (2001). Use of Optical Coherence Tomography for Assessment of Dental caries. *J. Oral Rehab.*, **28**(12): 1092-1093.
- Ando, M., Sharp, N. and Adams, D. (2012). Pulse thermography for quantitative nondestructive evaluation of sound, de-mineralized and re-mineralized enamel. *Proc. SPIE Health Monitoring of Structural and Biological Systems I*, San Diego, CA, **8348**: S1-7.
- Ando, M., Stookey, G. K. and Zero, D. T. (2006). Ability of quantitative light-induced fluorescence (QLF) to assess the activity of white spot lesions during dehydration. *Am. J. Dent.*, **19**(1): 15-18.
- Arends, J., Ruben, J. L. and Inaba, D. (1997). Major topics in quantitative microradiography of enamel and dentin: R parameter, mineral distribution visualization, and hyper-remineralization. *Adv. Dent. Res.*, **11**(4): 403-414.
- Banting, D., Eggertsson, H., Ekstrand, K. R., Ferreira-Zandona, A., Ismail, A. I., Longbottom, C., Pitts, N., Reich, E., Ricketts, D., Selwitz, R., Sohn, W., Topping, G. and Zero, D. (2005). Rationale and evidence for the International Caries Detection and Assessment System (ICDAS II). *Proc. the 7th Annual Indiana Conference: Clinical Models Workshop: Remin-Demin, Precavitation, Caries*, Indianapolis, IN, 161-221.
- Bush, J., Davis, P. and Marcus, M. A. (2000). All-fiber optic coherence domain interferometric techniques. *Proc. SPIE Fiber Optic Sensor Technology II*, San Jose, CA, **4204**: 71-80.
- Chan, K. H., Chan, A. C., Fried, W. A., Simon, J. C., Darling, C. L. and Fried, D. (2013). Use of 2D images of depth and integrated reflectivity to represent the severity of demineralization in cross-polarization optical coherence tomography. *J. Biophotonics*, **8**: 36-45.
- Chong, S. L., Darling, C. L. and Fried, D. (2007). Nondestructive measurement of the inhibition of demineralization on smooth surfaces using polarization-sensitive optical coherence tomography. *Lasers Surg. Med.*, **39**(5): 422-427.
- Chung, S., Fried, D., Staninec, M. and Darling, C. L. (2011). Multispectral near-IR reflectance and transillumination imaging of teeth. *Biomed. Opt. Express*, **2**(10): 2804-2814.
- Darling, C. L., Featherstone, J. D. B., Le, C. Q. and Fried, D. (2009). An automated digital microradiography system for assessing tooth demineralization. *Proc. SPIE Lasers in Dentistry VX*, San Jose, CA, **7162**: T1-7.

- Ekstrand, K. R., Martignon, S., Ricketts, D. J. and Qvist, V. (2007). Detection and activity assessment of primary coronal caries lesions: a methodologic study. *Oper. Dent.*, **32**(3): 225-235.
- Ekstrand, K. R., Ricketts, D. N., Longbottom, C. and Pitts, N. B. (2005). Visual and tactile assessment of arrested initial enamel carious lesions: an in vivo pilot study. *Caries Res.*, **39**(3): 173-177.
- Ekstrand, K. R., Zero, D. T., Martignon, S. and Pitts, N. B. (2009). Lesion activity assessment. *Monogr. Oral Sci.*, **21**: 63-90.
- Fried, D., Xie, J., Shafi, S., Featherstone, J. D. B., Breunig, T. M. and Le, C. Q. (2002). Early detection of dental caries and lesion progression with polarization sensitive optical coherence tomography. *J. Biomed. Opt.*, **7**(4): 618-627.
- Fried, W. A., Darling, C. L., Chan, K. and Fried, D. (2013). High contrast reflectance imaging of simulated lesions on tooth occlusal surfaces at near-IR wavelengths. *Lasers Surg. Med.*, **45**(8): 533-541.
- Jones, R. S., Darling, C. L., Featherstone, J. D. B. and Fried, D. (2006). Imaging artificial caries on the occlusal surfaces with polarization-sensitive optical coherence tomography. *Caries Res.*, **40**(2): 81-89.
- Jones, R. S., Darling, C. L., Featherstone, J. D. B. and Fried, D. (2006). Remineralization of in vitro dental caries assessed with polarization sensitive optical coherence tomography. *J. Biomed Opt.*, **11**(1): 014016.
- Kaneko, K., Matsuyama, K. and Nakashima, S. (1999). Quantification of early carious enamel lesions by using an infrared camera. *Proc. the 4th Annual Indiana Conference: Early Detection of dental caries II*, Indianapolis, IN, 83-99.
- Kidd, E. A. (1983). The histopathology of enamel caries in young and old permanent teeth. *Br. Dent. J.*, **155**(6): 196-198.
- Kidd, E. A. M. and Joyston-Bechal, S. (1997). *Dental caries: the disease and its clinical management*, Oxford University Press.
- Lee, R. C., Darling, C. L. and Fried, D. (2014). Automated detection of remineralization in simulated enamel lesions with PS-OCT. *SPIE Lasers in Dentistry XX*, San Jose, CA, **8929**: E1-8.
- Lee, R. C., Darling, C. L. and Fried, D. (2015). Assessment of remineralization via measurement of dehydration rates with thermal and near-IR reflectance imaging. *J. Dent.*, **43**(8): 1032-1042.

Lee, R. C., Kang, H., Darling, C. L. and Fried, D. (2014). Automated assessment of the remineralization of artificial enamel lesions with polarization-sensitive optical coherence tomography. *Biomed. Opt. Express*, **5**(9): 2950-2962.

Lin, M., Liu, Q. D., Xu, F., Bai, B. F. and Lu, T. J. (2009). In vitro investigation of heat transfer in human tooth. *Proc. SPIE Experimental Mechanics IV*, Singapore, Singapore, **7522**: N1-7.

Louie, T., Lee, C., Hsu, D., Hirasuna, K., Manesh, S., Staninec, M., Darling, C. L. and Fried, D. (2010). Clinical assessment of early tooth demineralization using polarization sensitive optical coherence tomography. *Lasers Surg. Med.*, **42**(10): 738-745.

Natsume, Y., Nakashima, S., Sadr, A., Shimada, Y., Tagami, J. and Sumi, Y. (2011). Estimation of lesion progress in artificial root caries by swept source optical coherence tomography in comparison to transverse microradiography. *J. Biomed. Opt.*, **16**(7): 071408.

Nee, A., Chan, K., Kang, H., Staninec, M., Darling, C. L. and Fried, D. (2014). Longitudinal monitoring of demineralization peripheral to orthodontic brackets using cross polarization optical coherence tomography. *J. Dent.*, **42**(5): 547-555.

Ngaotheppitak, P., Darling, C. L. and Fried, D. (2005). Measurement of the severity of natural smooth surface (interproximal) caries lesions with polarization sensitive optical coherence tomography. *Lasers Surg. Med.*, **37**(1): 78-88.

NIH (2001). Diagnosis and management of dental caries throughout life, *NIH Consensus Statement*, **18**: 1-24.

Nyvad, B., Machiulskiene, V. and Baelum, V. (1999). Reliability of a new caries diagnostic system differentiating between active and inactive caries lesions. *Caries Res.*, **33**(4): 252-260.

Shimada, Y., Sadr, A., Burrow, M. F., Tagami, J., Ozawa, N. and Sumi, Y. (2010). Validation of swept-source optical coherence tomography (SS-OCT) for the diagnosis of occlusal caries. *J. Dent.*, **38**(8): 655-665.

Simon, J. C., Chan, K. H., Darling, C. L. and Fried, D. (2014). Multispectral near-IR reflectance imaging of simulated early occlusal lesions: Variation of lesion contrast with lesion depth and severity. *Lasers Surg. Med.*, **46**(3): 203-215.

ten Cate, J. M. and Arends, J. (1977). Remineralization of artificial enamel lesions in vitro. *Caries Res.*, **11**(5): 277-286.

ten Cate, J. M. and Featherstone, J. D. B. (1991). Mechanistic aspects of the interactions between fluoride and dental enamel. *Crit. Rev. Oral Biol. Med.*, **2**: 283-296.

Thylstrup, A., Bruun, C. and Holmen, L. (1994). In vivo caries models-mechanisms for caries initiation and arrestment. *Adv. Dent. Res.*, **8**(2): 144-157.

Usenik, P., Bürmen, M., Fidler, A., Pernuš, F. and Likar, B. (2014). Near-infrared hyperspectral imaging of water evaporation dynamics for early detection of incipient caries. *J. Dent.*, **42**(10):1242-1247.

Wenzel, A. (2008). Dental Caries. *Oral radiology: principles and interpretation*. White, S. C. and Pharoah, M. J. Eds., Mosby Elsevier: 270-281.

Zakian, C. M., Taylor, A. M., Ellwood, R. P. and Pretty, I. A. (2010). Occlusal caries detection by using thermal imaging. *J. Dent.*, **38**(10): 788-795.

CHAPTER VI

ACTIVITY ASSESSMENT OF ROOT CARIES LESIONS WITH THERMAL AND NEAR-INFRARED IMAGING METHODS

6.1 SUMMARY

The purpose of this work was to evaluate thermal and near-infrared (NIR) reflectance imaging methods for the assessment of the activity of root caries lesions. In addition, changes in the lesion structure were monitored with polarization sensitive optical coherence tomography (PS-OCT). Artificial bovine and natural root caries lesions were imaged with PS-OCT, and their dehydration rate was measured with thermal and NIR cameras. The lesion activity of the natural root caries samples was also assessed by two clinicians by conventional means according to ICDAS II guidelines. The thickness of the highly mineralized transparent surface layer measured using PS-OCT increased and the area enclosed by the time-temperature curve, ΔQ , measured with thermal imaging decreased significantly with longer periods of remineralization in simulated dentin lesions, but the NIR reflectance intensity differences, ΔI , failed to show any significant relationship with the degree of remineralization. The PS-OCT algorithm for the automated assessment of remineralization successfully detected the highly mineralized surface layer on both natural and simulated lesions. Thermal imaging provided the most accurate diagnosis of root caries lesion activity. These results demonstrate that thermal imaging and PS-OCT may be ideally suited for the nondestructive root caries lesion activity during a clinical examination.

6.2 INTRODUCTION

Exposed dentin is a risk factor for root caries and dentin hypersensitivity (Sumney et al. 1973, Holland et al. 1997, Canadian Advisory Board on Dentin Hypersensitivity 2003, West et al. 2013). Etiologies of exposed dentin include loss of overlying enamel and

gingival recession due to loss of periodontal structures (Sumney et al. 1973, Holland et al. 1997). It has been reported that dentin exposure increases significantly with age, inadequate oral hygiene and excessive tooth brushing (Tugnait and Clerehugh 2001). The abrasive and erosive wear properties of dentin are significantly lower than those of enamel due to the higher organic content and more reactive mineral phase (Kinney et al. 2003). Dentin surfaces are more susceptible to carious attack than enamel surfaces and the fluid flow within dentinal tubules can induce nociceptor activation in the pulp (Kawasaki and Featherstone 1997, Bignozzi et al. 2014). It has been well established that early root caries and dentin hypersensitivity can be treated via non-surgical approaches such as fluoride application; the permeability and reactivity of exposed dentin surfaces may be modified so that they become less susceptible to future cariogenic challenges and dentin hypersensitivity (Brannstrom 1966, Fejerskov and Kidd 2003). Therefore, it is essential to have non-destructive methods to assess the condition of the exposed dentin in order to determine whether the lesion requires chemical or surgical intervention.

It is extremely difficult to detect early root caries due to its rapid progression and lack of reliable diagnostic techniques (Fejerskov and Kidd 2003). The international Caries Detection and Assessment System (ICDAS) coordinating committee and Ekstrand et al. proposed clinical scoring systems for assessing root caries lesion activity (Banting et al. 2005, Ekstrand et al. 2008). However, the clinical methods for root caries lesion activity assessment lack histological validation and are composed of visual and tactile exams, which are prone to subjective bias and interference from staining (Lynch and Beighton 1994). Histological analyses for lesion assessment such as transverse

microradiography (TMR) and polarized light microscopy (PLM) require destruction of the tooth and are not suitable for use *in-vivo*. Accurate diagnosis of early root caries and non-cariou cervical lesions (NCCL) will allow clinicians to apply appropriate treatments for occlusion of dentinal tubules and restoration of the lost tooth structure.

Optical coherence tomography (OCT) is a non-invasive technique for creating cross-sectional images of internal biological structures. Polarization sensitivity is particularly valuable for resolving the structure of early caries lesions because caries lesions strongly scatter incident polarized light and the image in the polarization axis orthogonal to that of the incident polarization can provide improved lesion contrast. Polarization-sensitive OCT (PS-OCT) has been successfully used to acquire images of both artificial and natural caries lesions, assess their severity in depth and assess the remineralization of such lesions on enamel and dentin (Everett et al. 1999, Fried et al. 2002, Manesh et al. 2009). Even though the penetration of near-infrared (NIR) light is markedly reduced in dentin due to higher light scattering and absorption, PS-OCT can effectively be used to discriminate demineralized dentin from sound dentin and cementum (Lee et al. 2009). PS-OCT has also been used to measure remineralization on dentin surfaces and to detect the formation of a highly mineralized layer on the lesion surface after exposure to a remineralization solution (Manesh et al. 2009). In previous studies, we developed approaches to automatically detect the highly mineralized surface layer of enamel lesions exposed to remineralization solutions and measure its thickness with high accuracy (Lee et al. 2014). In this chapter, we modified the algorithm to automatically detect and measure the remineralization in simulated dentin lesions and natural root caries lesions.

The organic scaffold and dentinal tubules are occupied by mostly water when hydrated (Kinney et al. 1993). The capacity of water retention of dentin increases with the increase in severity of demineralization and the size of dentinal tubules (Ozok et al. 2002). Therefore, loss of mobile water from the lesion and sound dentin is likely to be highly dependent on the structure and mineral content of the exposed dentin surface. The optical changes associated with water loss have been investigated via thermal imaging and NIR imaging for enamel caries lesions (Kaneko et al. 1999, Ando et al. 2012, Usenik et al. 2014). The influence of hydration on dentin lesions can also be investigated as an indirect indicator of the decreased permeability of water due to remineralization.

Evaporation of water from a lesion is an endothermic process, which causes a temperature decrease followed by a recovery to thermal equilibrium as the lesion becomes dry. Kaneko et al. and Zakian et al. carried out thermal imaging studies using an infrared camera and an air-jet for evaporation on occlusal and smooth natural tooth enamel surfaces (Kaneko et al. 1999, Zakian et al. 2010). In our most recent study, the thermal imaging via dehydration was also found to be suitable for detection of remineralization of enamel (Lee et al. 2015).

Near-infrared imaging has also been exploited for caries detection since sound enamel is transparent in the NIR and the scattering coefficient increases exponentially with increasing mineral loss (Darling et al. 2006). Zakian et al. showed that the reflectance from sound tooth areas decreases at longer wavelengths where water absorption is higher (Zakian et al. 2009). We demonstrated that the rate of water evaporation from enamel could be analyzed for the assessment of remineralization (Lee

et al. 2015). However, sound dentin manifests higher scattering and absorption coefficients, almost an order of magnitude higher than enamel, due to the presence of dentinal tubules of 1 – 3 μm in diameter and an organic matrix largely composed of collagen (Chan et al. 2014). It is anticipated that the high water content of dentin increases the lesion contrast during the dehydration process.

In this chapter, PS-OCT was used to measure the severity and the thickness of the highly mineralized surface zone of simulated dentin and natural root caries lesions. In addition, lesion dehydration rates were measured using thermal and near-infrared reflectance imaging with the aim of developing new methods for the assessment of lesion activity on root surfaces.

6.3 MATERIALS AND METHODS

Two sets of samples were used: simulated bovine dentin lesion samples and natural human root caries lesion samples. **Figure 6.1** shows a flowchart of the experimental design employed.

6.3.1 Simulated Dentin Lesion Sample Preparation

Dentin blocks ($n = 30$), approximately 8 – 12 mm in length with a width of 2 mm and a thickness of 2 mm were prepared from extracted bovine incisors acquired from a slaughterhouse. The bovine enamel was removed from the outer surface towards the dentinoenamel junction (DEJ) exposing the dentin and the surfaces of the bovine dentin blocks were ground to a 9 μm finish to create a smooth dentin surface. Each sample was partitioned into six windows (1 sound control, 4 lesion and 1 remineralization

control) by etching small incisions 1.8 mm apart across each of the dentin blocks using a laser. Incisions were etched using a transverse excited atmospheric pressure (TEA) CO₂ laser, an Impact 2500, GSI Lumonics (Rugby, UK), operating at 9.3 μm with a pulse duration of 15 μs, a pulse repetition rate of 200 Hz and a fluence of 20 J/cm².

A thin layer of acid-resistant varnish in the form of nail polish, Revlon (New York, NY), was applied to protect the sound and remineralization control windows before exposure to the demineralization solution. Two groups (n = 15 per group) of dentin samples each with four exposed lesion windows were immersed in 45 mL aliquots of the demineralization solution for 8 and 24 hours, respectively. The demineralization solution, which was maintained at 37°C and pH 4.9, was composed of 2.0 mmol/L calcium, 2.0 mmol/L phosphate and 0.075 mol/L acetate. After the demineralization period, the acid resistant varnish was removed by immersion in acetone in an ultrasonic bath for 15 minutes and the acid-resistant varnish was applied again to the sound and lesion windows.

Sample windows were subsequently exposed to an acidic remineralization solution for 4, 8 or 12-days by covering appropriate windows with acid resistant varnish at each time point. It has been hypothesized that the lower pH reduces preferential deposition of mineral in the outer enamel, enhancing remineralization of the lesion body (Yamazaki and Margolis 2008). This model has only been previously applied to enamel, and to the best of our knowledge, this is the first time it has been applied to dentin. The acidic remineralization solution was composed of 4.1 mmol/L calcium, 15 mmol/L phosphate, 50 mmol/L lactic acid, 20 mmol/L HEPES buffer and 2 ppm F⁻ maintained at 37°C and a pH of 4.9 (Yamazaki and Margolis 2008). The remineralization control

window was exposed to the acidic remineralization solution for 12 days in order to examine its effect on sound dentin. After the 12 days of remineralization, the acid resistant varnish was removed and the samples were stored in a 0.1 % thymol solution to prevent fungal and bacterial growth.

6.3.2 Natural Root Caries Lesion Sample Selection and Examination

Teeth extracted from patients in the San Francisco Bay area were collected, cleaned and sterilized with Gamma radiation. Twenty-five teeth with suspected caries lesions were selected with scores of 1 or 2 based on the ICDAS II root caries lesion classification (Banting et al. 2005). The coronal portions of the teeth were cut off and the root portions of teeth were mounted on 1.2 cm x 1.2 cm x 3 cm delrin blocks. The buccal surfaces of the cervical root portion of the teeth were scored according to the ICDAS II root caries lesion activity assessment criteria system via visual and tactile examination independently by two trained clinicians (Banting et al. 2005). Prior to the experiment, clinicians had been extensively calibrated through practical exercises. Ball ended periodontal probes were used to gently check for loss of tooth structure and surface texture without damaging the tooth structure.

6.3.3 PS-OCT System

The PS-OCT system used in this work has been described previously (Fried et al. 2002). An all fiber-based Optical Coherence Domain Reflectometry (OCDR) system with polarization maintaining (PM) optical fiber, high speed piezoelectric fiber-stretchers and two balanced InGaAs receivers that was designed and fabricated by Optiphase, Inc.,

Van Nuys, CA, USA was used to acquire the images (Bush et al. 2000). This two-channel system was integrated with a broadband superluminescent diode (SLD) DL-CS3159A, Denselight (Jessup, MD, USA) and a high-speed XY-scanning motion controller system, ESP 300 controller with ILS100PP and 850G-HS stages, (Newport, Irvine, CA, USA) for *in-vitro* optical coherence tomography. A high power (15 mW) polarized SLD source operated at a center wavelength of 1317 nm with a spectral bandwidth full-width-half-maximum (FWHM) of 84 nm was used to provide an axial resolution of 9 μm in air and 6 μm in dentin (refractive index = 1.5). Light from the sample arm was focused onto the sample surface using a 20 mm focal length plano-convex lens providing a lateral resolution of approximately 20 μm .

The PS-OCT system was completely controlled using LabView™ software (National Instruments, Austin, TX, USA). Samples were dried with pressurized air for 30 seconds prior to scanning. Each B-scan consisted of 300 A-scans spaced 50 μm apart. The A-scan sweep rate was 150 Hz with a dynamic range of 48 dB and each A-scan was an average of 10 scans. The total number of data points in each A-scan was 2000 over a scan range of approximately 5 mm in air.

6.3.4 Calculation of Surface Layer Thickness, Shrinkage, Lesion Depth and Integrated Reflectivity (ΔR)

PS-OCT images were processed using a dedicated program constructed with LabView™ software. There was a phase shift in the PM-fiber between the two axes, so an axial position calibration was performed once prior to the experiment. A gold mirror was scanned at a 150 Hz sweep rate and each A-scan was an average of 100 scans.

Five hundred A-scans were acquired at 10 μm intervals over the entire scan range to determine the required axial position adjustments and the axial position of the cross-polarization scan images was adjusted to match the co-polarization scan images.

Previously employed image processing methods for surface layer detection and measurement utilized an edge detection technique using the zero-crossing first-order derivative (Lee et al. 2014, Lee et al. 2014). In this work, the threshold requirements for the ratio of the intensity values of the edge and the second peak were removed from the surface layer detection algorithm for dentin samples.

Previous studies have shown that the integrated reflectivity, ΔR , over the estimated lesion depth positively correlates with the integrated mineral loss (volume percent mineral loss $\times \mu\text{m}$), ΔZ (Ngaotheppitak et al. 2005, Jones et al. 2006). ΔR was calculated by integrating from the base of the surface layer through the entire estimated lesion body in the cross-polarization (CP) OCT images (Lee et al. 2014). This had the added advantage of removing the contribution of the high specular reflection at the surface of the sample, which was large enough to be present even in the CP-OCT images.

Shrinkage was significant for the PS-OCT images in the zones of demineralization due to rapid dehydration after exposure to air. The simulated dentin lesions had relatively flat lesion surfaces while the natural root caries lesions had irregular lesion surfaces, thus shrinkage adjustments were only carried out for the simulated dentin lesions. The surface reflection measured in the co-polarization axis from the PS-OCT images was used to measure the shrinkage. We employed a previously developed approach to adjust for shrinkage in the lesion depth and

integrated reflectivity measurements (Lee et al. 2009). Shrinkage is expected to cause an overall loss in the integrated reflectivity from the lesion. The correction is predicated on the assumption that the additional mineral present in the dentin lesion area due to contraction from shrinkage causes no net change in reflectivity. This is a reasonable assumption since initial demineralization causes pores to be formed in the tissue that produce an increase in light scattering as the demineralization becomes more severe. The increase in light scattering reaches a plateau since pores merge and further demineralization does not increase the number or density of scattering sites (Darling et al. 2006). Therefore, a further change in reflectivity above a certain level of mineral loss is not anticipated.

A region of interest (ROI) was specified for the sound region from each sample in order to discriminate between demineralized and sound dentin. ΔR was calculated from the selected ROI and it was compared to the ΔR of the lesions in order to reduce false-positives in lesion detection. The surface layer, lesion depth and ΔR measurements were estimated by averaging 25 A-scans from a 5×5 pixel region of interest. A 5×5 pixel median filter was applied to the final 2D projection images for improved visualization.

Three-dimensional images were constructed by compiling the post-processed images using Avizo™ 9.0 software (FEI Visualization Sciences Group, Hillsboro, OR, USA).

6.3.5 Dehydration Measurements

The following setup was used for the dehydration experiments of sections 6.3.6 and 6.3.7. Each sample was placed in a mount connected to a high-speed XY-scanning motion controller system, Newport ESP 300 controller & 850G-HS stages coupled with an air nozzle and a light source as shown in the first figure of reference (Lee et al. 2015). The dehydration setup was completely automated using LabView™ software.

All surfaces of the simulated dentin lesion samples, excluding the windows, were covered with black nail polish, OPI (North Hollywood, CA, USA) in order to confine water loss to the exposed surface and prevent the transmission of light through the sides of the sample. Each simulated dentin lesion sample was immersed in the water bath for 30 seconds while being vigorously shaken to enhance water diffusion. After the sample was removed from the water bath, an image was captured as an initial reference image and the air spray was activated. The air pressure was set to 15 psi and the computer controlled air nozzle was positioned 2 cm away from the sample. Each measurement consisted of capturing a sequence of images at 4 frames per second for 30 seconds. For each measurement, the air nozzle was centered on the ROI, and this process was repeated for each window (6 times per sample).

The dehydration setup was slightly modified for the natural root caries lesion samples due to their complex anatomical structures. After the samples were removed from the water bath, the excess water on the surface of the lesions was removed with a disposable cotton roll. Seven air nozzles were positioned 5 cm away from the sample and the air pressure was set to 12 psi to ensure uniform distribution of airflow. The duration of the dehydration was set to 60 seconds instead of 30 seconds in order to

ensure adequate dehydration of the natural root caries samples.

6.3.6 NIR Reflectance Imaging and Analysis

An infrared (IR) thermography camera, Model A65 (FLIR Systems, Wilsonville, OR, USA) sensitive from 8 – 13 μm with a resolution of 640 x 512 pixels, a thermal sensitivity of 50 mK and a lens with a 13 mm focal length was used to record temperature changes during the dehydration process. The area per pixel was approximately 0.02 mm^2 . The ambient room temperature, flowing air temperature and water bath temperature were approximately 21 °C (294.15 K) and were consistent throughout the experiment. The object emissivity was set to 0.92, and the atmospheric temperature was set to 294.15 K (Lin et al. 2009). Relative humidity was set at a default value of 50%; humidity values were not recorded, but every sample was measured under the same conditions. Previous studies have shown that ΔQ , the area enclosed by the time-temperature curve, can be used as a quantitative measure of porosity and can be used to discriminate between the demineralized enamel and the remineralized or sound enamel *in-vitro* (Zakian et al. 2010, Lee et al. 2015).

Thermal images were processed and analyzed using a dedicated program written in LabviewTM. The thermography camera outputs a series of temperature measurements over time. The initial reference temperature measurements varied slightly (± 0.5 K) due to the different emissivity, lesion structure, mineral composition and water content among windows. Calibration was carried out via matching the measurements from the initial reference image to the ambient temperature. ΔQ was calculated from the area enclosed by the initial temperature and the time-temperature

curve, acquired from an average measurement of a 3 × 3 pixel ROI for each window.

6.3.7 NIR Reflectance Imaging and Analysis

A NIR camera, Indigo Alpha (FLIR Systems, Wilsonville, OR, USA) with an InGaAs focal plane array, a spectral sensitivity range from 900 nm to 1750 nm, a resolution of 320 x 256 pixels and an InfiniMite™ lens (Infinity, Boulder, CO, USA) was used to acquire images during the dehydration process. The area per pixel was approximately 0.003 mm². Light from a 150 W fiber-optic illuminator FOI-1 (E Licht Company, Denver, CO, USA) was directed at the sample at an incident angle of approximately 60 ° in order to reduce specular reflection as shown in the first figure of reference (Lee et al. 2015). Several band-pass (BP) and long-pass (LP) filters were used to provide different spectral distributions of NIR light: band-pass filters centered at 1300 nm with 90 nm bandwidth (1260–1340 nm), 1460 nm with 85 nm bandwidth (1420–1500 nm) (Spectrogon, Parsippany, NJ, USA) and long-pass filters at 1400 nm (1400–1700 nm) and 1500 nm (1500–1700 nm), FEL LP series from (Thorlabs, Newton, NJ, USA). Source to sample distance was fixed at 5 cm for all samples.

NIR reflectance images were processed and automatically analyzed using a dedicated program constructed with LabView™ software. A 5 × 5 pixel ROI was specified for each window and an average measurement was recorded for each time point. The image contrast was calculated using $(I_L - I_S)/I_L$ of the final image, where I_S is the mean intensity of the sound dentin and I_L is the mean intensity of the lesion. In addition to lesion contrast, the intensity difference, ΔI , was calculated by taking the difference of the mean intensity before and after the dehydration process.

6.3.8 Polarized Light Microscopy (PLM) and Transverse Microradiography (TMR)

After sample imaging was completed, 230 μm thick serial sections were cut using an Isomet 5000 saw (Buehler, IL, USA) for polarized light microscopy (PLM) and transverse microradiography (TMR). PLM was carried out using a Meiji Techno Model RZT microscope (Meiji Techno Co., LTD, Saitama, Japan) with an integrated digital camera, Canon EOS Digital Rebel XT (Canon Inc., Tokyo, Japan). The sample sections were imbedded in water and examined in the brightfield mode with crossed polarizers and a red I plate with 500 nm retardation. PLM images were acquired at 40x magnification and had a resolution of 3264 x 2448 pixels.

A custom built digital microradiography (TMR) system was used to measure the volume percent mineral content in the areas of demineralization on the tooth sections (Darling et al. 2009). High-resolution microradiographs were taken using $\text{Cu K}\alpha$ radiation from a Philips 3100 X-ray generator and a Photonics Science FDI X-ray digital imager, Microphotonics (Allentown, PA, USA). The X-ray digital imager consisted of a 1392 \times 1040 pixel interline CCD directly bonded to a coherent micro fiber-optic coupler that transfers the light from an optimized gadolinium oxysulfide scintillator to the CCD sensor. The pixel resolution was 2.1 μm and the images were acquired at 10 frames per second. A high-speed motion control system with Newport UTM150 and 850G stages and an ESP 300 controller coupled to a video microscopy and a laser targeting system was used for precise positioning of the sample in the field of view of the imaging system. Shrinkage also confounds measurement of the integrated mineral loss. The effect of shrinkage can be compensated for in TMR by equating the depth of shrinkage with an equivalent loss of sound dentin for the simulated dentin lesion samples. Line profiles

were integrated from the surface of the lesion to a depth of 150 μm subtracted by the depth of the shrinkage to ensure that the effective integrated volume was the same between zones that exhibited shrinkage and those zones did not.

6.3.9 Histological Validation of Lesion Activity of Natural Root Caries Lesions

PLM was used to record the location of caries lesions, the presence of an intact cementum layer and irregular surface defects such as cavitation, and TMR was used to measure changes in mineral content. If a surface layer of a similar or higher mineral content of sound dentin was present, the activity of the suspected lesion was categorized as “arrested”. If there was cavitation without any signs of caries activity (i.e., loss of mineral at surface of the lesion), the lesion was classified as a “non-carious cervical lesion”. If the lesion did not have the surface layer or had a significant loss in mineral content with a discontinuity of the surface layer, the lesion was categorized as “active”.

6.3.10 Statistical Analysis

Groups of the simulated dentin lesion samples were compared using repeated measures analysis of variance (ANOVA) with a Tukey–Kramer post hoc multiple comparison test. The natural root caries lesion samples were divided into two groups based on their histological assessment (section 6.3.2): active and non-active lesions. Imaging methods were evaluated using a paired t-test (two-tailed) and receiver operating characteristic (ROC) curves. All statistical analyses were performed with 95% confidence with PrismTM (GraphPad software, San Diego, CA).

6.4 RESULTS

6.4.1 Simulated Dentin Lesions

Figure 6.2 shows the visible, PLM, TMR and PS-OCT images of a simulated dentin lesion sample from the initial 24-hour demineralization group after exposure to the remineralization solution. Unlike enamel lesions, the windows exposed to the demineralization or the remineralization solution could not be easily discriminated from the sound window by visual examination as shown in **Fig. 6.2A**. The changes to the subsurface mineral structure upon demineralization and remineralization could be seen with PLM and TMR as shown in **Figs. 6.2B and 6.2C**. There was an increase in lesion depth measured with PLM even though there was a decrease in mineral loss with increasing periods of remineralization as shown in **Table 6.1**. The highly mineralized surface layer was often difficult to distinguish from demineralization with PLM. TMR showed an increase in mineral density at the surface of the lesion with increasing periods of exposure to the remineralization solution. The acidic pH remineralization model produced increased mineralization in the lesion body in a similar fashion to what has been observed for enamel samples (Lee et al. 2015).

In our previous study, the algorithm successfully detected the surface layer in enamel with high sensitivity and specificity (Lee et al. 2014). In this work, the algorithm was optimized for dentin and it was able to detect increased remineralization in the simulated dentin lesion samples with increasing periods of exposure to the remineralization solution as shown in **Figs. 6.2D and 6.2E** and **Table 6.1**. The modified algorithm was able to detect remineralization successfully without any false positives and false negatives; there were a total of 150 windows from 30 samples, with 90 true

positives and 60 true negatives. The thickness measurements of the surface layer with PS-OCT could not be accurately validated with histology due to the high opacity of dentin in PLM images and the absence of a distinct sharp edge to the highly mineralized surface layer in TMR images (Lee et al. 2009).

There was considerable shrinkage in the windows that were treated with the demineralization solution in the TMR and PS-OCT images (**Figs. 6.2C and 6.2D**). The degree of shrinkage decreased with increasing exposure to the remineralization solution with an exception of the remineralization control group as shown in **Table 6.1**. Both ΔR and the ΔZ decreased with exposure to increasing periods of remineralization for both the initial 24-hour and 8-hour demineralization models.

The time-temperature profiles of the sample from **Fig. 6.2** are shown in **Fig. 6.3A**. With air-drying, most samples approached ambient temperature within 30 seconds. **Figure 6.3A** shows that the lesion window exhibited the greatest temperature drop within the first 5 seconds of air-drying and manifested the slowest recovery to equilibrium. However, the magnitude of the temperature drop and the recovery time to ambient temperature decreased significantly with exposure to increasing periods of remineralization. In addition, the remineralization control window that was only treated with the remineralization solution underwent a marked reduction in ΔQ compared to the sound window. The ΔQ measurements are shown in **Fig. 6.3B** and **Table 6.1**.

NIR time-intensity difference profiles acquired at 1400 – 1700 nm wavelengths for the sample shown in **Fig. 6.2** are shown in **Fig. 6.4A**. The intensity difference, ΔI , was recorded instead of raw intensity data due to differences in anatomic structure of the sample, i.e. variation in depth to pulp chamber, presence of cracks, orientation and

size of dentinal tubules and organic content of the tissue. As seen in **Fig. 6.4B** and **Table 6.1**, the lesion contrast and the ΔI measurements for NIR reflectance did not manifest a significant reduction among groups as the sample was treated with increasing periods of remineralization. In addition, the lesion contrast and ΔI increased after exposure to the first 4-day period of remineralization. The samples were also imaged at different wavelengths and yielded similar measurements producing no significant changes with increasing periods of remineralization.

6.4.2 Natural Root Caries Lesions

Two trained clinician examiners relied on the ICDAS II lesion assessment system, which utilizes color (light/dark brown, black), texture (smooth, rough), appearance (shiny or glossy, matte or non-glossy), perception on gentle probing (soft, leathery, hard) and cavitation (loss of anatomic contour). The inter-examiner agreement was 80% agreement of diagnosis with a kappa value of 0.53, which is considered to be moderate in the strength of agreement. With the true-positive being the successful diagnosis of an active lesion, the two examiners yielded an average sensitivity of 0.38 and an average specificity of 0.83.

Images of a natural root caries lesion are shown in **Fig. 6.5**. The visible image (**Fig. 6.5A**) shows a cervical root caries lesion that is both light and dark brown in color, both smooth and rough in texture, both matte and non-glossy in appearance, and both soft and hard in perception on gentle probing with the presence of cavitation. PLM images (**Figs. 6.5G and 6.5H**) show anatomical structural loss, yet they do not show a distinct surface zone indicative of an arrested lesion. TMR images (**Figs. 6.5I and 6.5J**)

show a significant difference in mineral content between two sections and it is evident that the highly mineralized surface layer is present in **Fig. 6.5J**. PS-OCT images (**Figs. 6.5B – 6.5D**) accurately estimated the lesion severity and detected the presence of the highly mineralized surface layer. The NIR reflectance image (**Fig. 6.5E**) shows localized areas of high ΔI values while thermal image (**Fig. 6.5F**) shows different localized areas of high ΔQ values.

Lesion activity assessment via detection of the presence of a highly mineralized surface layer with PS-OCT yielded a sensitivity of 0.81 and a specificity of 0.67 for the natural root caries lesions. In addition, the lesion severity, ΔR , from PS-OCT was also evaluated for the root caries lesion activity assessment. The diagnostic performance of ΔR from PS-OCT, ΔI from NIR reflectance imaging and ΔQ from thermal imaging were also evaluated for the lesion activity assessment of natural root caries lesions. As shown in **Fig. 6.6** and **Table 6.2**, only the ΔQ measurements showed the significant differences between active and non-active lesion groups ($P < 0.0001$) from both t-test and ROC curve analyses.

6.5 DISCUSSION

The purpose of this work was to determine whether PS-OCT, NIR reflectance and thermal imaging methods could be used to non-destructively assess lesion activity on root surfaces. In order to simulate the complex process of demineralization and remineralization that occurs in the oral cavity, we used an acidic pH remineralization model that is designed to repair the existing crystal remnants in lesions (Yamazaki and Margolis 2008). In a previous dentin remineralization study, a neutral pH

remineralization model was used and there was superficial deposition of new mineral at the surface of the dentin lesion with minimal mineralization of the lesion body (Manesh et al. 2009). This model yielded far greater success in generating the highly mineralized surface layer compared to the neutral pH remineralization model; all windows of the simulated dentin lesion samples that were treated with both the demineralization and acidic remineralization solution yielded highly mineralized surface layers. The acidic pH remineralization model successfully remineralized artificial dentin lesions without producing superficial mineral deposition on the lesion surface, which was observed in a previous study (Manesh et al. 2009). The increase in mineral density and the decrease in shrinkage with this acidic remineralization treatment show that this acidic remineralization model was successful as shown in **Fig. 6.2** and **Table 6.1**. It has been shown that demineralized dentin exhibits considerable shrinkage if not immersed in water due to the high percentage of collagen and the amount of shrinkage in demineralized dentin is proportional to the integrated mineral loss, ΔZ . (Lee et al. 2009). However, this acidic remineralization model did produce an increase in the lesion depth with longer periods of remineralization. It is likely that this model initially induces further demineralization in the lesion body until fluorapatite deposition begins to form the surface layer inhibiting diffusion. PLM image (**Fig. 6.2B**) of the simulated dentin lesion sample shows that the windows treated with both the demineralization and acidic remineralization solutions have lesion depths greater than the initial lesion window, while the remineralization control window appears unaffected by the remineralization solution. One can speculate that the permeability of the demineralized dentin is much

higher than that of sound dentin, which can lead to the acceleration of demineralization before diffusion is inhibited by the remineralization process.

The algorithm for automatic assessment of remineralization was successfully modified and applied to the PS-OCT images of the simulated dentin lesion samples to accommodate for the different refractive index (1.5) and higher scattering and absorption coefficients of dentin. The algorithm was able to detect and measure the highly mineralized surface layer automatically (**Figs. 6.2D – 6.2E**). The measurements of ΔR and thickness of the highly mineralized surface layer suggested that they could be used to nondestructively measure lesion severity, remineralization and the activity of root caries lesions.

However, the performance of the modified PS-OCT algorithm was not as high for the natural root caries lesions. The algorithm yielded a much higher sensitivity but with a lower specificity compared to the conventional root caries lesion assessment methods recommended by ICDAS II. There were several characteristics of natural root caries lesion samples that led to a significant decrease in the diagnostic performance of the algorithm. Healthy root dentin is typically encapsulated by the cementum layer, which can be mistaken for the surface layer if there is an active lesion underlying the cementum layer, and the cementum layer is significantly more acid resistant than the underlying dentin (McIntyre et al. 2000). In addition, dentin and cementum are significantly weaker than enamel; their structural integrity can be much more easily compromised due to acid erosion, caries activity and mechanical abrasions (Malek et al. 2001, Kinney et al. 2003). There was generalized loss of the cementum layer centered on the suspected root caries lesions and they were often accompanied with loss of

dentin structure as well. Edges of the surrounding cementum layer appeared sharp when examined with histology and increased the reflectivity and scattering of NIR light resulting in false positives.

In a previous study, we reported that the highly mineralized surface layer plays an important role in the dehydration process of remineralized enamel lesions and that both the thermal and NIR imaging methods are suitable for detection of remineralization (Lee et al. 2015). In this work, only ΔQ decreased as the simulated dentin lesion was exposed to the remineralization solution. Unlike the enamel lesions, which showed no significant differences in ΔQ between individual remineralization windows or between sound and remineralization windows, there were significant differences in ΔQ among different windows as shown in **Fig. 6.3B** and **Table 6.1**. Another major difference is that the remineralization control window showed a large change in ΔQ compared to the sound window. This suggests that the dentinal tubules on the sound dentin surface were successfully occluded, i.e., filled with new mineral from the acidic remineralization treatment. Although there were no histological changes between the sound and the remineralization control windows in the PLM, TMR and PS-OCT analyses (**Fig. 6.2** and **Table 6.1**), there was an obvious change in thermodynamic behavior during the dehydration process. This result shows a potential application of the acidic remineralization regime for addressing dentin hypersensitivity.

We expected the NIR lesion contrast and ΔI to decrease as the lesion was exposed to the remineralization solution. Instead of a reduction in the NIR lesion contrast and ΔI , there was a significant increase after 4 days of remineralization followed by a decreasing trend in NIR lesion contrast and ΔI measurements with further

remineralization as shown in **Fig. 6.4** and **Table 6.1**. Because the lesion was more severe for the 4-day remineralization window than the lesion window itself, the lesion contrast and intensity difference measurements of the 4-day remineralization window appeared significantly higher after dehydration compared to those of the initial lesion.

Thermal imaging (ΔQ) yielded the strongest diagnostic performance for assessment of the natural root caries lesions while NIR reflectance (ΔI) did not perform well. Regardless of the presence of the surface layer, ΔI was highly dependent on the underlying lesion severity. However, the ΔQ values were low, independent of the severity of the underlying lesion, if the surface layer was present. Sound root surfaces yielded low ΔQ values, most likely due to the presence of the cementum layer and occlusion of dentinal tubules from the continued exposure to the oral environment. In addition, ΔQ was not affected by the structural variations of the root surface; presence of cementum or cavitation due to abrasion did not influence ΔQ measurements.

Clinical implication of these new techniques should be straightforward. Thermal cameras have been miniaturized to the point that they are now available as attachments for cell phones. Although the dehydration and imaging setup used in this work may not be feasible in clinical practice due to its large size, each component can be miniaturized and integrated into a single handpiece to fit into a person's mouth. The duration of the measurement can be also significantly reduced by increasing the pressure of the air and positioning air nozzles closer to the sample. Further research is required to evaluate the clinical feasibility of the new techniques for assessment of root caries lesion activity.

6.6 CONCLUSION

This work demonstrates that the infrared imaging modalities can be used to non-destructively assess root caries lesion activity. A modified PS-OCT algorithm for the automated assessment of remineralization was successful for discriminating between active and non-active root caries lesions. In addition, the highly mineralized surface layer plays an important role in the dehydration process of remineralized dentin lesions. Thermal imaging provided the best performance in root caries lesion activity assessment. NIR based imaging modalities, PS-OCT and NIR reflectance imaging, were extremely sensitive to anatomic structural variations and lesion severity. However, NIR reflectance imaging was not suitable for root caries lesion activity assessment because there was not a significant reduction in intensity with the presence of a surface layer. Therefore, PS-OCT and thermal imaging performed best for monitoring the activity of root caries lesions unlike in our earlier study on enamel lesions that yielded the highest performance for NIR reflectance imaging. Detection of remineralization with these novel methods is highly promising and extremely important for the clinical assessment of root caries lesion activity.

6.7 FIGURES AND FIGURE LEGENDS

Table 6.1 Mean \pm S.D. of PS-OCT, PLM, TMR, Δ Q from thermal imaging and NIR reflectance measurements at 1400 – 1700 nm wavelength for the 8 and 24-hour demineralization groups of the simulated dentin lesion samples. Groups with the same letters are statistically similar, $P > 0.05$ in each row ($n = 15$).

	Sound	Lesion	4-day Remin	8-day Remin	12-day Remin	Remin Control
24-hour demineralization (n=15)						
Surface Layer Thickness (PS-OCT, μm)	0 a	0 a	44 \pm 13 b	49 \pm 12 bc	54 \pm 13 c	4 \pm 10 a
Shrinkage (PS-OCT, μm)	0 a	40 \pm 12 b	30 \pm 14 c	29 \pm 14 c	25 \pm 11 c	0 \pm 6 a
Integrated Reflectivity, Δ R (dB \times μm)	0 a	2100 \pm 460 b	1660 \pm 320 c	1730 \pm 400 c	1600 \pm 380 c	30 \pm 110 a
Lesion Depth (PLM, μm)	0 a	58 \pm 10 b	78 \pm 13 c	92 \pm 14 d	110 \pm 26 e	1 \pm 5 a
Integrated Mineral Loss, Δ Z (vol% \times μm)	0 a	2140 \pm 380 b	1930 \pm 440 c	1820 \pm 420 d	1580 \pm 310 e	140 \pm 380 a
Δ Q (K \times s)	39 \pm 14 a	49 \pm 21 b	30 \pm 19 ac	25 \pm 15 c	21 \pm 12 c	13 \pm 9 d
NIR Contrast	-	0.3 \pm 0.2 ac	0.5 \pm 0.2 b	0.4 \pm 0.2 a	0.3 \pm 0.3 a	-0.2 \pm 0.7 c
Δ I(t=30)	215 \pm 124 a	372 \pm 244 b	512 \pm 244 c	447 \pm 237 bc	366 \pm 203 b	112 \pm 69 d
8-hour demineralization (n=15)						
Surface Layer Thickness (PS-OCT, μm)	0 a	0 a	34 \pm 12 b	35 \pm 10 b	39 \pm 13 b	4 \pm 11 a
Shrinkage (PS-OCT, μm)	0 a	20 \pm 5 b	11 \pm 6 c	9 \pm 6 d	8 \pm 5 d	0 \pm 3 a
Integrated Reflectivity, Δ R (dB \times μm)	0 a	1450 \pm 170 b	1130 \pm 180 c	1150 \pm 200 c	1080 \pm 150 c	90 \pm 190 a
Lesion Depth (PLM, μm)	0 a	34 \pm 4 b	61 \pm 8 c	74 \pm 10 d	79 \pm 18 d	5 \pm 10 a
Integrated Mineral Loss, Δ Z (vol% \times μm)	0 a	1060 \pm 270 b	770 \pm 290 c	640 \pm 250 d	520 \pm 250 e	80 \pm 270 a
Δ Q (K \times s)	29 \pm 14 a	35 \pm 8 b	14 \pm 7 c	11 \pm 7 c	12 \pm 7 c	10 \pm 3 c
NIR Contrast	-	0.3 \pm 0.2 ac	0.4 \pm 0.2 b	0.4 \pm 0.2 a	0.4 \pm 0.3 a	0.1 \pm 0.4 c
Δ I(t=30)	185 \pm 134 ac	286 \pm 130 b	319 \pm 186 ab	320 \pm 199 ab	279 \pm 195 ab	133 \pm 64 c

Table 6.2 Mean \pm S.D. and P-values for PS-OCT ΔR , NIR reflectance ΔI at 1400 – 1700 nm wavelength and thermal ΔQ measurements of the natural root caries lesion samples.

	Active (n = 16)	Non-Active (n = 9)	P-value
ΔR (dB \times μm)	835 \pm 538	591 \pm 351	0.2360
$\Delta I(t=60)$	169 \pm 181	103 \pm 116	0.3377
ΔQ (K \times s)	18.6 \pm 18.7	0.7 \pm 0.7	< 0.0001

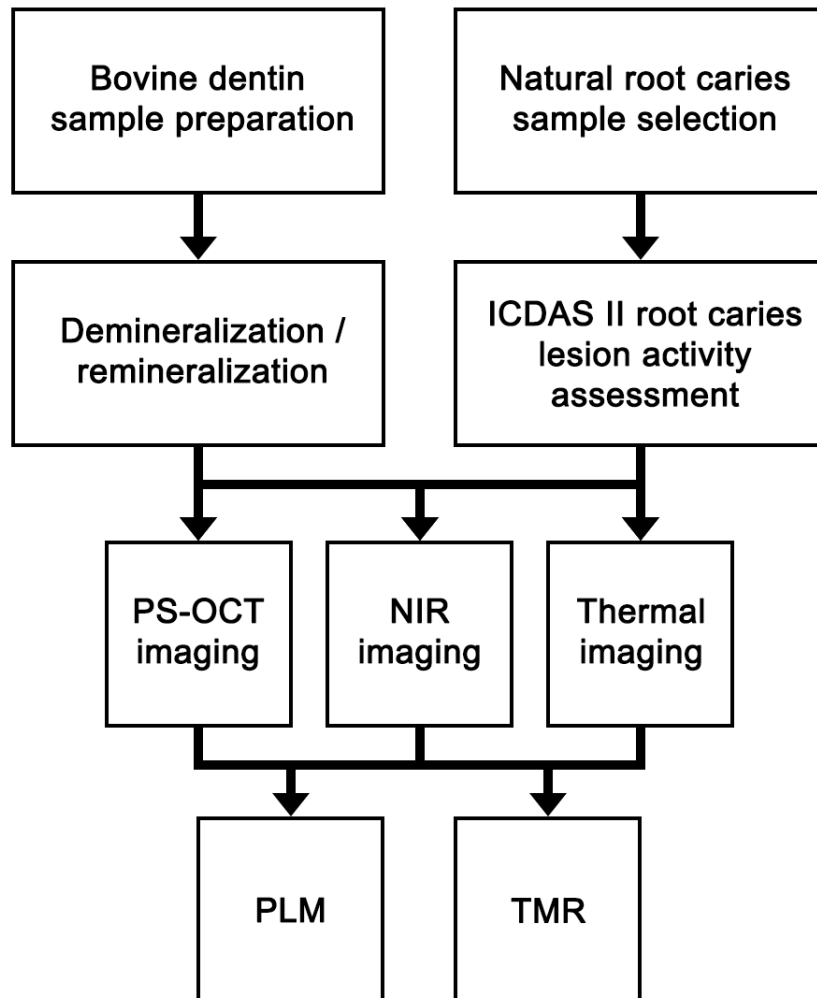


Figure 6.1 Flowchart of the study design.

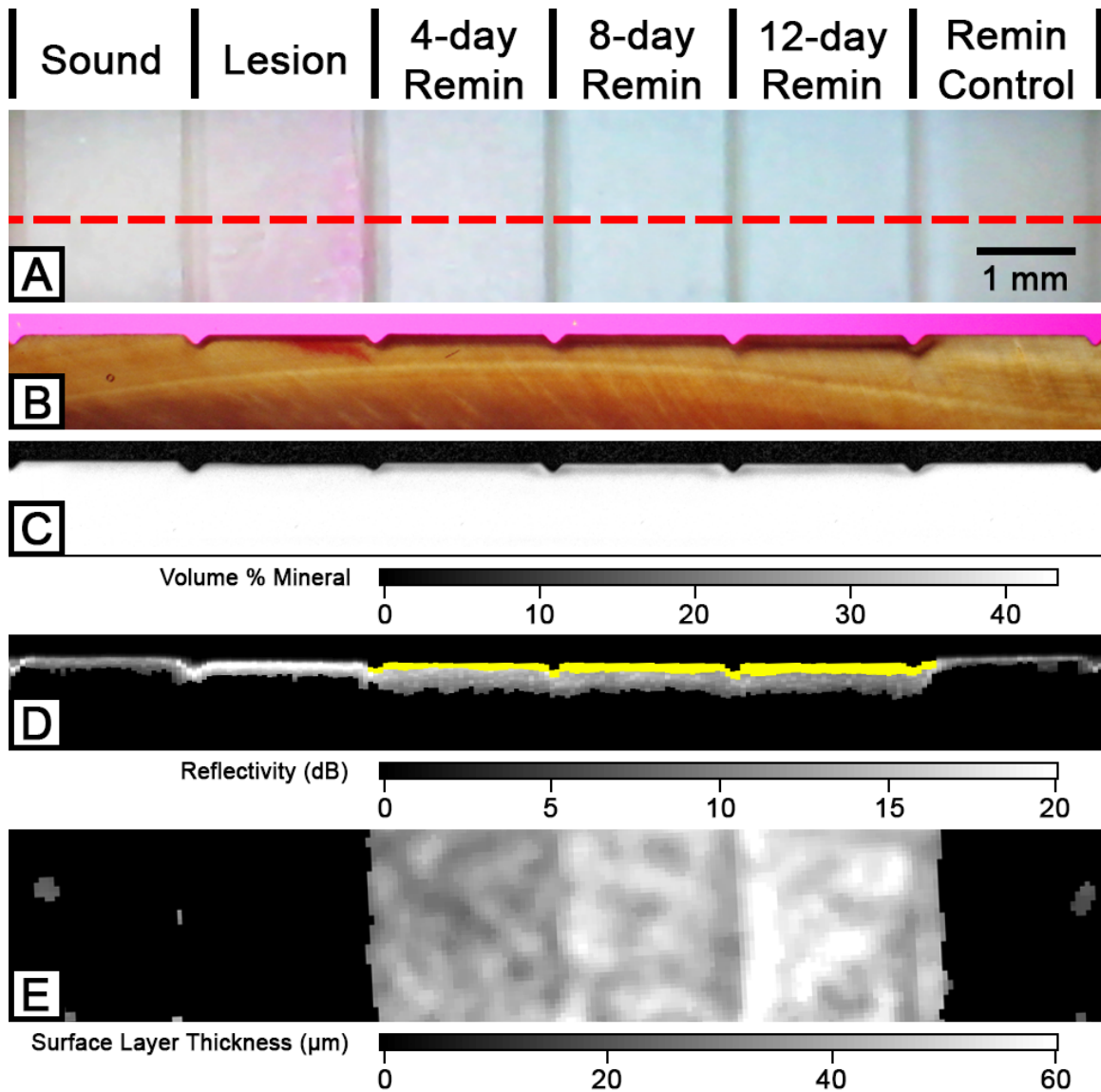


Figure 6.2 Two-dimensional projection and cross-sectional PLM, TMR and PS-OCT images of the six windows on a 24-hour demineralization sample. The red dotted line in the visible light reflectance image (A) represents the position of the section shown in (B), (C) and (D). PLM (B), TMR (C) and processed PS-OCT B-scan (D) images show an increase in transparent surface layer thickness over the periods of exposure to the remineralization solution. The transparent surface layer is highlighted in yellow (D) and shown in the 2D OCT surface projection images (E).

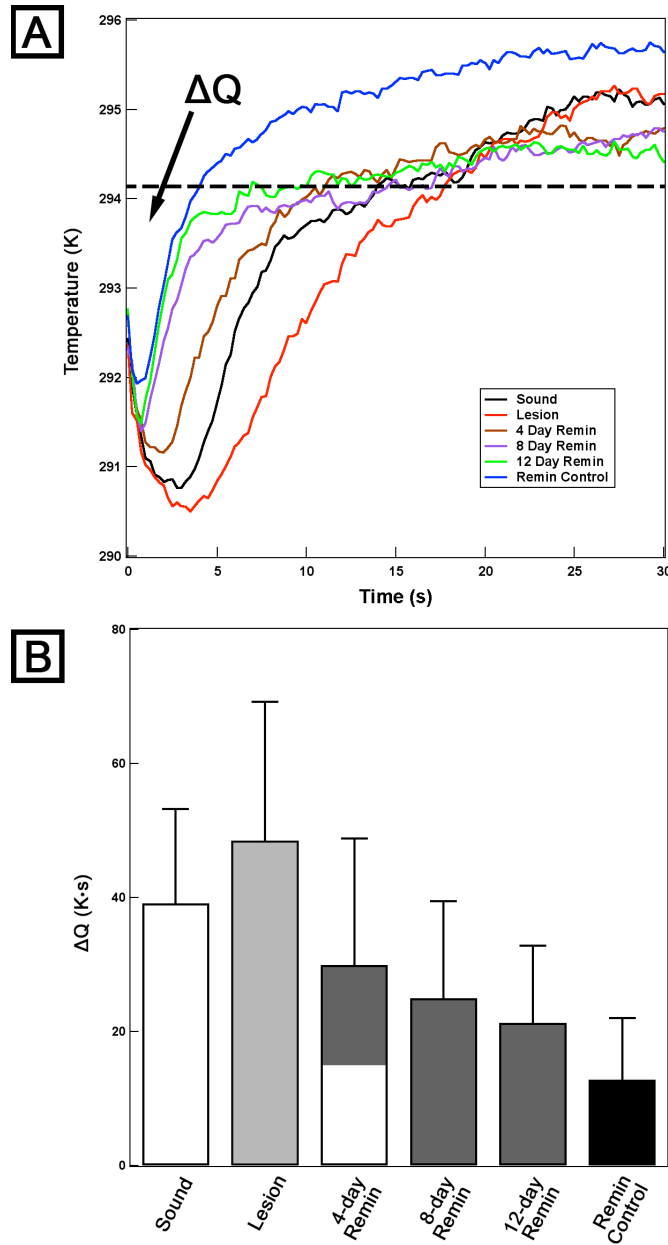


Figure 6.3 Typical time-temperature profiles (A) over 30 seconds for the simulated dentin lesion sample shown in **Fig. 6.2**. Mean \pm S.D. ΔQ measurements (B) of the 24-hour demineralization samples. Dashed line (A) represents the initial temperature and ΔQ is the area under the dashed line enclosed by the time-temperature curve. Bars not sharing any common colors were significantly different, $P < 0.05$ ($n = 15$).

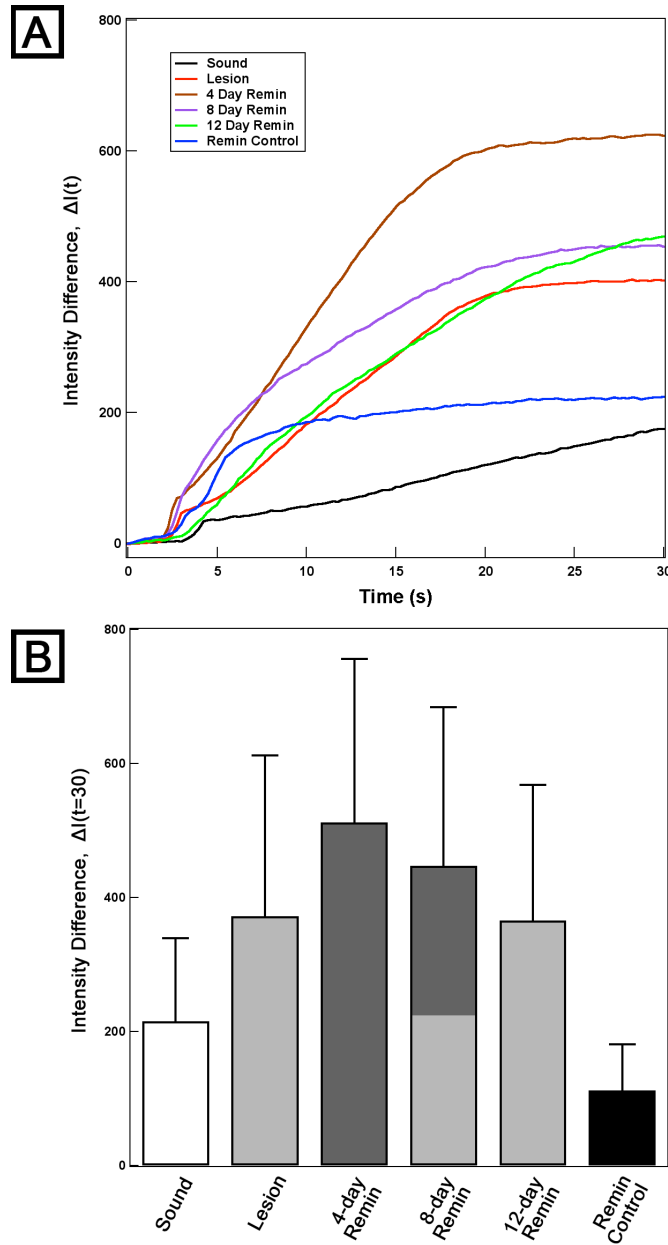


Figure 6.4 Typical time-NIR reflectance intensity difference profiles (A) with a 1400 nm long-pass filter over 30 seconds for the simulated dentin lesion sample shown in **Fig. 6.2**. Mean \pm S.D. ΔI measurements (B) of the 24-hour demineralization samples. Bars not sharing any common colors were significantly different, $P < 0.05$ ($n = 15$).

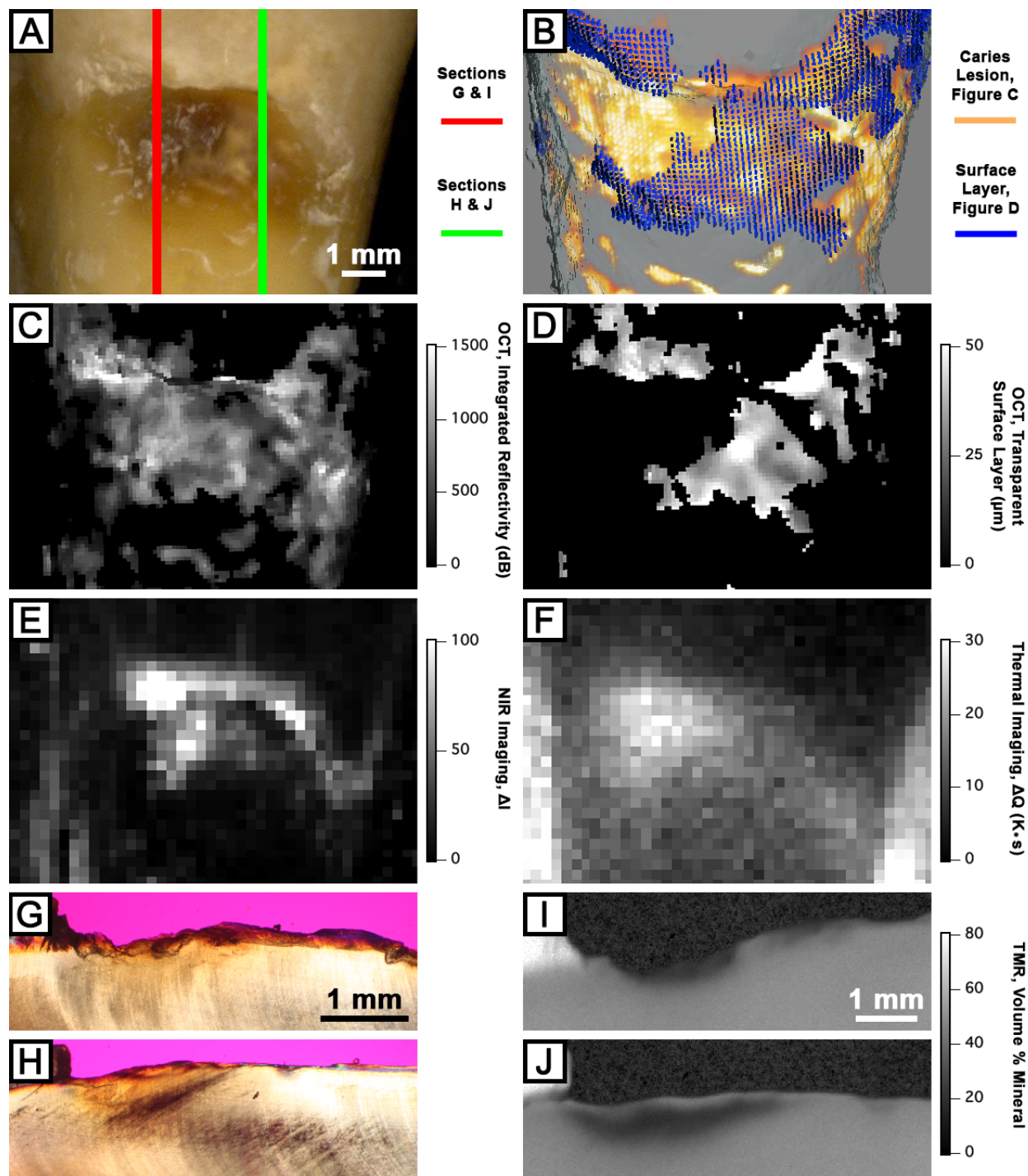


Figure 6.5 Visible (A), PS-OCT (B – D), NIR reflectance (E) and thermal (F) images and cross-sectional PLM and TMR images of a natural root caries lesion sample. Three-dimensional composite image (B) of processed PS-OCT images (C and D) shows the

surface layer (blue) covering the underlying lesion body (orange) The red line (A) represents the active portion of the root caries lesion as shown in sections (G) and (I), and the green line (A) represents the arrested portion of the root caries lesion as shown in sections (H) and (J).

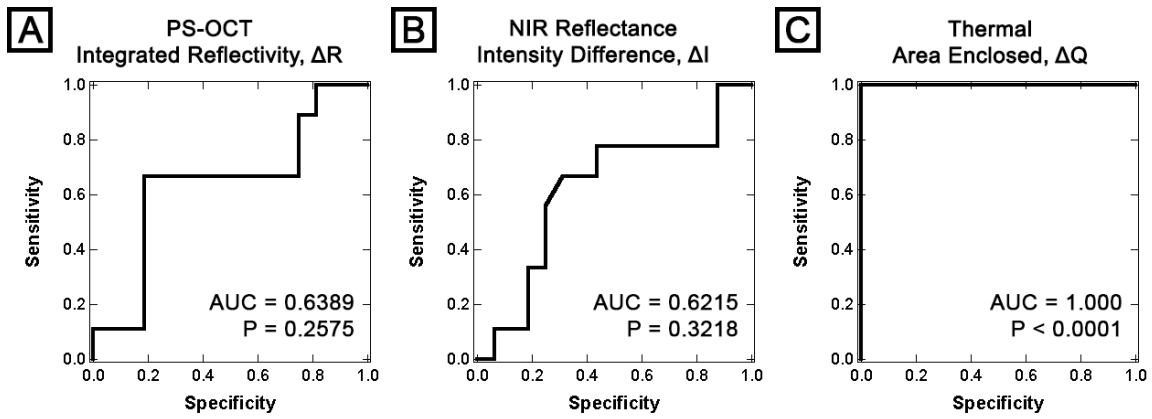


Figure 6.6 ROC curve analysis of three imaging modalities: PS-OCT ΔR (A), NIR reflectance ΔI (B) and Thermal ΔQ (C) measurements of the natural root caries lesion samples. AUC represents the area under the curve.

6.8 REFERENCES

- Ando, M., Sharp, N. and Adams, D. (2012). Pulse thermography for quantitative nondestructive evaluation of sound, de-mineralized and re-mineralized enamel. *Proc. SPIE Health Monitoring of Structural and Biological Systems I*, San Diego, CA, **8348**: S1-7.
- Banting, D., Eggertsson, H., Ekstrand, K. R., Ferreira-Zandona, A., Ismail, A. I., Longbottom, C., Pitts, N., Reich, E., Ricketts, D., Selwitz, R., Sohn, W., Topping, G. and Zero, D. (2005). Rationale and evidence for the International Caries Detection and Assessment System (ICDAS II). *Proc. the 7th Annual Indiana Conference: Clinical Models Workshop: Remin-Demin, Precavitation, Caries*, Indianapolis, IN, 161-221.
- Bignozzi, I., Crea, A., Capri, D., Littarru, C., Lajolo, C. and Tatakis, D. N. (2014). Root caries: a periodontal perspective. *J. Periodontal Res.*, **49**(2): 143-163.
- Brannstrom, M. (1966). Sensitivity of dentine. *Oral Surg. Oral Med. Oral Pathol.*, **21**(4): 517-526.
- Bush, J., Davis, P. and Marcus, M. A. (2000). All-fiber optic coherence domain interferometric techniques. *Proc. SPIE Fiber Optic Sensor Technology II*, San Jose, CA, **4204**: 71-80.
- Canadian Advisory Board on Dentin Hypersensitivity (2003). Consensus-based recommendations for the diagnosis and management of dentin hypersensitivity. *J. Can. Dent. Assoc.*, **69**(4): 221-226.
- Can, A. M., Darling, C. L. and Fried, D. (2008). High-resolution PS-OCT of enamel remineralization. *Proc. SPIE Lasers in Dentistry XIV*, San Jose, CA, **6843**: T1-7.
- Darling, C. L., Featherstone, J. D. B., Le, C. Q. and Fried, D. (2009). An automated digital microradiography system for assessing tooth demineralization. *Proc. SPIE Lasers in Dentistry VX*, San Jose, CA, **7162**: T1-7.
- Darling, C. L., Huynh, G. D. and Fried, D. (2006). Light scattering properties of natural and artificially demineralized dental enamel at 1310 nm. *J. Biomed. Opt.*, **11**(3): 34023.
- Ekstrand, K., Martignon, S. and Holm-Pedersen, P. (2008). Development and evaluation of two root caries controlling programmes for home-based frail people older than 75 years. *Gerodontology*, **25**(2): 67-75.
- Everett, M. J., Colston, B. W., Sathyam, U. S., Silva, L. B. D., Fried, D. and Featherstone, J. D. B. (1999). Non-invasive diagnosis of early caries with polarization sensitive optical coherence tomography (PS-OCT). *Proc. SPIE Lasers in Dentistry V*, San Jose, CA, **3593**: 177-182.

- Fejerskov, O. and Kidd, E., Eds. (2003). Dental caries: the disease and its clinical management. Oxford, Blackwell.
- Fried, D., Xie, J., Shafi, S., Featherstone, J. D. B., Breunig, T. M. and Le, C. Q. (2002). Early detection of dental caries and lesion progression with polarization sensitive optical coherence tomography. *J. Biomed. Opt.*, **7**(4): 618-627.
- Holland, G. R., Narhi, M. N., Addy, M., Gangarosa, L. and Orchardson, R. (1997). Guidelines for the design and conduct of clinical trials on dentine hypersensitivity. *J. Clin Periodontol.*, **24**(11): 808-813.
- Jones, R. S., Darling, C. L., Featherstone, J. D. B. and Fried, D. (2006). Imaging artificial caries on the occlusal surfaces with polarization-sensitive optical coherence tomography. *Caries Res.*, **40**(2): 81-89.
- Kaneko, K., Matsuyama, K. and Nakashima, S. (1999). Quantification of early carious enamel lesions by using an infrared camera. *Proc. the 4th Annual Indiana Conference: Early Detection of dental caries II*, Indianapolis, IN, 83-99.
- Kawasaki, K. and Featherstone, J. D. (1997). Effects of collagenase on root demineralization. *J. Dent. Res.*, **76**(1): 588-595.
- Kinney, J. H., Balooch, M., Marshall, G. W. and Marshall, S. J. (1993). Atomic-force microscopic study of dimensional changes in human dentine during drying. *Arch. Oral Biol.*, **38**(11): 1003-1007.
- Kinney, J. H., Marshall, S. J. and Marshall, G. W. (2003). The mechanical properties of human dentin: a critical review and re-evaluation of the dental literature. *Crit. Rev. Oral Biol. Med.*, **14**(1): 13-29.
- Lee, C., Darling, C. L. and Fried, D. (2009). Polarization-sensitive optical coherence tomographic imaging of artificial demineralization on exposed surfaces of tooth roots. *Dent. Mater.*, **25**(6): 721-728.
- Lee, R. C., Darling, C. L. and Fried, D. (2014). Automated detection of remineralization in simulated enamel lesions with PS-OCT. *SPIE Lasers in Dentistry XX*, San Jose, CA, **8929**: E1-8.
- Lee, R. C., Darling, C. L. and Fried, D. (2015). Assessment of remineralization via measurement of dehydration rates with thermal and near-IR reflectance imaging. *J. Dent.*, **43**(8): 1032-1042.
- Lee, R. C., Kang, H., Darling, C. L. and Fried, D. (2014). Automated assessment of the remineralization of artificial enamel lesions with polarization-sensitive optical coherence tomography. *Biomed. Opt. Express*, **5**(9): 2950-2962.

- Lin, M., Liu, Q. D., Xu, F., Bai, B. F. and Lu, T. J. (2009). In vitro investigation of heat transfer in human tooth. *Proc. SPIE Experimental Mechanics IV*, Singapore, Singapore, **7522**: N1-7.
- Lynch, E. and Beighton, D. (1994). A comparison of primary root caries lesions classified according to colour. *Caries Res.*, **28**(4): 233-239.
- Malek, S., Darendeliler, M. A. and Swain, M. V. (2001). Physical properties of root cementum: Part I. A new method for 3-dimensional evaluation. *Am. J. Orthod. Dentofacial Orthop.*, **120**(2): 198-208.
- Manesh, S. K., Darling, C. L. and Fried, D. (2009). Polarization-sensitive optical coherence tomography for the nondestructive assessment of the remineralization of dentin. *J. Biomed. Opt.*, **14**(4): 044002.
- McIntyre, J. M., Featherstone, J. D. and Fu, J. (2000). Studies of dental root surface caries. 2: The role of cementum in root surface caries. *Aust. Dent. J.*, **45**(2): 97-102.
- Ngaotheppitak, P., Darling, C. L. and Fried, D. (2005). Measurement of the severity of natural smooth surface (interproximal) caries lesions with polarization sensitive optical coherence tomography. *Lasers Surg. Med.*, **37**(1): 78-88.
- Ozok, A. R., Wu, M. K., ten Cate, J. M. and Wesselink, P. R. (2002). Effect of perfusion with water on demineralization of human dentin in vitro. *J. Dent. Res.*, **81**(11): 733-737.
- Sumney, D. L., Jordan, H. V. and Englander, H. R. (1973). The prevalence of root surface caries in selected populations. *J. Periodontol.*, **44**(8): 500-504.
- Tugnait, A. and Clerehugh, V. (2001). Gingival recession-its significance and management. *J. Dent.*, **29**(6): 381-394.
- Usenik, P., Bürmen, M., Fidler, A., Pernuš, F. and Likar, B. (2014). Near-infrared hyperspectral imaging of water evaporation dynamics for early detection of incipient caries. *J. Dent.*, **42**(10):1242-1247.
- West, N. X., Lussi, A., Seong, J. and Hellwig, E. (2013). Dentin hypersensitivity: pain mechanisms and aetiology of exposed cervical dentin. *Clin. Oral Investig.*, **17**(S1): 9-19.
- Yamazaki, H. and Margolis, H. C. (2008). Enhanced enamel remineralization under acidic conditions in vitro. *J. Dent. Res.*, **87**(6): 569-574.
- Zakian, C., Pretty, I. and Ellwood, R. (2009). Near-infrared hyperspectral imaging of teeth for dental caries detection. *J. Biomed. Opt.*, **14**(6): 064047.
- Zakian, C. M., Taylor, A. M., Ellwood, R. P. and Pretty, I. A. (2010). Occlusal caries detection by using thermal imaging. *J. Dent.*, **38**(10): 788-795.

CHAPTER VII

SUMMARY AND FUTURE PERSPECTIVE

7.1 SUMMARY

New diagnostic methods are needed to accurately assess lesion activity and avoid unnecessary cavity preparations. Conventional methods for caries lesion activity assessment are composed of visual and tactile exams and suffer from poor diagnostic performance due to their subjective nature (Ekstrand et al. 2009). The potential of infrared imaging methods to objectively assess caries lesion activity in a single examination has been demonstrated by the *in-vitro* experiments presented in this dissertation work. The following methods utilizing infrared methods were developed for the assessment of caries lesion activity: the highly mineralized surface layer detection with polarization-sensitive optical coherence tomography (PS-OCT), near-infrared (NIR) reflectance imaging with dehydration and thermal imaging with dehydration. These novel methods were tested on artificial and natural caries lesions on both coronal and root surfaces and were validated with histology.

7.1.1 Coronal Caries Lesion Activity Assessment

OCT has been heavily investigated as a non-invasive technique for creating cross-sectional images of dental tissue structures (Amaechi et al. 2001, Fried et al. 2002, Jones et al. 2006). The work in **chapter 2** describes the development of an algorithm for detection of the highly mineralized surface layer using the tomographic images acquired with PS-OCT. By analyzing both polarization axes, the algorithm had successfully detected the incident light surface reflection as well as the underlying lesion front and body, ultimately locating and measuring the thickness of the highly mineralized surface layer. This algorithm was further tested on in-vitro artificial enamel caries lesions and

yielded high sensitivity (= 0.92) and specificity (= 0.97) in **chapter 3**. It was demonstrated that PS-OCT could be used to nondestructively measure the changes in the artificial enamel lesion structure and severity upon exposure to remineralization solutions using two different models.

As the lesion becomes arrested or undergoes remineralization, the permeability of the lesion becomes diminished due to the presence of highly mineralized surface layer. The optical changes associated with dehydration at infrared wavelengths were investigated in **chapter 4**. Artificial enamel caries lesion samples were imaged using NIR reflectance and thermal imaging during the dehydration process. Both the thermal and NIR imaging methods were suitable for detection of remineralization, yet only NIR reflectance imaging at wavelengths between 1400 nm and 1700 nm was capable of detecting significant differences between different periods of remineralization as shown in **Figs. 4.5, 4.9 and 4.10**.

The three methods developed in **chapters 2, 3 and 4** were subsequently tested on natural occlusal and smooth surface enamel caries lesions and compared with the conventional methods in **chapter 5**. The diagnostic performance and the inter-examiner reliability of the conventional coronal caries lesion activity diagnostic method via ICDAS II were in general poor. PS-OCT coupled with the automated algorithm was effective in detection and measurement of the highly mineralized surface layer in natural coronal caries lesions (sensitivity: 0.79, specificity: 0.93 and $R^2 = 0.5920$). Images generated with PS-OCT provide useful information for estimating the severity and the degree of remineralization of the lesion. As expected, thermal and NIR reflectance imaging with dehydration were suitable for assessment of natural coronal caries lesion activity (**Table**

5.2). Most importantly, NIR reflectance imaging provided more localized and higher spatial resolution images compared to thermal imaging.

Conventional lesion activity assessment that relies on visual and tactile examination lacks certainty and reproducibility, and these experiments reinforce the importance of new methods with improved diagnostic performance in assessment of coronal caries lesion activity.

7.1.2 Root Caries Lesion Activity Assessment

In **chapter 6**, simulated root caries lesions and natural root caries lesions were evaluated with the methods introduced in the previous chapters. The simulated root caries lesions were produced using an acidic remineralization solution, which was applied to dentin for the first time. The algorithm introduced in **chapter 2** was modified to detect the highly mineralized surface layer in dentin samples. The modified algorithm was able to detect remineralization in simulated root caries lesions samples without any false positives and false negatives, yet it yielded a reduced sensitivity of 0.81 and a reduced specificity of 0.67 for the natural root caries lesion samples. The diagnostic performances of NIR reflectance and thermal imaging during the dehydration process can be found in **Tables 6.1 and 6.2** and **Fig. 6.6**. NIR reflectance imaging was not suitable for root caries lesion activity assessment because there was not a significant reduction in intensity with the presence of a surface layer in both groups of samples. It is speculated that NIR based imaging modalities, PS-OCT and NIR reflectance imaging, were extremely sensitive to anatomic structural variations and underlying lesion severity. Thermal imaging provided the best performance in root caries lesion activity

assessment for both groups of samples. Unlike NIR reflectance imaging, thermal imaging was not affected by the structural variation of the root surfaces such as presence of cementum or cavitation.

The conventional root caries lesion activity diagnostic method via ICDAS II yielded an average sensitivity of 0.38 and an average specificity of 0.83 with a moderate in the strength of inter-examiner agreement. This study shows that the thermal imaging and PS-OCT may be suitable for root caries lesion activity assessment in a single examination and that these imaging methods are superior in accuracy and selectivity in root caries lesion activity assessment compared to the conventional visual and tactile examination.

7.2 FUTURE PERSPECTIVE

Mild developmental defects with hypomineralization are difficult to discriminate from non-cavitated caries lesions that need intervention. Severe fluorosis can be readily distinguished, but the more common mild fluorosis can be easily mistaken for active enamel caries. Developmental enamel defects have different histological structure compared to caries lesions: developmental defects have a relatively thicker surface layer of highly mineralized and transparent enamel compared to active caries lesions. Previous studies show that PS-OCT and NIR imaging can be used to successfully detect these histological differences (Hirasuna et al. 2008). However, there is a high degree of variability among developmental defects, and structural criteria for distinguishing developmental defects from caries lesions need to be established for PS-

OCT and NIR imaging. Further studies are needed to elucidate the mechanism for those differences in optical appearance.

Recently, swept-source OCT (SS-OCT) and spectral domain OCT systems have been developed as clinical tools to operate at very high scan rate without a marked loss in the signal to noise ratio. Previous studies have shown that the high quality OCT images of caries lesions can be acquired using SS-OCT systems (Shimada et al. 2010, Natsume et al. 2011). A combination of PS-OCT with SS-OCT (PS-SS-OCT) would take advantage of both systems and allow rapid acquisition of high-resolution tomographic images in a clinical setting. In addition, a cross-polarization (CP)-OCT system is being tested for clinical use and it will be crucial to develop an algorithm for detection of the transparent layer utilizing only the cross-polarization images (Nee et al. 2014).

Clinical implication of these infrared imaging techniques coupled with a dehydration system should be straightforward. Thermal cameras have been miniaturized to the point that they are now available as attachments for mobile phones. Although the dehydration and imaging setup used in these experiments may not be feasible in clinical practice due to its large size, each component can be miniaturized and integrated into a single handpiece to fit into a person's mouth. The duration of the measurement can also be significantly reduced by increasing the pressure of the air and positioning air nozzles closer to the sample. Further research is required to evaluate the clinical feasibility of the new techniques for assessment of caries lesion activity.

7.3 REFERENCES

- Amaechi, B. T., Higham, S. M., Podoleanu, A. g., Rodgers, J. A. and Jackson, D. A. (2001). Use of Optical Coherence Tomography for Assessment of Dental caries. *J. Oral Rehab.*, **28**(12): 1092-1093.
- Ekstrand, K. R., Martignon, S., Ricketts, D. J. and Qvist, V. (2007). Detection and activity assessment of primary coronal caries lesions: a methodologic study. *Oper. Dent.*, **32**(3): 225-235.
- Fried, D., Xie, J., Shafi, S., Featherstone, J. D. B., Breunig, T. M. and Le, C. Q. (2002). Early detection of dental caries and lesion progression with polarization sensitive optical coherence tomography. *J. Biomed. Opt.*, **7**(4): 618-627.
- Hirasuna, K., Fried, D. and Darling, C. L. (2008). Near-IR imaging of developmental defects in dental enamel. *J. Biomed. Opt.*, **13**(4): 044011.
- Jones, R. S., Darling, C. L., Featherstone, J. D. B. and Fried, D. (2006). Remineralization of in vitro dental caries assessed with polarization sensitive optical coherence tomography. *J. Biomed Opt.*, **11**(1): 014016.
- Natsume, Y., Nakashima, S., Sadr, A., Shimada, Y., Tagami, J. and Sumi, Y. (2011). Estimation of lesion progress in artificial root caries by swept source optical coherence tomography in comparison to transverse microradiography. *J. Biomed. Opt.*, **16**(7): 071408.
- Nee, A., Chan, K., Kang, H., Staninec, M., Darling, C. L. and Fried, D. (2014). Longitudinal monitoring of demineralization peripheral to orthodontic brackets using cross polarization optical coherence tomography. *J. Dent.*, **42**(5): 547-555.
- Shimada, Y., Sadr, A., Burrow, M. F., Tagami, J., Ozawa, N. and Sumi, Y. (2010). Validation of swept-source optical coherence tomography (SS-OCT) for the diagnosis of occlusal caries. *J. Dent.*, **38**(8): 655-665.

PUBLISHING AGREEMENT

It is the policy of the University to encourage the distribution of all theses, dissertations, and manuscripts. Copies of all UCSF theses, dissertations, and manuscripts will be routed to the library via the Graduate Division. The library will make all theses, dissertations, and manuscripts accessible to the public and will preserve these to the best of their abilities, in perpetuity.

I hereby grant permission to the Graduate Division of the University of California, San Francisco to release copies of my thesis, dissertation, or manuscript to the Campus Library to provide access and preservation, in whole or in part, in perpetuity.

Author Signature _____

A handwritten signature in black ink, consisting of several overlapping loops and a long horizontal stroke extending to the right.

Date _____

5/24/16